

SCHEFFING, CANDICE CAMILLE. Properties of a Multilayer Coating for Applications in High Level Waste Packaging.* (Under the direction of Dr. Man-Sung Yim and Dr. Mohamed Bourham.)

Materials features that are being considered for the Yucca Mountain high level waste repository include corrosion, hydrogen, and radiation effects as well as structural strength. The current plan for protection of the environment from high level waste placed inside Yucca Mountain includes a defense-in-depth design with multiple engineering barriers. The outer engineered barrier is a large drip shield made of titanium grade-7. Titanium was chosen for its high corrosion resistance and structural strength. This titanium drip shield is an elaborate design that will be expensive and may be susceptible to hydrogen embrittlement or hydrogen-induced cracking. An alternative, multi-layer coating design is proposed that will provide corrosion resistance and act as a barrier to hydrogen diffusion. The coating proposed is composed of the hydrogen barrier titanium nitride (TiN), corrosion resistant zirconium oxide (ZrO₂), and wear resistant diamond-like carbide (DLC).

TiN and ZrO₂ coatings were deposited on stainless steel substrates using magnetron sputtering and laser ablation. Analysis of the corrosion resistance of TiN and the multilayer coating, TiN + ZrO₂, has been performed at Lawrence Livermore National Laboratory (LLNL) using simulated waters, representative of the Yucca Mountain environment. The hydrogen barrier properties of TiN have also been analyzed using low temperature resistance measurements and secondary ion mass spectrometry (SIMS) analysis.

Using cyclic polarization testing, TiN was found to be resistant to SCW and BSW, Yucca Mountain simulated waters, with a passive region of 760 ± 342 mV in SCW and 408 ± 67 mV in BSW. The added ZrO₂ layer increased the passive region to 822 ± 108 mV in SCW, and increased the passive region in BSW to 1002 ± 260 mV. The ZrO₂ did not significantly increase the passive region in SCW but dramatically increased the passive region in BSW, considered to be the worst-case scenario for Yucca Mountain. Further testing in SCW using multiple coatings of TiN increased the passive region to 1050 ± 31.1 mV. Long term corrosion tests were also performed on TiN coated 316L weight-loss samples. After exposure for 6 months in corrosion tanks, the maximum corrosion rate observed was $0.530 \mu\text{m y}^{-1}$. This level was observed in the 90 °C aqueous SCW environment, and the coating had been completely stripped away while immersed in the tank.

Hydrogen diffusion testing was done on TiN coated stainless steel samples by exposing coated and non-coated samples to hydrogen at an elevated temperature for 3 hours. SIMS analysis indicated that for the TiN-coated samples there was no increase in hydrogen for the exposed sample; rather the hydrogen content of the substrate was lower than the non-exposed sample. The non-coated samples tested in SIMS did not show a difference in hydrogen content between the hydrogen exposed and non-exposed samples. More tests need to be done to confirm claims that TiN is a good diffusion barrier to hydrogen.

The multilayer TiN + ZrO₂ coating provides good resistance against corrosion as shown by the large cyclic polarization passive regions. It does not, however, provide comparable corrosion resistance to titanium, indicating it is not as protective as titanium. The hydrogen barrier property of TiN is an additional property that pure titanium does not have and may be useful for Yucca Mountain. Additional corrosion tests can be done on the ZrO₂ coatings to find a more accurate corrosion passive region for the various simulated Yucca Mountain water. The feasibility of this multi-layer coating will also be an important next step to determine in what ways the coating can be a better choice than titanium as an alternative to the drip shield design at Yucca Mountain.

*This research was performed under appointment of the Office of Civilian Radioactive Waste Management Fellowship Program administered by Oak Ridge Institute for Science and Education under a contract between the U.S. Department of Energy and the Oak Ridge Associated Universities.

**PROPERTIES OF A MULTILAYER COATING FOR APPLICATIONS IN HIGH
LEVEL WASTE PACKAGING**

by
CANDICE CAMILLE SCHEFFING

A thesis submitted to the Graduate Faculty of
North Carolina State University
in partial fulfillment of the
requirements for the Degree of
Master of Science

NUCLEAR ENGINEERING

Raleigh

2005

APPROVED BY:

Co-chair of Advisory Committee

Co-chair of Advisory Committee

Dedication

To my parents, Charles and Regina Scheffing, for all their love and support.

I would not be the person I am without you.

Biography

Candice Camille Scheffing grew up in Farmington, New Mexico and became interested in science and engineering at a young age through science fair projects. Her first introduction to Nuclear Engineering was during a science fair project testing for radon in natural gas. She graduated from Farmington High School in 1999 and continued on to college at New Mexico Institute of Mining and Technology in Socorro, New Mexico. She chose to pursue Chemical Engineering and graduated Summa Cum Laude in 2003, earning the Cramer Award for being the top female engineer of her graduating class.

Candice was fortunate to work with an amazing group at Los Alamos National Laboratory for three summers while she was an undergraduate, learning the basics of gamma spectroscopy and becoming familiar with nuclear waste management. She spent the summer after graduation at Oak Ridge National Laboratory doing gamma spectrometry work at the ^{233}U storage facility. The work she did at ORNL, “Parametric Studies for ^{233}U Gamma Spectrometry,” was recently published in the Journal for Undergraduate Research, v.4 (2004). She went to North Carolina State University in the fall of 2003 and joined the Nuclear Engineering department to begin work on her Masters degree under appointment by the Office of Civilian Radioactive Waste Management to study aspects of high level and spent nuclear fuel waste management. She received a Master of Science degree in Nuclear Engineering in May of 2005 from NCSU.

Candice had a one-act play, The Prayer, written during high school published in 2001 by Bakers Plays and enjoys live theater and music. She is an avid golfer and swing dancer in her spare time and enjoys traveling to new places. She married Clifford Combs, 2nd Lt. USAF, in March of 2005 and looks forward to finding more opportunities to use her knowledge and skills as a family member in the Air Force.

Acknowledgements

This work would not have been possible without the support provided by the Office of Civilian Radioactive Waste Management. I truly appreciate the opportunities they have given me throughout this research appointment. Colleen Babcock and Norma Ward have been very helpful in making sure that everything concerning the fellowship has run smoothly.

My practicum at Lawrence Livermore National Laboratory went beyond my expectations in allowing me to work with many very generous and brilliant people. Special thanks to Dan Day for all his time and patience in explaining potentiostats, corrosion, and geology to me. Also the additional work you did for me after I returned to school has been invaluable. Thanks also to Joseph Farmer, Jeff Haslam, and Lesa Christman for taking me as a student for the summer, despite all the other projects you had going on. I learned so much from all of you and recognize the extra time that you spent to make sure my summer work was a success. Thanks also to Dave Fix for help with the weight-loss samples after their six-months of tank exposure. Other people from LLNL that helped me throughout the summer include Lana Wong, Mike Whalen, John Estill, Ken Evans, Raul Rebak, Tiangan Lian, and Dan McCright. Special thanks to Nancy Yang of Sandia National Laboratories who performed some valuable SEM analysis on my samples.

At NCSU, I would like to thank my advisory committee for meeting with me often and providing support and advice throughout the research process. Thanks to Jag Kasichianula for the use of his lab, equipment, and valuable time to coat many samples for corrosion tests, and even more coatings for hydrogen tests. Thanks to Dr. Bourham for his time and effort in working through EIS theory with me and keeping things simple. Thanks to Dr. Yim for his open door policy and good advice in moving forward in keeping this project active. Thanks also to Dr. Gross for his time in being a part of the committee. Additional people that I cannot forget include April Jackson, Dan Leonard, Mia from the Materials Department, Fred Stevie, and Larry DuFour.

Without the help and guidance of all these people and countless others who I have not mentioned, I could not have completed this project.

Table of Contents

LIST OF TABLES	vii
LIST OF FIGURES	viii
CHAPTER 1 INTRODUCTION	1
1.1 Background.....	1
1.1.1 Yucca Mountain.....	3
1.1.2 Engineered Barrier Design.....	6
1.1.3 Drip Shield.....	9
1.1.4 Experimental Design.....	11
1.2 Objectives.....	13
CHAPTER 2 COATING	14
2.1 Apparatus, Materials, and Methods.....	15
2.2 Coating Results.....	21
2.3 Discussion.....	25
CHAPTER 3 CORROSION TESTING	26
3.1 Apparatus, Materials, and Methods.....	35
3.1.1 Polarization Testing.....	35
3.1.2 Weight-loss Testing.....	39
3.2 Corrosion Testing Results.....	40
3.2.1 Cyclic Polarization Results.....	40
3.2.2 Polarization Resistance Results.....	52
3.2.3 Electrochemical Impedance Results.....	54
3.2.4 Weight-loss Results.....	60
3.2.5 Optical and SEM Images.....	63
3.3 Discussion.....	67
CHAPTER 4 HYDROGEN DIFFUSION TESTING	69
4.1 Apparatus, Materials, and Methods.....	70
4.2 Hydrogen Testing Results.....	73
4.3 Discussion.....	78
CHAPTER 5 DISCUSSION	80
5.1 Significance of Results.....	80
5.2 Engineering and Economic Considerations.....	81

5.3	Other Applications.....	82
CHAPTER 6	CONCLUSIONS AND FUTURE WORK.....	83
6.1	Conclusions.....	83
6.2	Future Work.....	84
CHAPTER 7	REFERENCES.....	85
APPENDIX A	MATERIAL PROPERTIES.....	88
APPENDIX B	CYCLIC POLARIZATION CURVES.....	89
APPENDIX C	SAMPLE PHOTOS.....	103

List of Tables

Table 1.1	Temperature and environment levels for polarization corrosion testing.....	12
Table 2.1	Coating conditions for mirror polished samples to produce defect-free layers.....	21
Table 3.1	Composition of simulated waters.....	28
Table 3.2	BSW-13 solution recipe (TIP-CM-28, LLNL).....	29
Table 3.3	Testing solution and temperature for each disk sample.....	38
Table 3.4	Sample ID and position in long-term corrosion SCW vessels.....	40
Table 3.5	Values for plots in Figure 3.29.....	60
Table 3.6	Weight-loss sample data and corrosion rate.....	61
Table A.1	Properties of TiN and ZrO ₂	88

List of Figures

Figure 1.1	Location and disposal schematic for Yucca Mountain HLW repository (Benton, 2001).....	4
Figure 1.2	US commercial spent fuel discharge from 1970 – 2020.....	5
Figure 1.3	Defense-in-depth, multiple barrier design concept for repository.....	6
Figure 1.4	a) Engineering barrier design for Yucca Mountain with backfill (Eckhardt, 2000) and b) without backfill (OCRWM).....	7
Figure 1.5	Waste package design (Benton, 2001).....	8
Figure 1.6	Coating layers and processes under investigation.....	10
Figure 2.1	Disk sample and weight-loss coated with TiN; sample dimensions indicated.....	16
Figure 2.2	Schematic of magnetron sputtering chamber (Kasichainula).....	16
Figure 2.3	Magnetron sputtering chamber front vacuum port showing substrate bias.....	17
Figure 2.4	Laser ablation vacuum chamber, showing laser beam hitting target at 45°, plume depositing on substrate.....	20
Figure 2.5	SEM image showing de-lamination on coating before electrochemical testing.....	22
Figure 2.6	SEM elemental analysis shows carbon particle sitting on top of substrate surface (PEA0994).....	23
Figure 2.7	400 X optical microscope view of a) smooth TiN surface coated at 400°C and b) rough TiN surface coated at 500°C.....	24
Figure 2.8	X-ray spectrum of TiN coating on silicon-400 substrate.....	24
Figure 3.1	Pseudo-ternary diagram showing the effect of calcium carbonate and calcium sulfate precipitation on water composition upon evaporation (Farmer et. al, 2003).....	27
Figure 3.2	a) Controlled potential circuitry using a potentiostat (Jones, 1992), b) Pathway of a general electrode reaction (Bard, 1980).....	30
Figure 3.3	Typical cyclic polarization curve indicating important points of interest.	31

Figure 3.4	Typical polarization resistance curves.....	32
Figure 3.5	EIS model of sample and equivalent circuit.....	33
Figure 3.6	Equivalent circuit with a) Nyquist plot & b) Bode plot (Jones, 1992).....	34
Figure 3.7	Electrochemical vessel for corrosion testing.....	36
Figure 3.8	Schematic of polarization cell from ASTM standard G5.....	37
Figure 3.9	Titanium nitriding tube furnace block diagram.....	39
Figure 3.10	Selected cyclic polarization curves for 90°C SCW tests.....	41
Figure 3.11	SCW potential comparisons for cyclic polarization corrosion tests.....	42
Figure 3.12	SCW current density comparisons for cyclic polarization corrosion tests.....	43
Figure 3.13	Cyclic polarization curves for 90°C BSW.....	44
Figure 3.14	BSW potential comparisons for cyclic polarization corrosion tests.....	44
Figure 3.15	BSW current density comparisons for cyclic polarization corrosion tests.....	45
Figure 3.16	Cyclic polarization curves for 5M CaCl ₂ at 105°C.....	46
Figure 3.17	Cyclic polarization curves for SSW at 90°C.....	46
Figure 3.18	5M CaCl ₂ , SSW potential comparisons for cyclic polarization tests.....	47
Figure 3.19	5M CaCl ₂ , SSW current density comparisons for cyclic polarization tests.....	47
Figure 3.20	Average potential comparisons for cyclic polarization corrosion tests....	48
Figure 3.21	Average current density comparisons for cyclic polarization corrosion tests.....	49
Figure 3.22	Matrix of TiN coated samples after corrosion tests showing solution and temperature level of testing.....	50
Figure 3.23	Matrix of TiN + ZrO ₂ coated samples after corrosion testing showing solution and temperature level of test with zoomed in views of sample surface.....	50
Figure 3.24	Cyclic polarization curves for plain Ti and nitrided Ti in oxalic acid.....	51
Figure 3.25	Matrix showing nitrided titanium and plain titanium after corrosion testing in oxalic acid.....	52

Figure 3.26	TiN corrosion rate from polarization resistance tests in 30°C and 60 °C solutions.....	53
Figure 3.27	Corrosion rates as calculated from polarization resistance tests in high temperature solutions.....	54
Figure 3.28	Equivalent circuit showing current flow, and broken down into solution resistance and impedance.....	55
Figure 3.29	R_L , Z imaginary from Case II, and the measured impedance, Z, plotted versus frequency (Hz).....	59
Figure 3.30	Weight-loss samples after removal from corrosion tanks at LLNL (Fix, 2005).....	62
Figure 3.31	1000X optical a) pre-corrosion and b) post corrosion.....	63
Figure 3.32	SEM elemental analysis, 2000X post corrosion – dark area indicates crater where TiN is absent and O is present.....	64
Figure 3.33	1000X optical a) pre-corrosion and b) post corrosion.....	64
Figure 3.34	SEM image a) 2000X pre-corrosion and b) 1200X post-corrosion.....	65
Figure 3.35	1000X optical a) pre-corrosion and b) post corrosion.....	65
Figure 3.36	SEM image a) 1800X pre-corrosion and b) 2000X post-corrosion.....	66
Figure 3.37	1000X optical a) pre-corrosion and b) post corrosion.....	66
Figure 3.38	SEM image a) 3000X pre-corrosion and b) 2000X post-corrosion.....	67
Figure 4.1	General resistance vs. temperature trend observed between a pure metal and a metal with impurities.....	70
Figure 4.2	Diagram showing lead location and use on 5 mm-diameter sample for resistivity measurements.....	71
Figure 4.3	Low temperature hall dewar diagram, 6.0” x 2.5” x 0.75” (MMR Technologies, 2005).....	72
Figure 4.4	Stainless steel resistance vs. temperature data for plain and hydrogen-exposed.....	74
Figure 4.5	TiN coated resistance vs. temperature data for plain and hydrogen exposed samples.....	74
Figure 4.6	Plain stainless steel and TiN coated resistance versus temperature data combined for overall comparison.....	75

Figure 4.7	Nickel and TiN SIMS depth profile for hydrogen exposed and non-exposed TiN-coated samples.....	76
Figure 4.8	Hydrogen and oxygen SIMS depth profile for hydrogen exposed and non-exposed TiN-coated samples.....	77
Figure 4.9	Hydrogen, oxygen, and nickel SIMS depth profile for hydrogen exposed and non-exposed plain stainless steel samples.....	78
Figure B.1	Cyclic polarization curve – TiN coated E316L600, 30 °C SCW.....	89
Figure B.2	Cyclic polarization curve – TiN coated E316L589, 30 °C SCW.....	89
Figure B.3	Cyclic polarization curve – plain 316L stainless steel E316L571, 30 °C SCW.....	90
Figure B.4	Cyclic polarization curve – TiN coated E316L583, 60 °C SCW.....	90
Figure B.5	Cyclic polarization curve – TiN coated E316L585, 60 °C SCW.....	91
Figure B.6	Cyclic polarization curve – TiN coated E316L593, 90 °C SCW.....	91
Figure B.7	Cyclic polarization curve – TiN coated E316L595, 90 °C SCW.....	92
Figure B.8	Cyclic polarization curve – plain 316L stainless steel E316L569, 90 °C SCW.....	92
Figure B.9	Cyclic polarization curve – TiN/ZrO ₂ coated E316L001, 90 °C SCW....	93
Figure B.10	Cyclic polarization curve – TiN/ZrO ₂ coated E316L009, 90 °C SCW....	93
Figure B.11	Cyclic polarization curve – TiN/Ti/TiN coated PEA0991, 90 °C SCW...	94
Figure B.12	Cyclic polarization curve – TiN/TiN (laser) coated PEA0992, 90 °C SCW.....	94
Figure B.13	Cyclic polarization curve – TiN/TiN/TiN coated PEA0993, 90 °C SCW.....	95
Figure B.14	Cyclic polarization curve – TiNTi/Ti coated PEA0994, 90 °C SCW.....	95
Figure B.15	Cyclic polarization curve – TiN coated E316L591, 30 °C BSW.....	96
Figure B.16	Cyclic polarization curve – TiN coated E316L599, 30 °C BSW.....	96
Figure B.17	Cyclic polarization curve – TiN coated E316L586, 90 °C BSW.....	97
Figure B.18	Cyclic polarization curve – TiN coated E316L594, 90 °C BSW.....	97
Figure B.19	Cyclic polarization curve – TiN/ZrO ₂ coated E316L002, 90 °C BSW....	98
Figure B.20	Cyclic polarization curve – TiN/ZrO ₂ coated E316L003, 90 °C BSW....	98
Figure B.21	Cyclic polarization curve – TiN coated E316L588, 90 °C SSW.....	99

Figure B.22	Cyclic polarization curve – TiN coated E316L596, 90 °C SSW.....	99
Figure B.23	Cyclic polarization curve – Plain 316L stainless steel E316L570, 90 °C SSW.....	100
Figure B.24	Cyclic polarization curve – TiN/ZrO ₂ coated E316L005, 90 °C SSW....	100
Figure B.25	Cyclic polarization curve - TiN coated E316L581, 30 °C 5M CaCl ₂	101
Figure B.26	Cyclic polarization curve - TiN coated E316L584, 105 °C 5M CaCl ₂	101
Figure B.27	Cyclic polarization curve – TiN/ZrO ₂ coated E316L004, 105 °C 5M CaCl ₂	102
Figure C.1	TiN coated E316L582 disk sample before test.....	103
Figure C.2	TiN/ZrO ₂ coated E316L009 disk sample before test.....	103
Figure C.3	TiN coated weight-loss sample before test.....	103
Figure C.4	TiN coated E316L581 after polarization test in 5 M CaCl ₂ at 30°C.....	104
Figure C.5	TiN coated E316L584 after polarization test in 5 M CaCl ₂ at 105°C.....	104
Figure C.6	TiN coated E316L588 after polarization test in SSW at 90°C.....	104
Figure C.7	TiN coated E316L591 after polarization test in BSW at 30°C.....	105
Figure C.8	TiN coated E316L599 after polarization test in BSW at 30°C.....	105
Figure C.9	TiN coated E316L586 after polarization test in BSW at 90°C.....	105
Figure C.10	TiN coated E316L594 after polarization test in BSW at 90°C.....	106
Figure C.11	TiN coated E316L589 after polarization test in SCW at 30°C.....	106
Figure C.12	TiN coated E316L600 after polarization test in SCW at 30°C.....	106
Figure C.13	TiN coated E316L583 after polarization test in SCW at 60°C.....	107
Figure C.14	TiN coated E316L585 after polarization test in SCW at 60°C.....	107
Figure C.15	TiN coated E316L593 after polarization test in SCW at 90°C.....	107
Figure C.16	TiN coated E316L595 after polarization test in SCW at 90°C.....	108
Figure C.17	TiN/ZrO ₂ coated E316L004 after polarization test in 5M CaCl ₂ at 105°C.....	108
Figure C.18	TiN/ZrO ₂ coated E316L005 after polarization test in SSW at 90°C.....	108
Figure C.19	TiN/ZrO ₂ coated E316L002 after polarization test in BSW at 90°C.....	109
Figure C.20	TiN/ZrO ₂ coated E316L003 after polarization test in BSW at 90°C.....	109
Figure C.21	TiN/ZrO ₂ coated E316L001 after polarization test in SCW at 90°C.....	109
Figure C.22	TiN/ZrO ₂ coated E316L009 after polarization test in SCW at 90°C.....	110

Figure C.23	TiN coated weight-loss samples W316L581-583 after 6-month exposure in 90°C SCW Vapor.....	110
Figure C.24	TiN coated weight-loss samples W316L590-592 after 6-month exposure in 60°C SCW Vapor.....	111
Figure C.25	TiN coated weight-loss samples W316L587-589 after 6-month exposure in 90°C SCW aqueous.....	111
Figure C.26	TiN coated weight-loss samples W316L584-586 after 6-month exposure in 60°C SCW aqueous.....	112
Figure C.27	TiN coated weight-loss samples W316L594-595 after 6-month exposure in 90°C SCW at water line.....	112
Figure C.28	TiN coated weight-loss sample W316L593 after 6-month exposure in 60°C SCW at water line.....	113

Chapter 1

INTRODUCTION

1.1 Historical Background on Spent Nuclear Fuel and High Level Waste

The United States is currently faced with a large-scale storage/disposal dilemma for the highly radioactive materials produced from civilian nuclear power operations, defense nuclear programs, and smaller-scale industrial and institutional research and health activities. These materials include spent nuclear fuel (SNF) that has been irradiated in a nuclear reactor and withdrawn because it has decreased in useful enrichment, high level waste (HLW) which comes from reprocessing of SNF from either defense or civilian origin, transuranic waste (TRU) which includes any alpha emitting isotope with an atomic number greater than 92, half-life longer than 20 years and a concentration greater than 3.7×10^6 Bq/kg (100 nCi/g waste), and low-level waste (LLW) which includes any waste other than SNF, HLW, or TRU. LLW is regulated by the Department of Transportation and the Nuclear Regulatory Commission but handled and disposed by states and regions. Commercial LLW is sent to one of three disposal facilities found in South Carolina, Washington, or Utah (Saling, 2002). Solid TRU waste is currently being disposed of at the Waste Isolation Pilot Plant in Carlsbad, New Mexico, shipped from all over the country.

SNF however, is still being stored at over 100 various nuclear reactor sites where it was used to produce energy, from which approximately 20% of the nations electricity is produced (Murray, 2003). The spent fuel is stored first in water pools specifically designed for the initial cool-down of SNF after leaving the reactor. As these pools have gradually been filled over the years, an alternative storage method has been developed by energy vendors to move the older, cooled SNF to dry storage and make room in the cooling pool for the fresh SNF. There are several different designs of dry-cask SNF storage; one example, the CASTOR V/21, is made of cast iron with cooling fins added to the outside to aid in removing decay heat. The cask is placed onto a concrete pad storage area outside the reactor's main containment walls. There are also plans for a centralized facility to be built that can store many SNF dry-storage casks for a consortium of nuclear reactors to avoid many dry-cask

storage sites at individual reactor sites (Murray, 2003). However, these spent fuel pools and dry storage areas are not meant to be the final disposal location of the nuclear reactor by-product.

Spent fuel from commercial energy producers is destined for a final deep geological disposal by the Federal Government's Department of Energy (DOE). In 1982 the Nuclear Waste Policy Act (NWPA) was passed by Congress, which was a compromise among industry, government, and environmentalists outlining the timeline for the DOE to ultimately dispose of HLW/SNF geologically (from this point forward, SNF will be combined into the term HLW unless specifically addressing aspects of SNF). Since the NWPA was passed, power generators have been charging a fee of one-tenth of a cent for each kilowatt-hour to help DOE pay for the research and development of a site for disposal. Also, as a result of the NWPA, a new office for addressing this task was set up in the DOE, the Office of Civilian Radioactive Waste Management (OCRWM). This office started out by studying various locations as possible sites for the geological HLW disposal. The site possibilities were narrowed down to three by 1987, including Deaf Smith County, Texas, Hanford, Washington, and Yucca Mountain, Nevada. At this time, Congress amended the NWPA, which declared Yucca Mountain as the only site that would be further investigated by DOE for geological disposal. Since 1987, the OCRWM has been characterizing and studying aspects of HLW disposal at Yucca Mountain including geology, hydrology, seismology, volcanology, meteorology, ecology, as well as social aspects such as law, sociology, demography, and politics.

For the past fifteen years, this characterization process has dealt with drawbacks, successes, and challenges. Not only is the state of Nevada against the repository being located in the state, but the scientific analysis has been (is currently) held up to public scrutiny and challenged from many angles. The analysis for the Yucca Mountain repository is held to the highest standards of quality assurance and review to assure that the characterization is thorough. The future of Yucca Mountain with HLW emplaced inside of it is being predicted using the scientific analysis and modeling that has been going on for the past 15 years. Due to all of the challenges from various groups opposed to Yucca Mountain, the initial timeline produced by the NWPA was not met. In fact, the expected date of SNF acceptance by DOE has been changed several times, initially planned for 1998 but now does

not anticipate waste acceptance until 2010. In the aftermath of the September 11 terrorist attacks, national security has become a major argument for opening a repository at Yucca Mountain (Zacha, 2002). It has become more important to remove the many scattered targets around the country and safely dispose of all HLW in an underground repository. It has again come up in recent news that the demand for some form of HLW sequestration needs to be addressed due to the current obstacles and delays to certifying, licensing, and opening the Yucca Mountain Repository. The National Commission on Energy Policy has suggested the opening of two independent spent fuel storage installations (ISFSI) to be built (Tompkins, 2005), thus reducing the number of dry-cask storage areas from roughly 100 to 2.

The pressure for opening the Yucca Mountain Repository is great, and there are many factors that will influence how quickly this project moves forward. The research for this thesis is based on the assumption that Yucca Mountain will be opening in the future and that the engineered barrier design can be improved upon, particularly in regards to cost with possible improvements in performance.

1.1.1 Yucca Mountain

Yucca Mountain has been studied since 1978 by the DOE to determine if it is suitable for the nation's first long-term geologic repository for SNF and HLW (OCRWM, 2004). The ultimate purpose of the characterization has been to understand the mountain's physical aspects and the processes that could affect the mountain's safety. Safety to the public and to the environment over the next 10,000 years is being estimated/predicted using the results of the thousands of studies that have been carried out at multiple universities and national laboratories. The natural ability of the repository site is of great interest to ensure isolation of the waste and to minimize the amount of radioactive material that can migrate from the facility. The design of the repository includes a series of excavated tunnels, or drifts, deep underground in the solid rock of Yucca Mountain. The layout of the drifts was made to manage the heat that would be produced by the SNF (OCRWM).

Yucca Mountain is located on federal land in southern Nevada approximately 160 km (100 mi) northwest of Las Vegas, Figure 1.1. It is within the secure boundaries of the Nevada Test Site in Nye County, NV. The mountain varies in elevation at its crest from

1,500 m to 1,930 m above sea level, an irregularly shaped volcanic upland. It is located in a region known as the Great Basin, composed of volcanic tuff formed when lava having mineral gas content welded with ash into a dense, non-porous rock approximately 11.5 to 14 million years ago. The volcanoes that formed this region have been extinct for

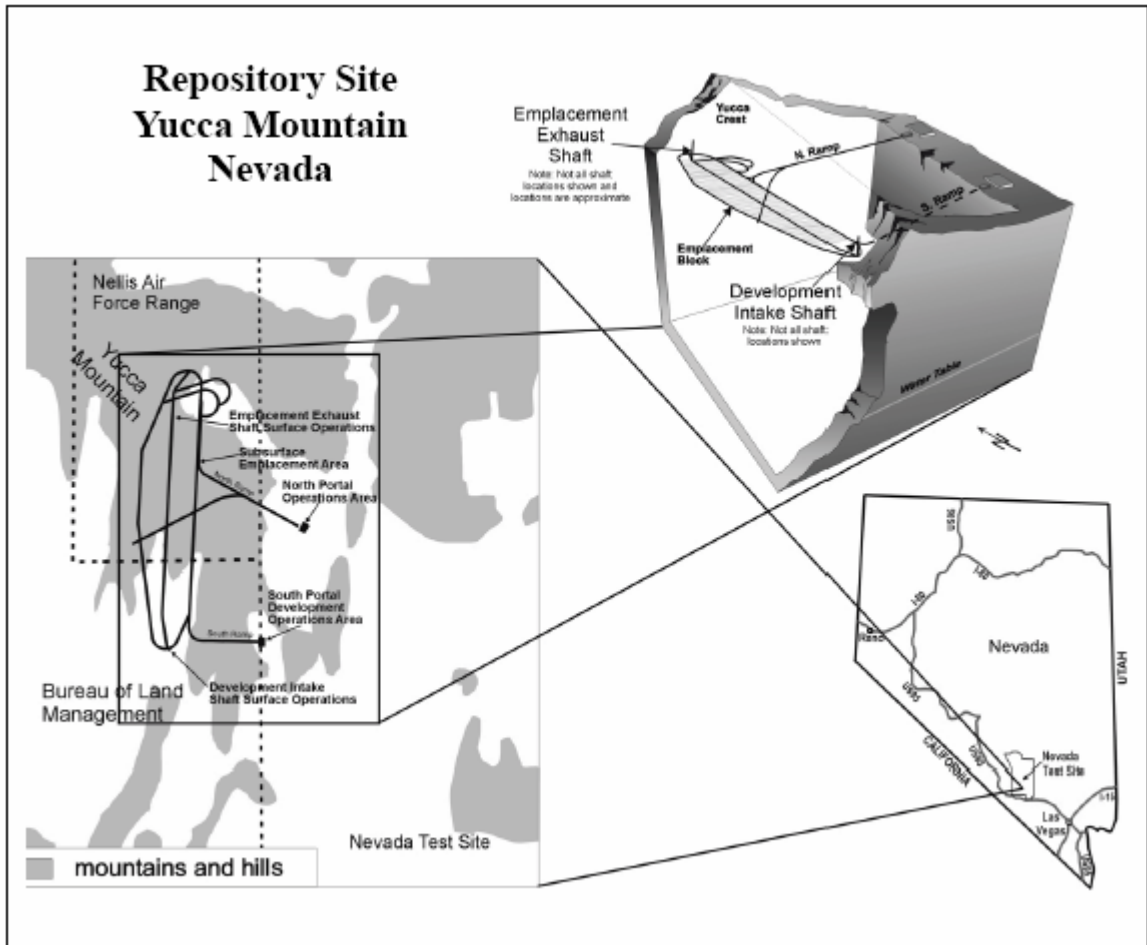


Figure 1.1 Location and disposal schematic for Yucca Mountain HLW repository (Benton, 2001).

millions of years. The site is at one of the driest places in the United States with an average rainfall of 15 cm (6 in) per year. The water table is typically 100 m to 300 m below the ground surface near Yucca Mountain, and groundwater flow in the unsaturated zone is primarily downward. The saturated groundwater flow is generally to the southeast near the Mountain, with a transition toward the south and southwest farther south. In the direction of groundwater flow, the nearest community is Lathrop Wells,

approximately 20 km (14 mi) south of Yucca Mountain (Wilson et. al., 2002). The mean annual temperature at Yucca Mountain is 63° Fahrenheit. There are no known natural resources of value such as precious metals, mineral, or oil located at the site. In addition to low rainfall and no natural resources in the area, the very location of Yucca Mountain near the Nevada Test Site makes it an ideal location because of the contamination from nuclear tests that occurred there.

As described in the NWPA, Yucca Mountain has a capacity of approximately 70,000 metric tons of uranium (MTU). This volume will account for the amount of SNF that is currently being stored at reactors across the country. With the reactor license extensions that are occurring, however, it is easy to predict that 70,000 MTU will not be sufficient for disposing of all the country's SNF. Figure 1.2 shows the cumulative U.S. commercial spent fuel discharges from 1970 thru 2020 (Murray, 2003).

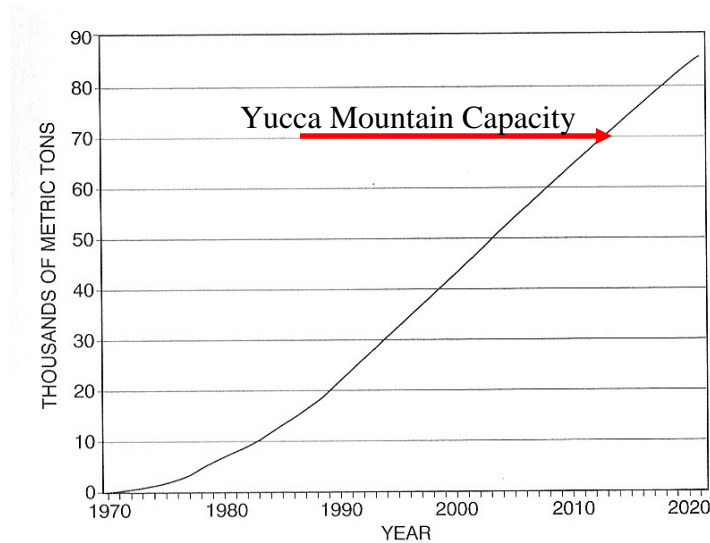


Figure 1.2 US commercial spent fuel discharge from 1970 – 2020.

With this level of SNF disposed of in Yucca Mountain, it is easy to see the importance of thorough planning and studying for the safety of the human environment. Not only will the repository easily fill up, but there will need to be further studies into disposal or other methods of dealing with the additional SNF that will be produced. Already, characterization studies have shown that the repository will not flood, the water table will not rise to the level of the emplacement drifts, the rocks making up the repository's fundamental framework will not erode, seismic effects will be minor, and the

likelihood of future volcanic disruption is minimal (Benton, 2001). Uncertainties that are present in the characterization studies due to the length of time that is being predicted (10,000 years) are high. In response to this, the design for the Yucca Mountain Repository has been made as a defense-in-depth design, which not only includes the natural barriers of the Mountain, but also includes robust engineering designs to help in achieving the repository's objectives.

1.1.2 Engineered Barrier Design

Federal regulations require that the repository for nuclear waste include at least one natural barrier and one engineered barrier to protect against water reaching the waste, degrading it, and transporting radioactive particles (NRC, 2001). The combination of the mountain's natural features and technology-based engineered components supports the defense-in-depth approach, which is illustrated in Figure 1.3.

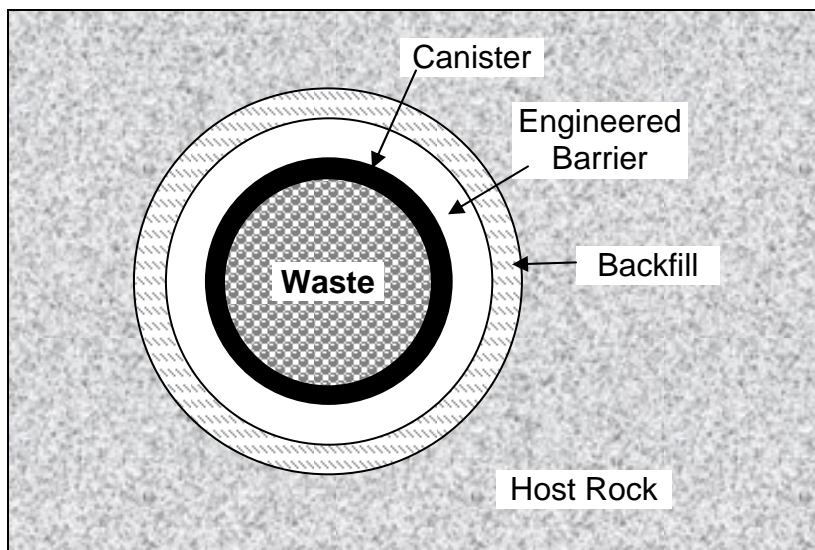


Figure 1.3 Defense-in-depth, multiple barrier design concept for repository.

The overall idea of this concept is that not only does the natural environment act as a barrier to human contact, but the waste form itself acts as a barrier. A series of obstacles between the hazard (SNF) and the human environment will add containment and reduce the uncertainty in the scientific models that have been produced. The model depicted in Figure 1.3 indicates the waste form itself as the first barrier, which can account for the

uranium oxide in zircaloy cladding, vitrified glass, or HLW mixed with cement. The second barrier is the canister or waste package in which the waste form is placed; typically, it is a large metal container that can hold multiple wastes in one bundle. The engineered barrier is an additional man-made barrier in a repository drift that adds even more protection in addition to the waste package and waste form. This diagram also indicates backfill, which is the host rock that was removed to drill the shafts and/or a highly sorbent material that can be placed into the drift around the waste package. The backfill acts as a liquid absorber and helps sorb moisture away from the waste. The host rock is the natural barrier for the design.

This concept has gone through several different design iterations over the past few years, with different designs having different types and forms of barriers that could account for the multiple-barriers. As examples, Figure 1.4a shows a design with a backfill, and Figure 1.4b shows the design without a backfill. The current design for Yucca Mountain, as seen in Figure 1.4b, does not include a backfill. This may be due to the fact that there is not expected to be a lot of seepage into the disposal drifts that would need to be diverted away from the waste package. The drip shield will likely be sufficient for seepage/drip diversion.

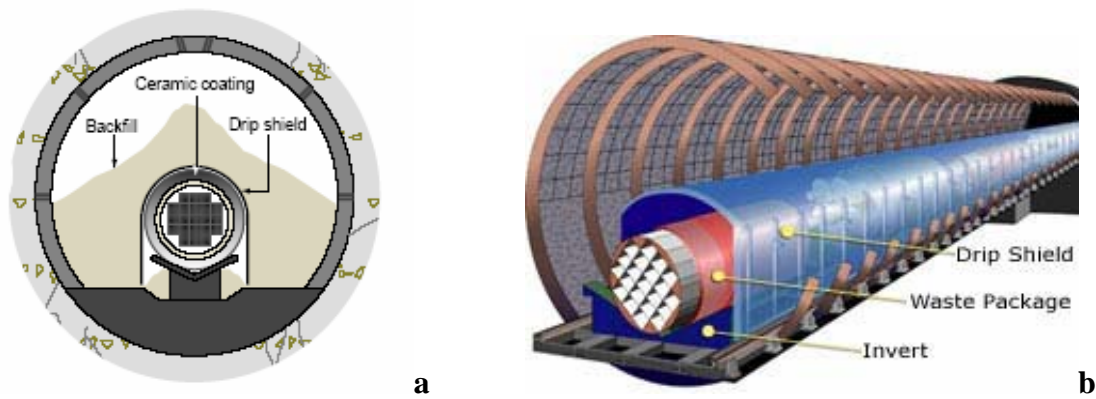


Figure 1.4 a) Engineering barrier design for Yucca Mountain with backfill (Eckhardt, 2000) and **b)** without backfill (OCRWM).

The waste forms for material that may be placed inside Yucca Mountain will range from fission products melted with glass to the uranium oxide fuel form of SNF. The waste form is resistant to corrosion as can be seen from natural analogs with glass and as

is known from the design of reactor fuel for the corrosive environments inside reactors. The waste form should hold the waste for several hundred years during which most of the radionuclides decay to safe levels (Murray, 2003).

The waste package has gone through several different designs, while the current model is that of two thick metal cylinders, one nested within the other. This design is meant to withstand many different environments especially those involving different corrosive activity. The inner shell would be made of stainless steel 316 Nuclear Grade (NG) which will improve the waste package’s performance because it is less susceptible to oxidation than carbon steel. The outer shell will be made of Alloy 22, a nickel-based alloy that has proven to be highly resistant to corrosion (Benton, 2001). Figure 1.5 is a diagram of this cylinder within a cylinder design for the waste package at Yucca Mountain.

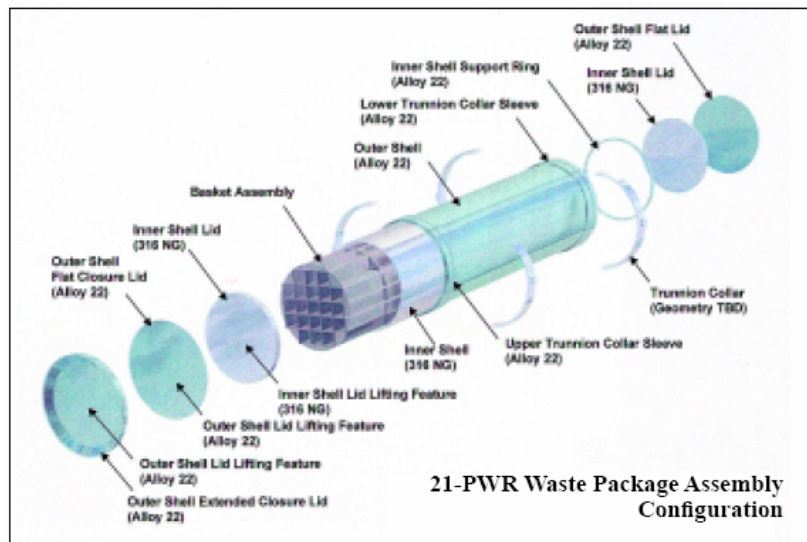


Figure 1.5 Waste package design (Benton, 2001).

The drip shield is designed to be placed over the waste package inside the tunnels just before the repository is closed. It is meant to prevent moisture, which could drip from the tunnel walls or condense on the shield, from coming in contact with the waste package. In addition to water diversion, the drip shields will protect the waste package against falling rock from the tunnel walls from direct impact. The drip shield will be made out of about 1.5 cm-thick titanium, which is extremely strong and corrosion resistant

(OCRWM). The drip shield was the motivation for this thesis work and will be discussed in more detail in the next section.

The host rock of Yucca Mountain is the largest and most effective barrier in the entire design. The geologic processes that occur in and around Yucca Mountain act to filter and delay particles from first, reaching the emplacement drifts, and further being transported into the water table. The migration of radioactive material through the geologic area of Yucca Mountain will be low because of surfaces within the rock such as particles, pores, grain boundaries, and fissures which all generally have a retarding effect on the motion of groundwater and waste material (Burkholder, 1980).

1.1.3 Drip Shield: Important Issues to Consider

The titanium drip shield mentioned in the previous section is a large shield meant to divert any liquid water seepage from the host rock, around the waste packages, and onto the drift invert. It will be emplaced in segments that link together, forming a single, continuous barrier for the entire length of each emplacement drift (OCRWM, 2000). The main design requirements for the drip shield are corrosion resistance and structural strength. The corrosion resistance is meant to ensure high performance reliability for 10,000 years. The structural strength is meant to protect the waste package from damage due to rock fall. The bulk of the drip shield will be made from titanium grade 7 at a thickness of 15 mm (0.6 in).

The current design of the drip shield will do well at providing corrosion resistance and structural support. There are, however, drawbacks to the design including: the large amount of titanium increases the costs and titanium acts as a sink to hydrogen in the environment that may cause hydrogen embrittlement. Embrittlement will reduce its structural support features. Titanium costs about 30 times more per pound than steel and is used in many applications including consumer goods, airplane fabrication, and other advanced engineering projects (Froes, 2004). The cost of the titanium drip shield was estimated in 2000 to be four billion dollars (NCNP, 2000). Hydrogen is also potentially available during repository operation as a product of the cathodic partial reaction in a general corrosion process (OCRWM, 2002). This hydrogen has the potential of being

absorbed by the titanium drip shield which could cause hydrogen embrittlement and/or hydrogen induced cracking.

As a proposal for a possible alternative to this titanium drip shield, the work for this thesis has investigated the properties of a multilayer coating design that could provide good corrosion resistance as well as prevent the absorption of hydrogen into an underlying metal. The possibilities of using a different material for a drip shield should take into account many aspects of the project including material properties (corrosion, structural strength, and hydrogen absorption/diffusion), economics, and application possibilities. For this study, the main properties considered are corrosion and hydrogen susceptibility, as could be studied in a laboratory setting. Structural integrity, application possibilities, and economics are considered briefly but not studied in depth.

The proposed alternative is a series of coatings that can be applied as multi-layers to provide a diffusion barrier to hydrogen, wear and erosion protection, corrosion and radiation resistance, and strong adhesion. The coatings were determined based on their individual properties that matched those that were important for this type of multi-layer coating. The overall design has three coated layers of titanium nitride (TiN), zirconium oxide (ZrO₂), and diamond-like carbide (DLC) under a final protective paint coating. The coating layers and process for coating application can be seen in Figure 1.6.

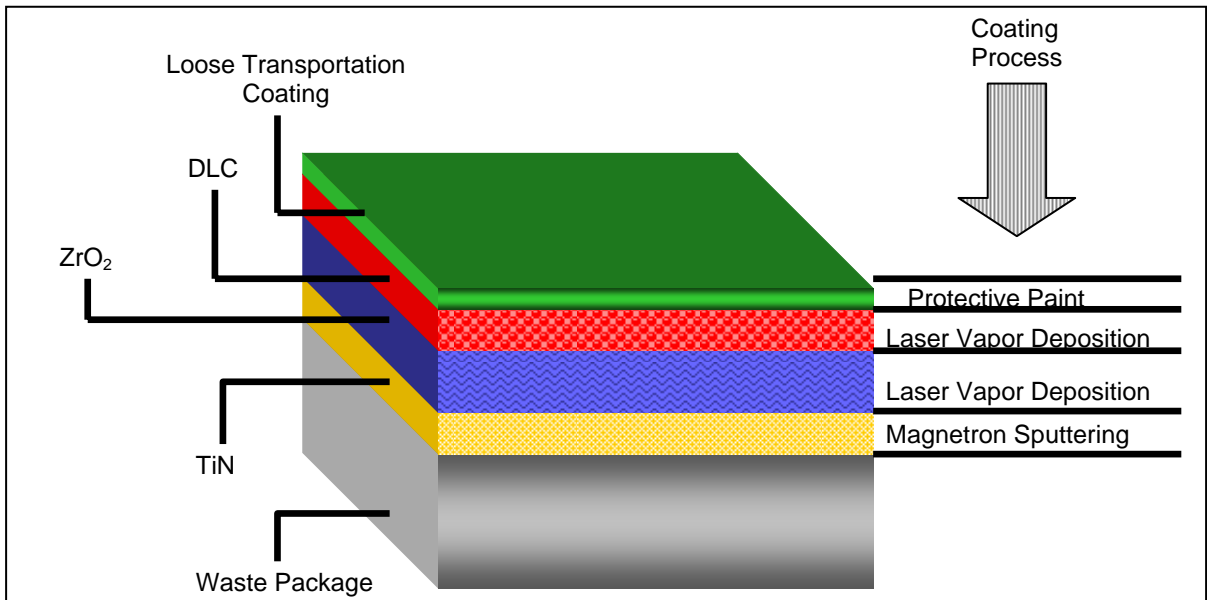


Figure 1.6 Coating layers and processes under investigation.

TiN has been shown to lower hydrogen permeability by at least four orders of magnitude (Checcheto et. al., 1996). This layer also has good adhesion properties and stability on titanium alloy substrates. TiN can be deposited using magnetron sputtering, utilizing a titanium target and nitrogen gas to produce plasma, combining atoms of Ti and N to form a near stoichiometric thin film of TiN.

The second coated layer of ZrO₂ is proposed for its protective properties against corrosion and its high wear resistance. Zirconium is insoluble in water and is resistant to high levels of radiation as observed in its uses in nuclear reactors as a fuel cladding material. ZrO₂ is also known to have good thermal barrier properties. The third coated layer, DLC, is proposed for its uses as hard, wear resistant tools, and for its lubricating properties (Voevodin et. al., 1995). This top layer is thought to add strength properties to the coating, but its adhesion properties may be problematic. The coating method proposed for both the ZrO₂ and DLC coatings is laser ablation. The coating processes are described in more detail in Chapter 2 where the coatings are produced and results are presented.

The majority of characterization work done for this multi-layer coating was done at Lawrence Livermore National Laboratory (LLNL) using their advance corrosion facility. Corrosion testing involved polarization tests on small 316L stainless steel disk samples coated with TiN and weight-loss testing on 316L stainless steel weight-loss samples. Additional characterization was performed on samples using optical and SEM microscopy of the coatings. TiN was also tested for its ability to prevent hydrogen from diffusing through into the underlying substrate. This was tested using low temperature resistance measurements and secondary ion mass spectroscopy (SIMS) analysis.

1.1.4 Experimental Design

A brief discussion concerning the design of this experiment is important because of the need for accurate, reproducible results and the limited time and resources available to achieve this end. As mentioned earlier, corrosion testing was performed at LLNL during the summer months of 2004, and all the samples that were to be tested needed to be coated before arriving at LLNL. The polarization testing involved about a two and a half

to three day turnaround from start to finish for each test, utilizing two polarization cells for testing. Coating of samples also required about two and a half to three days because of the time needed to reach a good vacuum, raise the temperature, and decrease the temperature at a controlled rate. Samples that were corrosion tested using polarization (disk samples) required only one side to be coated while the weight-loss samples required all sides to be coated.

Taking the time and materials available for coatings, the corrosion tests were planned to allow for multiple tests at each environment/temperature level. Initially, there were a total of three temperature levels and four environments to be tested. Table 1.1 indicates the generic temperature and environment levels needed for complete testing in possible Yucca Mountain conditions.

Table 1.1 Temperature and environment levels for polarization corrosion testing. Environment and temperature levels are described in Chapter 3.

	Temperature 1	Temperature 2	Temperature 3
Environment 1	XX	XX	XX
Environment 2	XX		XX
Environment 3			XX
Environment 4	X		X

Twelve samples would be needed for one test at each level and twenty four samples for two tests at each level. A more desirable number of replicates is three at each level (36 samples total), but with a total of twenty stainless steel samples available for coating, it would not even be possible to test each level twice. It would also be difficult to perform this many polarization tests in the short 12 weeks available at LLNL. In order to prepare for these shortcomings, more stainless steel samples were cut, polished, and coated at NCSU before heading to California for corrosion testing, and the most important temperature and environment levels were determined.

The most likely environment at Yucca Mountain was determined to be the first environment (as indicated in Table 1.1), which was tested at all the temperature levels. The other environments were tested at the high and low temperature levels as determined through more information about each environment. Table 1.1 indicates the tests that

were done on TiN-coated samples with an X for each test performed at the corresponding environment and temperature level. Only six samples were coated with the multilayer of TiN + ZrO₂, which required careful testing. Samples that were coated with multiple layers were tested at the high temperature levels for each environment, in order to test at the more corrosive level (higher T = higher corrosion rate). In the end, a total of 28 samples were tested, 15 with a TiN coating, 3 plain stainless steel samples, and 6 that were coated with TiN and ZrO₂. The last 4 were coated with multiple layers of TiN and tested in the high temperature level of the most likely environment (Environment 1).

The tanks for testing the weight-loss samples had two temperatures and one environment with three positions (vapor, waterline, or submerged) available for testing. These samples also took much longer to coat with TiN using magnetron sputtering (2 per week). Only 15 weight-loss samples were completely coated, and these were divided evenly among the temperature and environment positions, depending on the space available in the tanks. The final testing condition for both the disk and weight-loss samples is described in Chapter 3.

1.2 Objectives

As indicated in sections 1.1.3 and 1.1.4, the main objective for this thesis is to produce coatings of TiN, TiN + ZrO₂, and TiN + ZrO₂ + DLC and test their corrosion properties. In addition to this, testing the hydrogen barrier properties of TiN was done. TiN is the main coating of interest and was characterized more thoroughly than the other layers. The first step to achieving these objectives involved producing the coatings using the optimum conditions for magnetron sputtering and laser ablation. Chapter Two describes the coating processes used and the results obtained. Chapter Three describes the corrosion testing processes and the results obtained using polarization and weight-loss testing at LLNL. Chapter Four describes the testing done on the TiN coating to discover its hydrogen barrier properties. The final two chapters discuss the significance of the results and briefly consider the engineering and economic advantages and disadvantages of this proposal. Other applications, final conclusions, and future work are also considered in the final two chapters.

Chapter 2

COATING

The coatings that were applied during the course of this thesis work include titanium nitride (TiN), zirconium oxide (ZrO₂), and diamond-like carbon (DLC). The two deposition methods used were magnetron sputtering and laser ablation. The majority (~85%) of the completed coatings were TiN deposited using magnetron sputtering. The discussion in this section includes, first, how magnetron sputtering and laser ablation are performed, then describes the apparatus and procedure specific to these coatings. The final section presents the results and the quality of the coatings applied.

In the magnetron sputtering process, plasma is generated using a pulsed DC voltage applied between two electrodes. Ions are accelerated by the sheath potential and impact on the target (sputtering material), where the sputtered ions are allowed to deposit onto the surface of the substrate and form the desired deposited layer. The magnetic field is used to trap electrons and allow only ions to reach the target surface. The coating layer can be altered by changing the target material or changing the gaseous ions introduced into the chamber. For example, to produce a titanium coating, argon gas with a titanium target is used. The ions produce blue plasma that sputters titanium but does not combine with the metal. To produce TiN, nitrogen gas is introduced along with argon. The resulting pink plasma nitrogen ions combine with the sputtered titanium ions to produce TiN.

The second and third layers in the coating model, zirconium oxide (ZrO₂) and diamond-like carbide (DLC), were produced using pulsed laser ablation rather than magnetron sputtering. This was done due to target availability for ZrO₂ and DLC, and better coating application for oxides and DLC. Oxides are typically insulating and are very difficult to coat using DC sputtering. Laser ablation works by removing material from a target using the incident light of the laser which vaporizes a small portion of the target by thermal energy. The vaporized portion forms a plume consisting of molecular fragments, neutral particles, free electrons and ions, and chemical reaction products (Miller, 1998). The target and substrate were kept inside a vacuum chamber and under vacuum during the

ablation to minimize any chemical reaction products and encourage crystalline film growth. The substrate was positioned so that the plume could condense onto it, forming a thin film. There are many parameters that need to be considered for efficient laser ablation including the pulse duration and energy, laser power, focal length and target distance, and the beam quality.

2.1 Apparatus, Materials, and Methods

Initial preparations included the cleaning and polishing of the substrates. Several deposition conditions were attempted with different substrate materials to find the ideal coating conditions for improvement in the corrosion resistance. Early depositions of the coatings were on carbon steel samples, 1.5" x 0.25" x 0.125" (38.1mm x 6.35mm x 3.175mm), that were polished down to a 600 grit finish on all sides. The carbon steel samples were cleaned in soapy de-ionized water, rinsed, and etched with 70% phosphoric acid. Thoroughly dried samples were stored until ready for coating. Prior to deposition of the films, the samples were cleaned with alcohol followed by acetone. It was discovered that the etching process did not allow for the coating to adhere to the sample. The substrates were polished again with 600 grit polishing paper and cleaned with water followed by alcohol and acetone. This removed the poor coating and began the procedure again while neglecting the etching process. The carbon steel samples were not the correct dimensions to perform corrosion tests at LLNL, but were a useful starting point to find optimal coating parameters (deposition temperature and current from power supply).

All of the samples coated for corrosion testing at LLNL were Stainless Steel type 316L. These samples were selected based on the sample sizes required by the corrosion testing performed at LLNL and included disk samples and weight-loss samples. The disk sample, used for cyclic polarization testing, was a 16 mm diameter disk with a thickness of approximately 3 mm. The weight loss sample, used for salt fog/immersion testing, was 26 mm x 51 mm x 3 mm thick with a small hole (~3.2 mm diameter) in the center for mounting. The disk samples were prepared by polishing with 600 grit polishing paper and 5 μ m alumina polish on one side, followed by cleaning with alcohol, then acetone. The weight loss samples were not polished due to time constraints and the acceptable machine finish on the samples. These were cleaned with alcohol followed by acetone before coating. Figure 2.1 shows both

the disk sample and the weight-loss sample with the orange-gold coloring from the TiN coating.

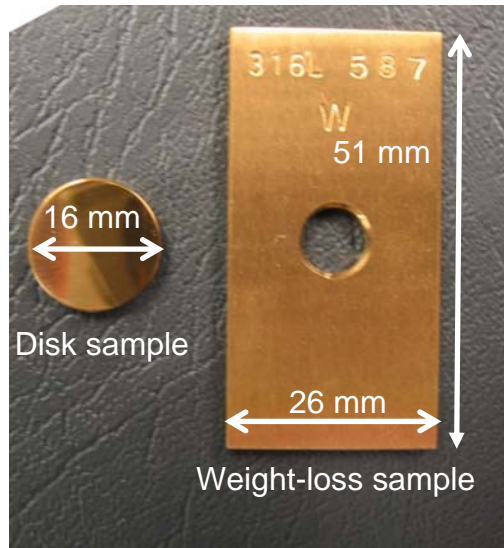


Figure 2.1 Disk and weight-loss samples coated with TiN; sample dimensions indicated.

The magnetron sputtering chamber consisted of a vacuum chamber (8 – inch diameter), vacuum gauges (Granville-Phillips series 275 conductance gauge, Granville-Phillips series 270 high-vacuum ion gauge), argon and nitrogen gas supply, 4 – inch diameter titanium target, and power supply (DORA Power System, MSS-10, 3x208V). A schematic of the magnetron sputter chamber is shown in Figure 2.2.

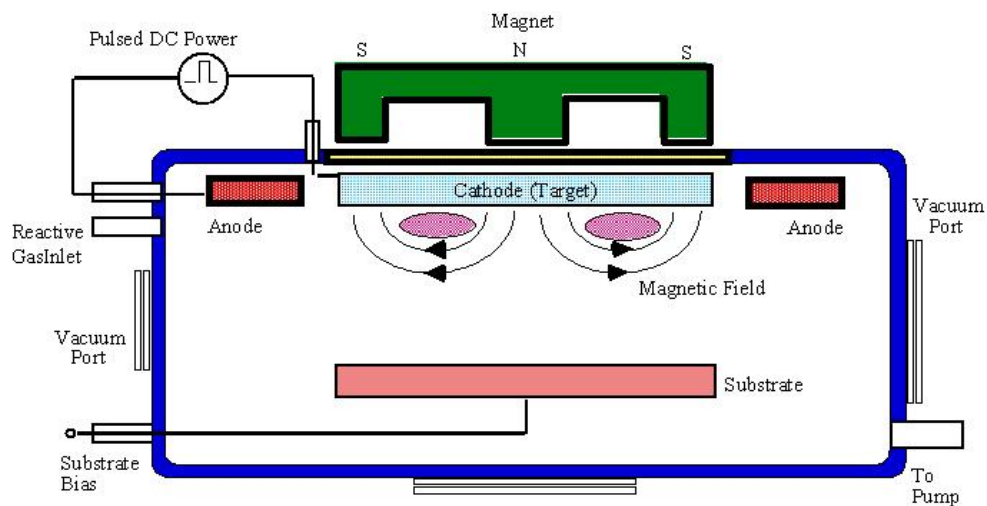


Figure 2.2 Schematic of magnetron sputtering chamber (Kasichainula)

The substrate holder is a stage for the substrate to be placed inside the chamber, made of a hollow ceramic that has coiled tungsten wire inside for heating. There is also a shutter that moves from a 'closed' position covering the substrate to an 'open' position without affecting the vacuum or other operating procedures. The shutter was used to avoid deposition on the substrate during cleaning of the target. The chamber was cooled by coiled copper around the target area with chilled water flowing through from an in-room water chiller (Neslab Coolflow Refrigerated Recirculator, HX-150). A photo of the chamber vacuum port can be seen in Figure 2.3.

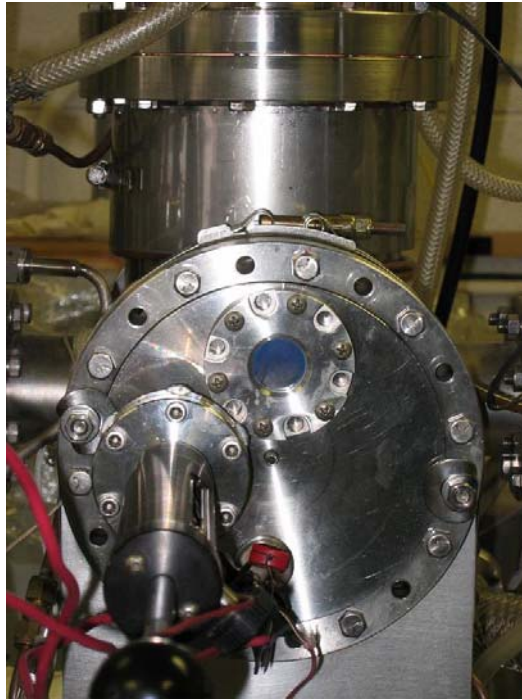


Figure 2.3 Magnetron sputtering chamber front vacuum port showing substrate bias.

The procedure for depositing titanium nitride coating on the substrate using magnetron sputtering began by placing the substrate on the stage, covering it with the shutter and closing the chamber. The chamber was baked at 120°C for 15 hours to achieve a pressure of 10^{-6} Torr. This 'baking' process helped to evaporate any residual moisture in the chamber and remove oxygen using the continued vacuum that was drawn. After the vacuum reached about 10^{-6} Torr, the stage was slowly heated up to 350 °C at a rate of about 2 °C per

minute. Once the temperature reached approximately 350 °C, the pulsed DC supply was connected to the target, including a ground connection, and the temperature was raised to 500 °C at a rate of 8 °C per minute. With the increase in temperature, the pressure in the chamber increased slightly to approximately 10^{-5} Torr. After the power supply was safely connected and the temperature was at 480 – 520 °C, argon gas (99.999% UHP) was introduced into the chamber at a pressure of 2 mTorr.

With Argon gas flowing into the chamber, the power supply was turned on for a timed ‘cleaning’ of 3 minutes while the shutter still covered the substrate from bombarding ions. The soft blue plasma, formed after turning the power supply on, was maintained with a current level set at 0.50 - 0.70 amps (A). Typically, this level of current corresponded to an effective power of 0.25 – 0.35 kW and a circulating power of 0.17 - 0.21 kW. After three minutes, cleaning was completed; with the argon gas still flowing at a pressure of 2 mTorr, the power supply was turned on again and nitrogen gas (99.999% UHP) was introduced into the chamber at a pressure of 2 mTorr. The Nitrogen gas produced soft pink plasma and the current was raised to a higher level for deposition. This pink-colored plasma indicated the formation of titanium nitride, and the current was increased to a level of about 1.48 - 1.52 A (0.73 – 0.75 kW effective power, 0.51 – 0.56 kW circulating power). The shutter was then moved so that it no longer covered the substrate, and these deposition conditions were held for 45 minutes. These conditions were known previously to produce approximately a 0.5 – 1.0 μm layer of coating, where approximately 2 – 3 Angstroms of the film per second were deposited ($1 \mu\text{m} / 10,000 \text{ \AA}$; $2700\text{s} * (2 \text{ to } 3) = 5400\text{\AA} \text{ to } 8100 \text{ \AA} = 0.54 \mu\text{m} \text{ to } 0.81 \mu\text{m}$).

At the end of the 45 minute deposition, the power supply was turned off and disconnected, temperature was reduced at a rate of about 5 – 10 °C per minute, and the argon gas pressure was discontinued. Nitrogen pressure was reduced only slightly so as to provide a positive pressure of nitrogen purge as the sample was cooled to room temperature. After the sample was completely cooled, the chamber was purged with nitrogen and the vacuum turned off to allow it to reach atmospheric pressure. The chamber was then opened and the sample removed for further characterization.

Magnetron sputtering of titanium nitride coatings was done on disk and weight – loss samples. A total of thirty disk samples of stainless steel 316L were coated with TiN on one side and fifteen weight-loss samples of stainless steel 316L were coated with TiN on both

sides. All these samples were characterized at LLNL for corrosion resistance as described in Chapter 3. Additional coatings using the magnetron sputtering method were performed on small test samples of stainless steel 304 for hydrogen analysis per description in Chapter 4. These test samples were circular disks with a 5 mm diameter and a thickness of 1 mm. These samples were polished on both sides with 600 grit paper and 5 μm alumina abrasive followed by cleaning with de-ionized (DI) water and ultrasonically cleaned in alcohol. The coatings were performed at different temperatures (between 400°C and 500°C) to determine the effect of substrate temperature on the coating smoothness and quality.

The TiN, ZrO₂, and DLC multilayer coatings were deposited using an Nd-Yag laser in the 4th harmonic (Spectra Physics Quanta Ray, GCR – 270) with 226 nm wavelength and 10 Hz pulse frequency. The pulse duration is 8-9 nano-seconds with the pulse energy of 210 mJ/pulse. The beam was focused onto the target using a focusing lens. The targets, TiN, ZrO₂ (Cerac, Ytria stabilized 1 – inch diameter), and carbon, were placed on a rotating target stage for a 45° laser incidence. The substrate was held parallel and approximately 3 centimeters from the target so that the plume is deposited directly onto the surface. The target and substrate were inside a vacuum chamber that reached 10⁻⁷ Torr prior to deposition. A schematic of the laser ablation system used is shown in Figure 2.4. The deposition chamber was baked using a resistance heater to remove water vapor and oxygen in the chamber. The substrate was finally heated to 400°C for deposition of the films. The deposition rate was approximately 1 – 2 Å per pulse. The deposition of the TiN/ZrO₂ multilayer structure was performed for 30 minutes for each layer. Multilayer deposition of TiN/ZrO₂/DLC was performed for 30 minutes, each for TiN and ZrO₂ and 15 minutes for DLC so that the coating showed good adhesion. The depositions for DLC were, first, 30 minutes, then reduced to 15 minutes for coating stability. (30min = 1800 seconds; 1800*10Hz = 18,000 pulses; ~18,000 Å = 1.8 μm).

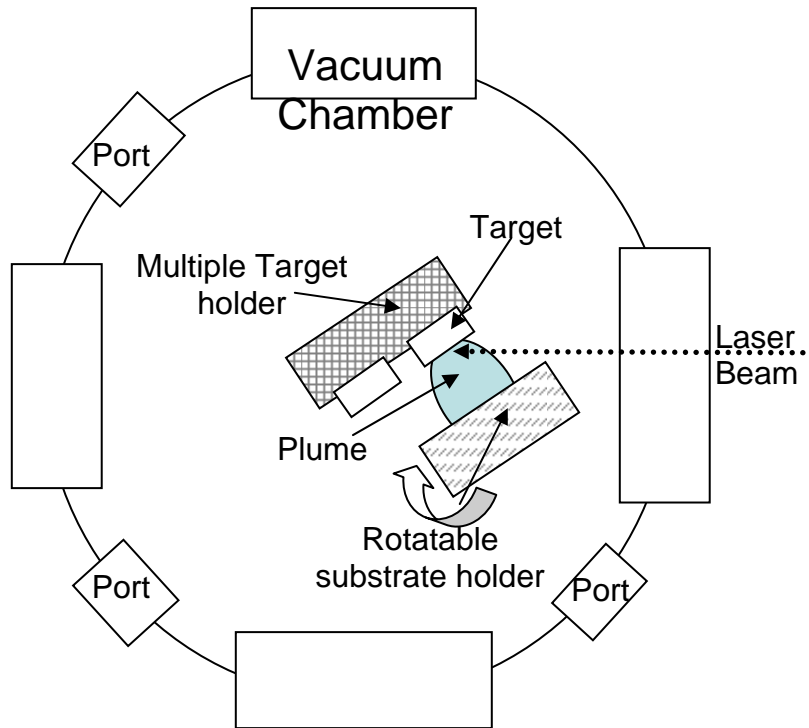


Figure 2.4 Laser ablation vacuum chamber, showing laser beam hitting target at 45°, plume depositing on substrate.

Four samples with both TiN + ZrO₂ coatings and two samples with all three layers, TiN + ZrO₂ + DLC, were made due to limited substrates and time constraints. TiN, ZrO₂ and carbon targets were placed on a rotating target stage for the laser ablation of coatings that allowed for an in-situ sequential deposition of each layer without introducing contamination to the surface between different coating layers. The samples that were coated with multiple layers were prepared entirely in the laser deposition system.

All samples tested at LLNL for corrosion resistance were coated using the magnetron sputtering or laser ablation method. After the initial corrosion testing (Chapter 3), further analysis of the coating method was needed to improve the coating surface. Additional 316L disk samples with a mirror polish were obtained through LLNL and used to test different coating conditions, including temperature, current, multiple coated layers, and coating method (laser or magnetron sputtering). The mirror polish was thought to help reduce the amount of defects and discontinuities that were likely caused by poor coating surfaces and polishing. The mirror polished samples from LLNL were coated as described in Table 2.1.

Table 2.1 – Coating conditions for mirror polished samples to produce defect-free layers.

Sample	Coating Method	Coating Layers Bottom/middle/ top	Temperature	Current
PEA 0991	Mag. Sputtering	TiN / Ti / TiN	500 °C	2 A
PEA 0992	Laser Ablation	TiN / TiN	450 °C	n/a
PEA 0993	Mag. Sputtering	TiN / TiN / TiN	500 °C	2 A
PEA 0994	Mag. Sputtering	TiN / Ti / Ti	500 / 400 °C	1.5 A

These samples were characterized using a scanning electron microscope (SEM) with elemental mapping capabilities before and after corrosion testing.

X-ray diffraction was used to determine the crystallinity of the TiN film. A TiN film on silicon (400) substrate was characterized using the x-ray diffractometer. because the film on the stainless steel contained extra peaks that shadowed the TiN lines. A Rigaku Geigerflex model number 58741 diffractometer with Cu K α (1.5404 Å) was operated at 27.5 kV and 22 mA with a slit width of 2° for x-ray work.

2.2 Coating Results

Polished samples of carbon-steel were difficult to coat without defects and delaminated areas of coating that were visible in an optical microscope at 1000X. Multiple coatings on top of each other were often needed on the carbon steel to produce a uniform coating to the scale as seen through an optical microscope. The initial coatings, completed on carbon steel for the first test of coating application requirements, led to the final procedure used for the remaining sample coatings of TiN using magnetron sputtering.

The corrosion testing required samples of specific dimensions, and therefore coatings were prepared on 316L stainless steel disk and weight-loss samples shown in Figure 2.1. Coatings on these samples were not as prone to defects and delaminated areas. The first set of samples of stainless steel that were coated produced smooth, yellow-gold colored coatings of TiN. The polished disk samples, as viewed through an optical microscope, were continuously coated and there were no obvious defects visible.

A more detailed analysis and characterization of one of these samples using an SEM microscope revealed the nature of defects that were seen with the optical microscope. These defects were delaminations of 10-20 μm observed in the SEM and shown in Figure 2.5

(produced by Nancy Yang at Sandia National Laboratories). While this figure shows the SEM image of only one sample, E316L-598, it cannot be ruled out that this phenomenon is not seen on other samples. The disk samples were coated with TiN in batches of eight using magnetron sputtering.

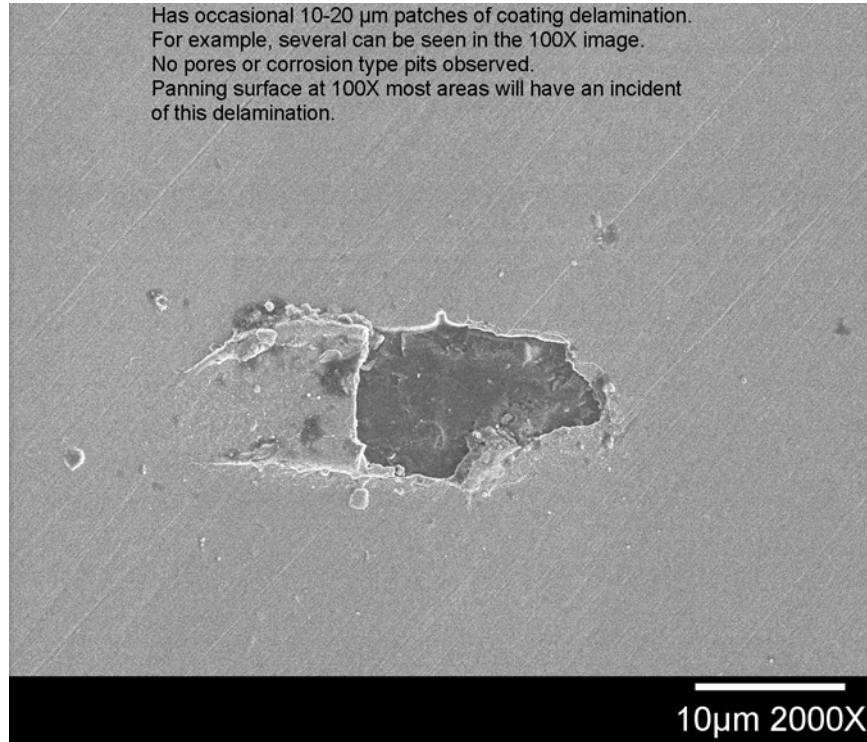


Figure 2.5 SEM image showing de-lamination on coating before electrochemical testing.

Further characterization of these defects within TiN coatings was investigated at NCSU to test how the de-lamination was occurring on the substrates. These tests were done using the mirror polished samples from LLNL. The optical microscope inspection of these samples showed particles that were sitting on top of the sample, rather than de-laminated areas. These particles, after an elemental analysis were discovered to be small pieces of carbon. Figure 2.6 shows an example of the SEM elemental analysis, performed at NCSU, on the sample PEA0994 before corrosion testing was performed. The multiple layers also showed that a layer of titanium aided in the adhesion of TiN to the substrate.

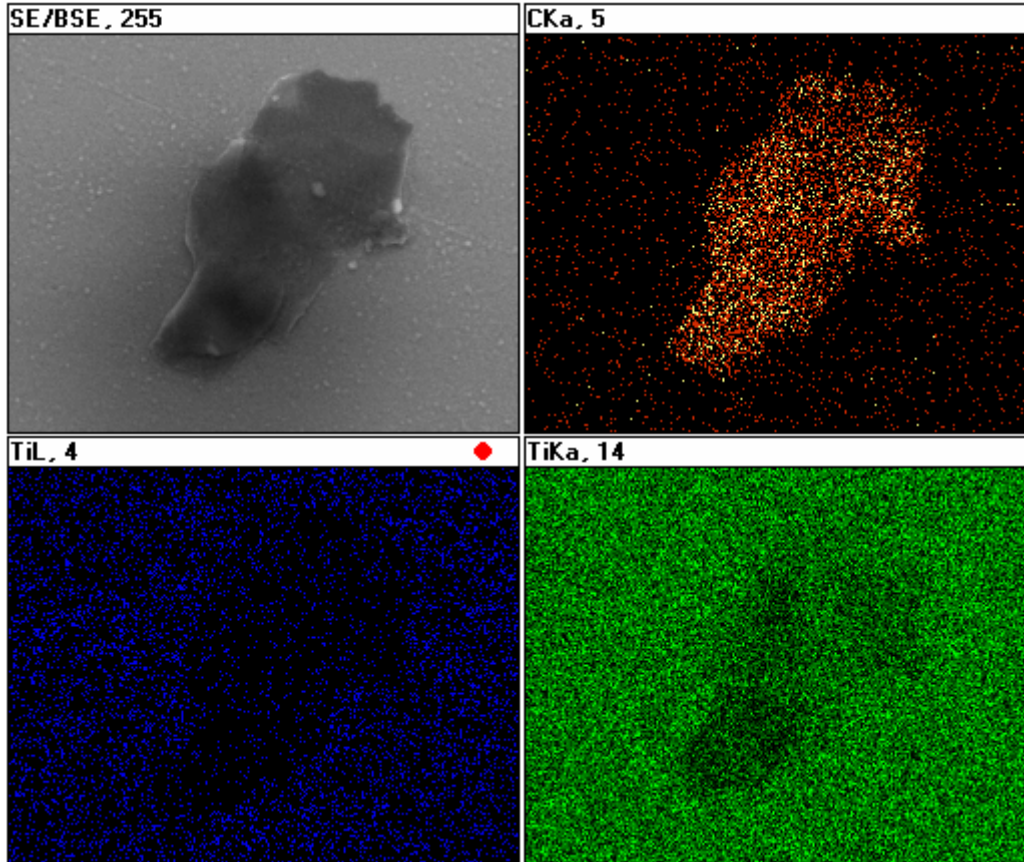


Figure 2.6 SEM elemental analysis shows carbon particle sitting on top of substrate surface (PEA0994).

There was also a difference in the samples related to the temperature that the coating was deposited. On the small punched out samples used for hydrogen diffusion testing, an obvious difference was observed between the substrate deposition temperatures of 400 °C and 500 °C. The lower temperature (400°C) deposition produced a smoother coating, despite identical sample preparations. Figure 2.7 a-b shows the difference in smoothness of samples coated at different temperatures. This figure also shows the surface smoothness that was translated from the surface preparation through to the coating. Removing the very small scratches and defects on the substrate surface would require advanced polishing techniques beyond the skills of human effort.

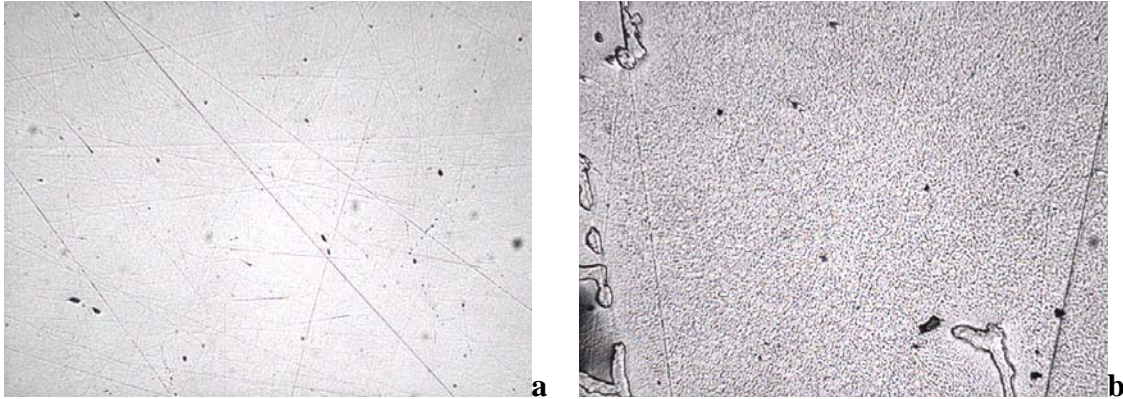


Figure 2.7 400 X optical microscope view of **a)** smooth TiN surface coated at 400°C and **b)** rough TiN surface coated at 500°C.

The x-ray diffraction peaks are shown in Figure 2.8, with the silicon (200) forbidden peak on the far left and silicon (400) peak on the far right of the spectrum. TiN gives peaks at 2-theta values of 36.67° for the (111), 42.6° for the (200), and 61.82° for the (220) reflections. All of these peaks are observed in Figure 2.8, with the (111) peak distorted by

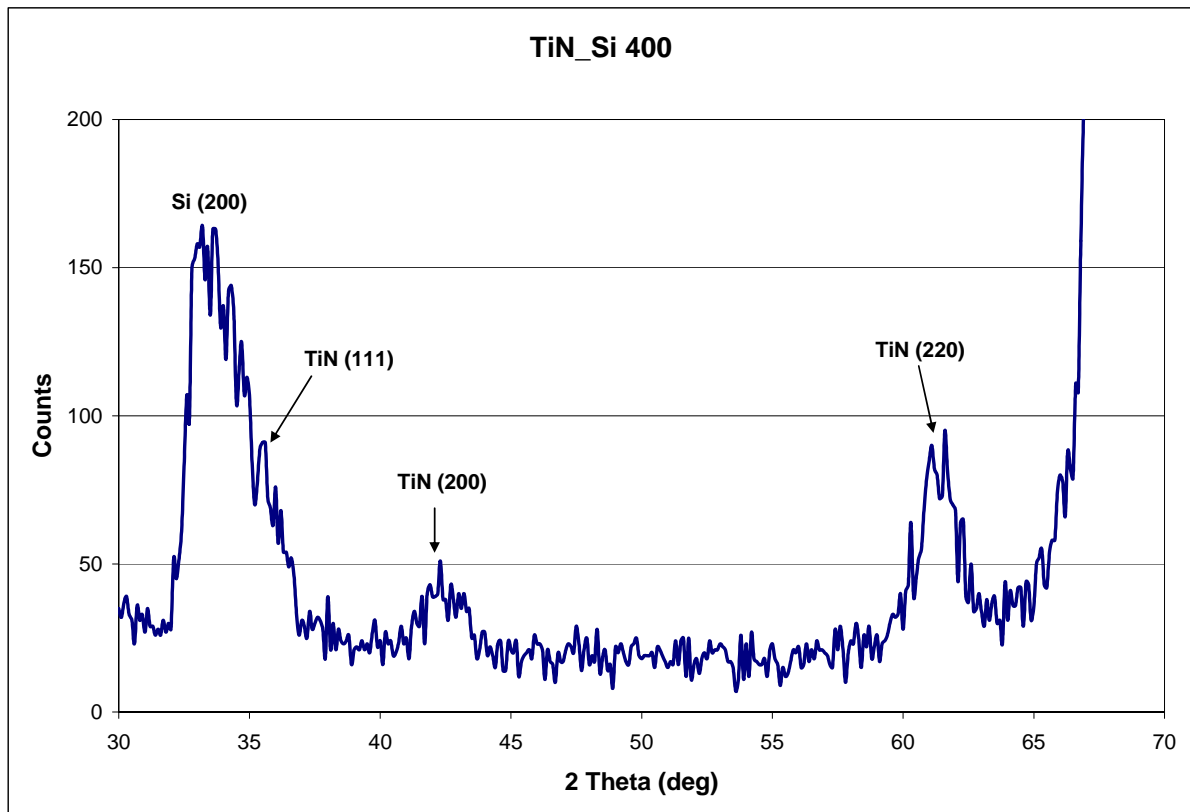


Figure 2.8 X-ray spectrum of TiN coating on silicon-400 substrate.

the large silicon (200) peak. This x-ray diffraction spectrum indicates that the coating formed using magnetron sputtering is a good layer of TiN.

2.3 Discussion

The coating process using magnetron sputtering for TiN went through several different variations in the substrate deposition temperature and the deposition current used. Based on the optical and SEM images it appears that a single coating has a susceptibility to surface defects which could cause a decrease in its protective properties. The adhesion of the coating was affected by the surface conditions and preparation prior to coating as well as by the actual substrate material. TiN did not adhere well to carbon steel, but did adhere to 316L stainless steel. An added layer of titanium coated on the substrate before coating the TiN increased the adhesion. The deposition temperature that produced a smooth coating was 400 °C along with a current source of 2 A. A higher deposition temperature produced a rougher surface, but still produced a good, continuous coated layer. The x-ray analysis performed showed that the coating produced was crystalline TiN without added impurities.

The laser deposition process produced an effective coating of ZrO₂, but it was difficult to produce a good DLC layer. The DLC did not adhere well to the ZrO₂ layer. Reducing the thickness (deposition time) of the DLC allowed for better adhesion. The laser ablation process worked well for coating all three layers in sequence without disturbing the sample surface.

Chapter 3

CORROSION TESTING

All testing for corrosion resistance was completed at Lawrence Livermore National Laboratory (LLNL) in Livermore, California during the summer months of 2004. Electrochemical corrosion testing has been done for many years, and for the specific case of corrosion at Yucca Mountain there has been considerable research into precise environments that may be present in the disposal drifts and cause corrosion (OCRWM, 2002). The facility at LLNL has been involved in the Yucca Mountain project since 1977, and has been doing the most extensive corrosion testing for the project. It is home of the Long Term Corrosion Test Facility (LTCTF) where many important materials corrosion studies have been and currently are being done to help with the characterization and design for the project.

The water environments used for this study are the same that have been used at LLNL for the LTCTF testing. Based on samples taken from wells around the Yucca Mountain site, sample water compositions have been developed that are representative of those that might be expected in repository conditions. These simulated waters can be broken up into three different categories as illustrated in Figure 3.1, sulfate, bicarbonate, or calcium chemistries (Farmer et. al., 2003). This diagram illustrates what is a relatively simple way to describe the types of brine that would evolve based on dilute water compositions at Yucca Mountain (Gdowski et. al., 2002). The evolution of different water chemistries in the same colored region on the pseudo-ternary diagram will all evolve to the same end-point. The evolution of natural waters was determined using a geo-chemical simulation model for five experimentally determined pore waters as input. Each of these water chemistries were modeled through evaporative processes to find what end-point solution chemistry would be in the repository drifts. The final simulation of evaporation to dryness, the deliquescence point, led to the choice of water chemistries that have been simulated and used for many of the corrosion tests at LLNL (Farmer et. al., 2003). Evaporative chemical experiments have also been conducted to find the major ion concentrations that remain (Rosenberg, et. al., 2001).

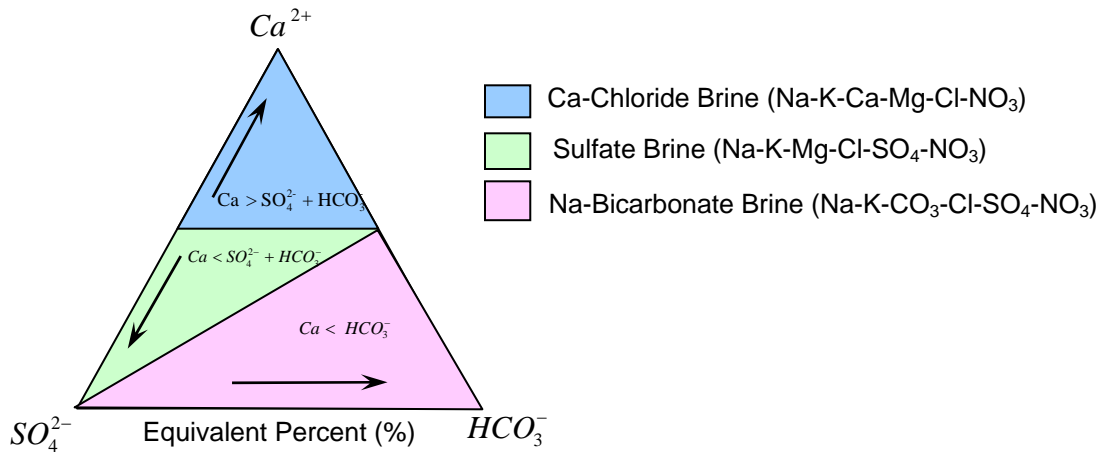


Figure 3.1 Pseudo-ternary diagram showing the effect of calcium carbonate and calcium sulfate precipitation on water composition upon evaporation (Farmer et. al, 2003).

There are several different simulated waters that have been made to represent the waters predicted by the evaporation model. These waters include:

- Simulated concentrated water (SCW) – concentrated J-13 well water, bicarbonate
- Simulated dilute water (SDW) – less concentrated J-13 well water, bicarbonate
- Basic saturated water (BSW) – saturated bicarbonate with basic pH
- Simulated acidified water (SAW) – concentrated sulfate with acidic pH
- Saturated sulfate water (SSW) – saturated sulfate
- Concentrated calcium chloride (5 M CaCl_2) – calcium solution.

All of these waters are based on analyses of J-13 well water, which is a representative water well near Yucca Mountain. It is a dilute sodium – bicarbonate – carbonate ($\text{Na-HCO}_3\text{-CO}_3$) water, and the simulated concentrated water (SCW) is 1000 times the concentration of this well water. SDW is 10 times more concentrated than J-13 well water, while SAW is 1000 time more concentrated, and acidified using sulfuric acid (H_2SO_4). SSW is based upon a separate assumption that the evaporation of J-13 well water becomes a sodium – potassium – chloride – nitrate solution with the absence of sulfate and carbonate. This water is a concentrated solution that begins to solidify at temperatures below 90°C . BSW is a test environment that has a pH between 11 and 13 and a boiling point near 110°C . The solution for BSW has three separate recipes depending on the desired pH level. The CaCl_2 solution is precisely that, a concentrated calcium chloride at 5 M. The CaCl_2 solution has been

considered the harshest environment for Yucca Mountain, but at the same time is unlikely. Recent analysis by the NWTRB has concluded that this environment is in fact unlikely to occur and cause significant corrosion to the Alloy 22 waste package (NWTRB, 2004). Of the remaining solutions from those listed, a bicarbonate solution is the most likely with BSW being the most aggressive environment in that set. The compositions for SCW, SDW, SAW, and SSW can be seen in Table 3.1, while the recipe for BSW-13 is given in Table 3.2.

Table 3.1 Composition of simulated waters.

Ion	Concentration (mg/L)			
	SCW	SDW	SAW	SSW
K ⁺	3400	34	3400	141,600
Na ⁺	40,900	409	37,690	487,000
Mg ⁺²	<1	1	1000	0
Ca ⁺²	<1	0.5	1000	0
F ⁻¹	1400	14	0	0
Cl ⁻¹	6700	67	24,250	128,400
NO ₃ ⁻¹	6400	64	23,000	1,310,000
SO ₄ ⁻²	16,700	167	38,600	0
HCO ₃ ⁻¹	70,000	947	0	0
pH	9.8 – 10.2	9.8 – 10.2	2.7	7.0

Table 3.2 BSW-13 solution recipe (TIP-CM-28, LLNL)

Chemical	Chemical Quantity
KCl	8.7 g
NaCl	7.9 g
NaF	0.2 g
NaNO ₃	13.0 g
Na ₂ SO ₄	1.4 g
H ₂ O (deionized)	66 ml
10N NaOH	2 ml
pH	13.13

Corrosion testing of materials is typically carried out using electrochemical methods such as polarization. Polarization techniques have been used for years to characterize the corrosion behavior of metal alloys in specific environments (Dean, 1986). The general approach is to immerse a substrate into an environment that does not have oxidizing agents present, and measure the corrosion current as a function of the oxidation potential as the sample is polarized. Polarization methods followed for this thesis included ASTM standards G 5 – 94 (2004) and G 61 – 86 (2003) with slight modifications due to the need for specific water solutions and slight differences in vessel configuration. Polarization of a cell is the potential change from the equilibrium of a half-cell electrode potential caused by a net surface reaction rate for the half-cell reaction (Jones, 1992). A schematic of a polarization cell with a potentiostat and a generic electrode reaction can be seen in Figure 3.2 a-b. Polarization is a common method used for accelerated testing of the corrosive behavior for a material.

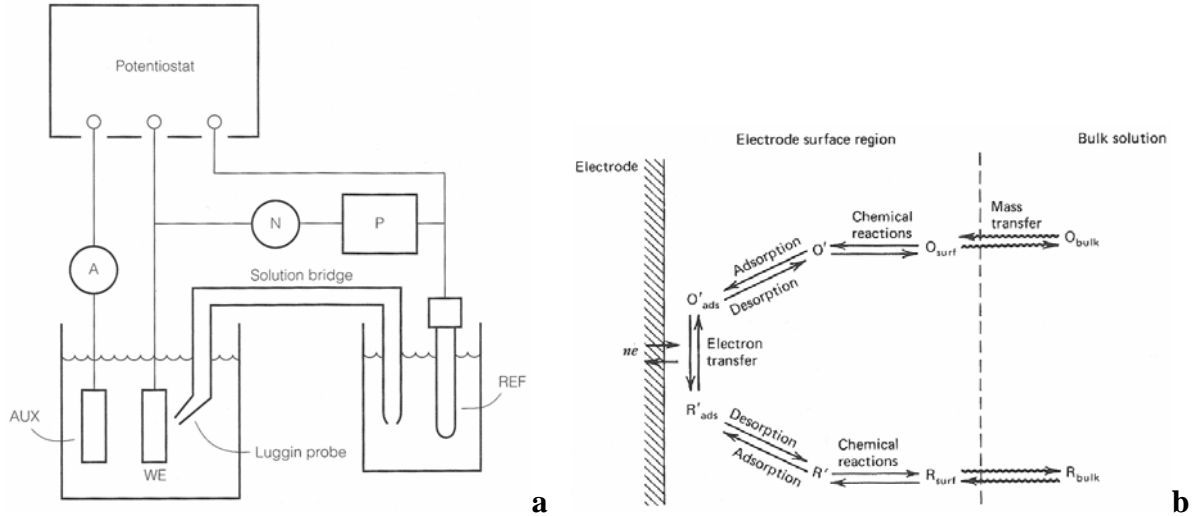


Figure 3.2 a) Controlled potential circuitry using a potentiostat (Jones, 1992), **b)** Pathway of a general electrode reaction (Bard, 1980).

The polarization method described in ASTM G-61 is potential controlled (potentiostatic), and uses a potentiostat which automatically adjusts the applied polarizing current to control potential between the working electrode (WE) and the reference electrode (REF). The WE is the substrate of interest that is being corrosion tested while the REF is joined to the cell through a solution salt bridge or luggin probe. An auxiliary electrode is used by the power supply to apply a potential to the working electrode, while the current is measured with respect to the REF electrode. The current approaches a steady-state value at each controlled potential step and allows for a detailed study of the important parameters affecting the formation and growth of passive films (Jones, 1992).

These parameters can be interpreted from polarization curves to determine the general properties of a sample. A polarization curve is performed only after the corrosion potential, E_{corr} , or equilibrium potential between the WE and REF, has been reached (typically 1 to 24 hours immersed in the solution). E_{corr} is also referred to as the open circuit potential. A cyclic polarization curve begins a potential scan of the substrate at 50 mV below E_{corr} (for these experiments) and increases the potential, V_f (V vs. REF), at a scan rate of 0.6 V/h (+/- 5%) (ASTM, 2003). The potential scan is increased until the scan reaches a limit of 1.2 V or 5 mA, at which point the potential scan is reversed at the same rate. Figure 3.3 shows a typical cyclic polarization curve, which indicates localized corrosion susceptibility and shows the region of passivity.

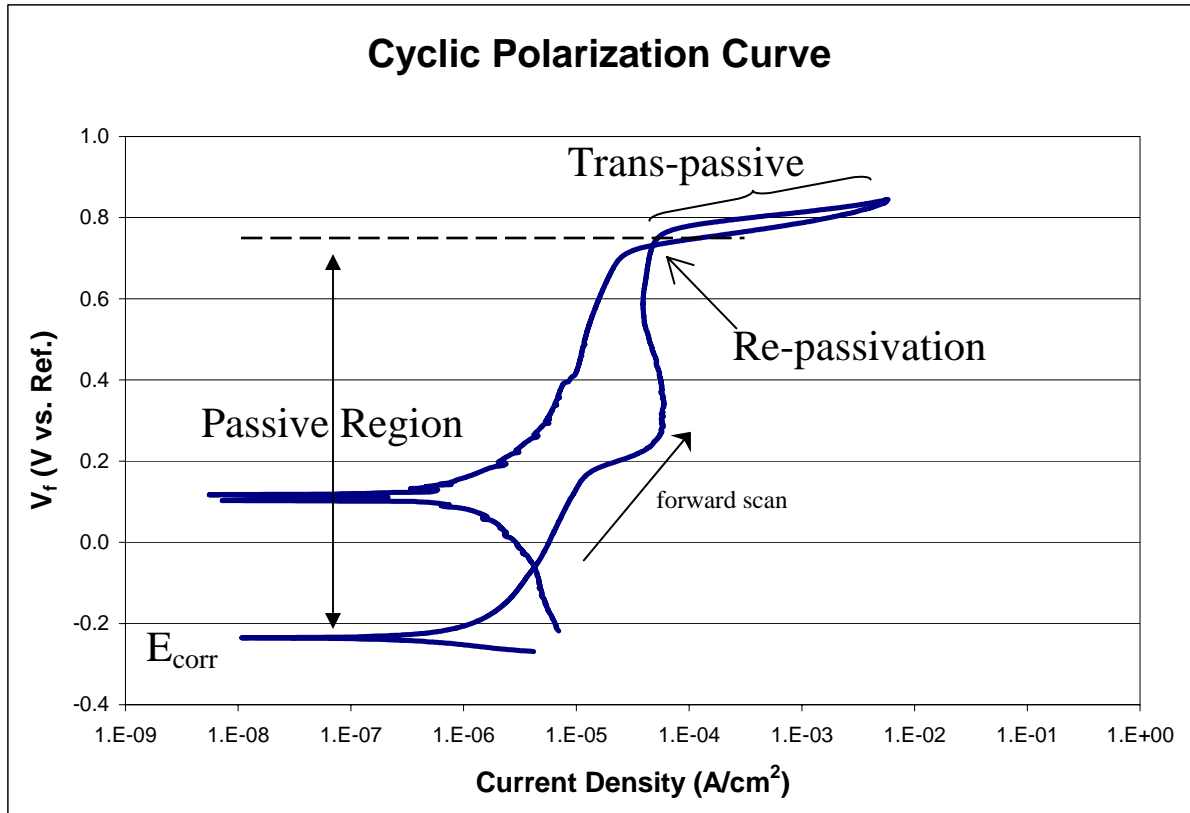


Figure 3.3 Typical cyclic polarization curve indicating important points of interest.

The passive region is where a film has built up on the surface of the sample, preventing localized corrosion from actively propagating, indicated by a small change in current with large changes in potential. The onset of localized corrosion is usually marked by a rapid increase of the current with a small increase in potential, or a trans-passive region. The reverse scan will typically decrease the current density, and the curve will cross itself and re-passivate. The passive region extends from the open circuit potential, E_{corr} , to the potential where re-passivation occurs. A large passive region and low current density for re-passivation indicates a more corrosion resistant material. Due to the large range of potential that is scanned during this test, causing the sample to go through a passive region and passivate, the cyclic polarization test is destructive to the sample. Corrosion actively occurs on the surface of the sample and its effects can be seen after being removed from the solution.

Another potentiostatic test that can be performed using a potentiostat is a polarization resistance scan. This scan is done at the same rate as the cyclic polarization scan, 0.6 V/h, but is scanned from 20 mV below the open circuit to 20 mV above the open circuit. This

scan provides data that can be used to calculate a general corrosion rate for the sample. Figure 3.4 shows a set of three polarization resistance scans, performed one after the other with brief pauses to allow the potential to reach the open circuit level before re-testing.

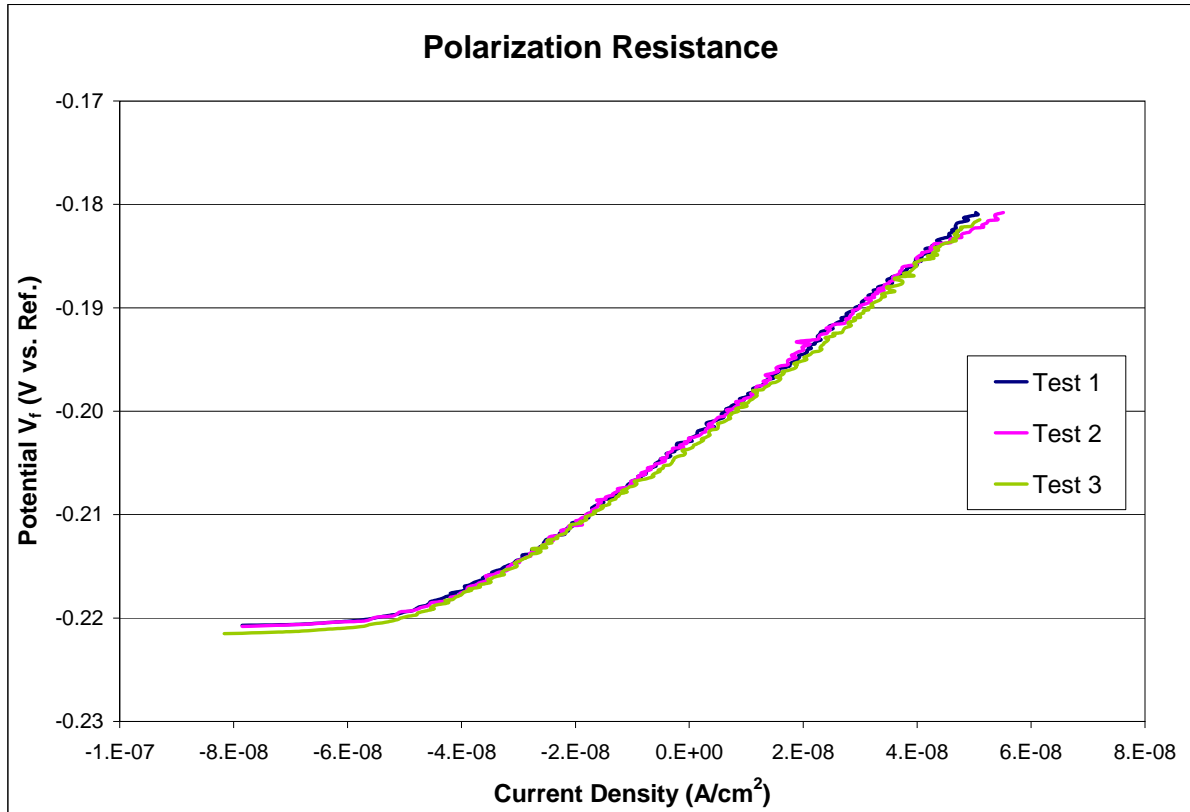


Figure 3.4 Typical polarization resistance curves.

The slope of the polarization resistance curve has been shown to be inversely proportional to the corrosion rate (Jones, 1992). The relation was quantified using the software developed by Gamry^R, EchemAnalyst. EchemAnalyst uses the slope of the polarization resistance curve along with the density of the sample, the number of equivalents exchanged, the atomic weight, sample area, and Faraday's constant to calculate a sample corrosion rate. This test is not destructive to the sample due to the small potential range that is scanned.

A final polarization method used in this thesis was electrochemical impedance spectroscopy (EIS). This method uses a small perturbation of the system at steady state, rather than a large potential sweep. The EIS method, as performed in this thesis, applies a small sinusoidal excitation at varying frequencies to the electrochemical cell, which is not a destructive test to the sample. The cell acts as an impedance to the excitation, and it can

typically be modeled using an equivalent circuit of resistors and capacitors that pass current with the same amplitude and phase angle that the real cell does under a given excitation (Bard, 1980). A basic cell and circuit model that are used in this thesis are shown in Figure 3.5. This figure shows a solution resistance, double-layer capacitance, and a corrosion

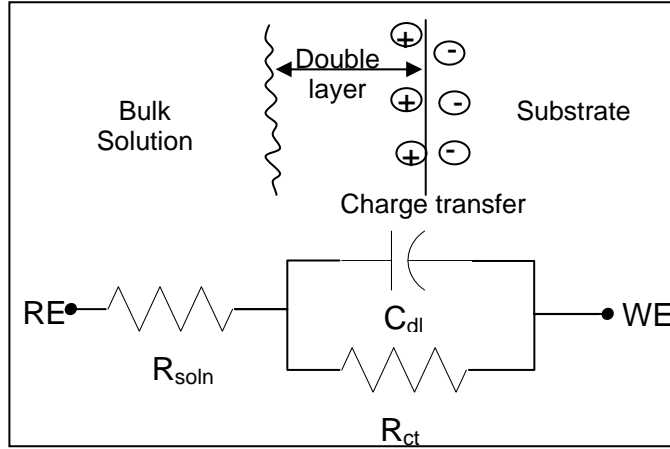


Figure 3.5 EIS model of sample and equivalent circuit.

resistance for the solution, solution-sample interface, and sample respectively. While there is the possibility to calculate several useful properties of the solution and the sample, the chief objective of an impedance experiment is to discover the frequency dependencies of the solution resistance, R_s , and the double layer capacitance, C_{dl} (Bard, 1980).

EIS equivalent circuits can be modeled using mathematical descriptions of the electrical circuit. The time-dependent current response $I(t)$ of an electrode surface to a sinusoidal alternating potential signal $V(t)$ is expressed as an angular frequency (ω) dependent impedance $Z(\omega)$:

$$Z(\omega) = \frac{V(t)}{I(t)}$$

$$V(t) = V_o \sin \omega t$$

$$I(t) = I_o \sin(\omega t + \theta)$$

where θ is the angle between $V(t)$ and $I(t)$, and ω is the angular frequency as provided by the potentiostat perturbation (Jones, 1992). The impedance can be expressed in terms of real, $Z'(\omega)$, and imaginary, $Z''(\omega)$, components:

$$Z(\omega) = Z'(\omega) + Z''(\omega)$$

(Jones, 1992). The data gathered from an EIS experiment provides a Bode plot of both the impedance and phase angle versus the frequency, and a Nyquist plot showing a semicircle of imaginary and real impedance with the frequency moving in a counterclockwise direction (Figure 3.6). This circuit is often an adequate representation of a simple corroding surface.

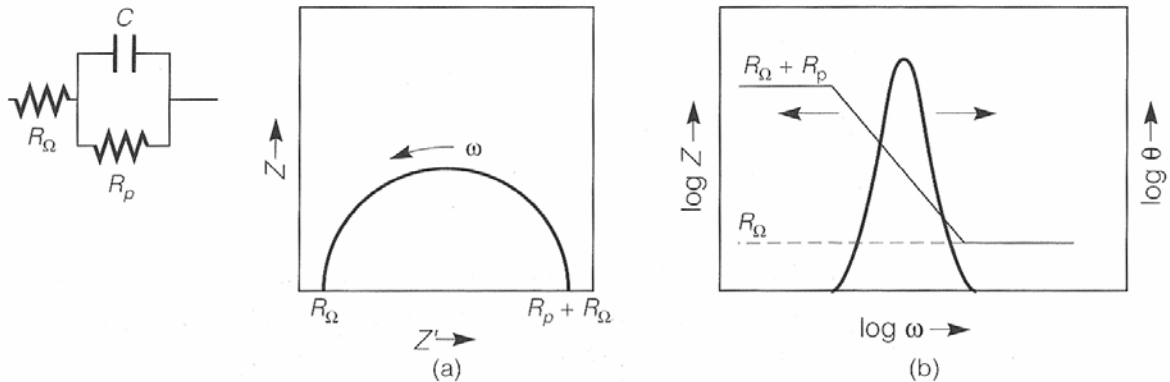


Figure 3.6 Equivalent circuit with **a)** Nyquist plot and **b)** Bode plot (Jones, 1992).

Notice the relationship between the solution resistance (R_Ω) and the corrosion resistance (R_p) which can be seen in both the Nyquist and Bode plots: at very high frequency, the imaginary component, Z'' , disappears leaving only the solution resistance. At low frequencies, the imaginary component disappears again, leaving the sum of the solution and corrosion resistance.

The Gamry^R software, EchemAnalyst, has the ability to perform analysis on EIS data, but it is best to know the equivalent circuit for the sample and solution being tested before performing the software analysis. Assumptions can sometimes be made and the model can be simplified. The analysis method used for this thesis is described in section 3.2.3. It was found that no single equivalent circuit model worked well for all samples tested. There was no consistency in any one model to allow useful reporting of the data.

General corrosion properties were also studied briefly using the weight-loss samples. General corrosion studies can be done by exposing a sample to a solution for a specified period of time, t , and after a sufficient time period calculating the corrosion rate from the weight loss, w , of the sample. The corrosion rate (dp/dt) for weight-loss samples can be calculated in centimeters per year using the following equation:

$$\frac{dp}{dt} \left(\frac{cm}{year} \right) = \frac{w}{\rho A t}$$

Where w is the weight loss in grams, ρ is the density in grams per cubic centimeter, A is the exposed area in square centimeters, and t is the time in years that the sample was exposed (Farmer et. al, 2000).

3.1 Apparatus, Materials, and Methods

Corrosion tests were performed at LLNL using the advanced corrosion testing facilities that have been used for Yucca Mountain corrosion studies for more than 10 years. The corrosion analyses at LLNL for Yucca Mountain follow strict quality assurance protocol to ensure defensible results and maintain consistency in all analysis, no matter who performs them or where they are performed. The corrosion studies performed on the samples for this experiment followed the same procedures as those used at LLNL.

Two different samples were tested for corrosion using two different methods: potentiostatic measurements on disk samples as described in the introduction and coating section of this thesis, and general corrosion of weight-loss samples in concentrated solutions.

3.1.1 Polarization Testing

Potentiostatic corrosion tests were done using a Gamry Instruments Version 4.30 Potentiostat (PC14/300 model) with DC105 and EIS 300 capabilities. This potentiostat can control the electrode potential within 1 mV of the preset value and has an anodic current range from 7.5 nA – 750 mA. The input impedance is $>10^{12}$ ohms with an accuracy of $\pm 0.3\%$ of the voltage range or $\pm 0.3\%$ full-scale for the current. A three-electrode configuration with a platinum auxiliary electrode, silver/silver-chloride reference electrode (Accumet), and a test specimen/working electrode was the design used for testing. A solution volume of 950 ml with a nitrogen bubbler was used along with a condenser as the gas outlet. The solution was kept at temperature using a circulating oil bath with automatic controls for temperature stability and uniformity (PolyScience model 9112).

The test cell was a 1-L round flask made of borosilicate glass with five openings for the test electrode, platinum electrode, Luggin capillary with salt-bridge connection for the

reference electrode, and the gas bubbler and condenser. A thermometer is often seen in designs such as this, but with the silicon bath, the solution temperature was checked just before and after testing and assumed to stay constant during the testing period. The Luggin probe-salt bridge maintained separation between the bulk solution and the reference electrode and also allowed for adjustment of the tip to be in close proximity of the test electrode. The glassware and material used for mounting and testing the sample can be seen in Figure 3.7 which closely matches the design as described in ASTM standard G5-94 on the *Standard Reference Test Method for Making Potentiostatic and Potentiodynamic Anodic Polarization Measurements* (Figure 3 in standard), Figure 3.8.

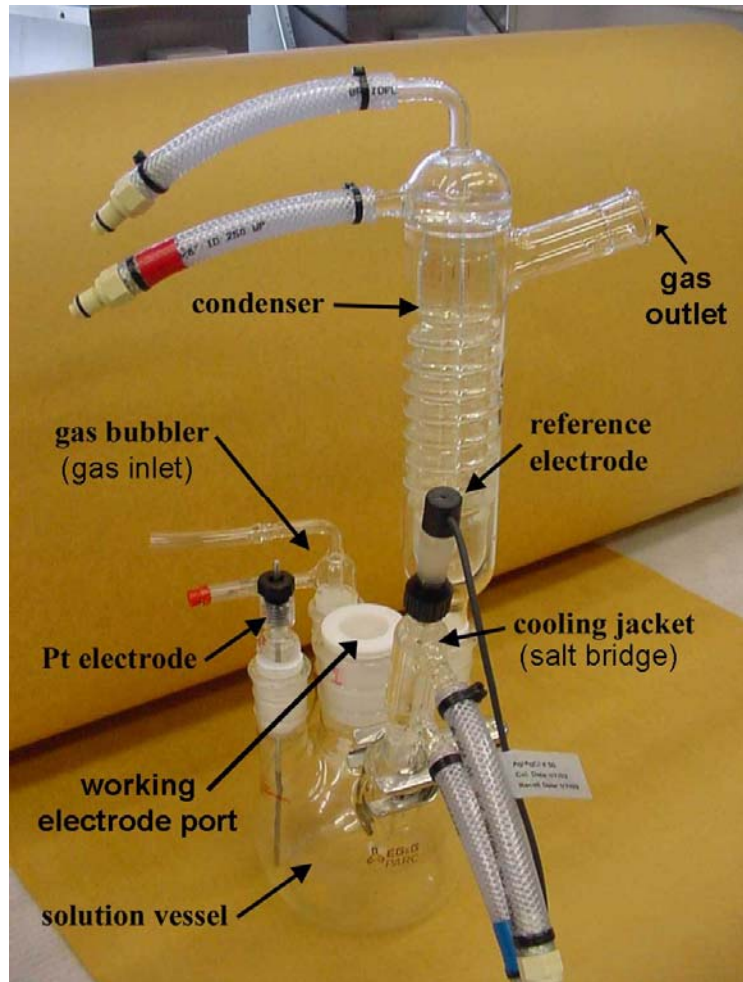


Figure 3.7 Electrochemical vessel for corrosion testing.

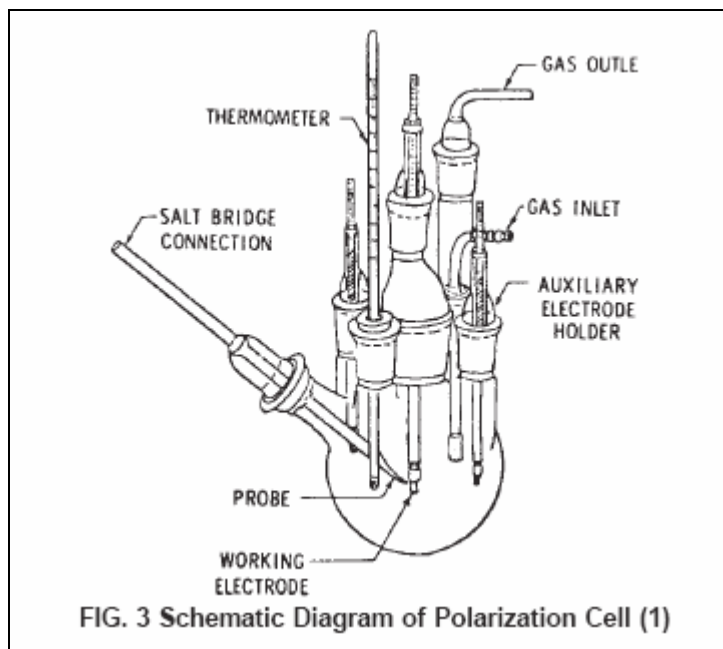


Figure 3.8 Schematic of polarization cell from ASTM standard G5.

Three basic experiments were carried out on the disk samples including cyclic polarization, linear polarization, and EIS tests. These tests were done following the ASTM standards for electrochemical measurements (G3-89, G5-94, G61-86, G106-89, etc.). The order of experiments was chosen to allow for as much data to be collected before the sample was destructively tested (cyclic polarization).

Tests were carried out in the following order: 1) Open circuit potential (OCP), 24-hour measurement of open circuit with a sample period every 10 seconds. 2) Electrochemical impedance spectroscopy (EIS) with a measurement frequency range from 100 kHz to 1 mHz. A voltage of 10 mV AC was used as the imposing signal with the DC voltage set to 0 mV versus the open circuit. 3) Polarization resistance with a scan rate of 0.1667 mV per second ranging ± 20 mV of the OCP, measured three times consecutively with five minutes between the end of one test and the beginning of another to allow for the cell to reach the OCP again. 4) Cyclic polarization using a scan rate of 0.1667 mV per second from -50 mV versus the OCP increasing up to 1.2 V versus the reference electrode or a max current density of 5 mA/cm^2 , then reversing back to the OCP. 5) A final EIS scan was conducted using the same measurement parameters as the initial EIS scan. This second EIS scan was performed to see how the behavior of the sample changed from before the cyclic polarization test to after the cyclic polarization

test. A solution pH measurement was taken before and after each test was completed. The testing configuration for solution and temperature level for each sample tested can be seen in Table 3.3.

Table 3.3 Testing solution and temperature for each disk sample.

Solution	30°C	60°C	90°C	105°C
SCW	E316L589 E316L600 E316L571	E316L583 E316L585	E316L593 E316L595 E316L569 001, 009 PEA0991-0994	
BSW	E316L591 E316L599		E316L586 E316L594 002, 003	
SSW			E316L588 E316L596 E316L570 005	
CaCl₂	E316L581			E316L584 004
Key: TiN coated: black . TiN/ZrO ₂ coated: red . Plain stainless steel: blue .				
Additional samples not tested				
Not tested:	E316L582 E316L587 E316L597	E316L598 SEM imaging	E316L592 Soaked in DI water	E316L590 SCW 90C early termination

The software used during experimentation and for analysis included Gamry Framework DC105 for corrosion testing, and Gamry EChem Analyst for data analysis. The Framework software provided a rapid non-destructive corrosion rate measurement and had a wide scan standard technique for most corrosion region studies as specified in ASTM standard G5.

An additional test was completed to test the performance of TiN against titanium itself. This test was performed after results from the coated titanium nitride were analyzed and compared to those results from plain 316L stainless steel to try and recognize if the performance was inherent of TiN or if it was the coating itself that led to the performance observed. Disk samples of titanium grade-12 were used and rather than coating a titanium sample with TiN, one sample was nitrated using a tube furnace with a

quartz tube, and nitrogen gas passed through an oxygen trap to remove any impurities. The titanium sample was placed inside the tube centered in the furnace, and nitrogen gas was passed through while the temperature was raised and held at 875°C for six hours. The nitrogen flow rate was held at 150 cubic centimeters per minute throughout the nitriding process. The nitrided sample became an orange-gold color, indicating a successful nitriding procedure.

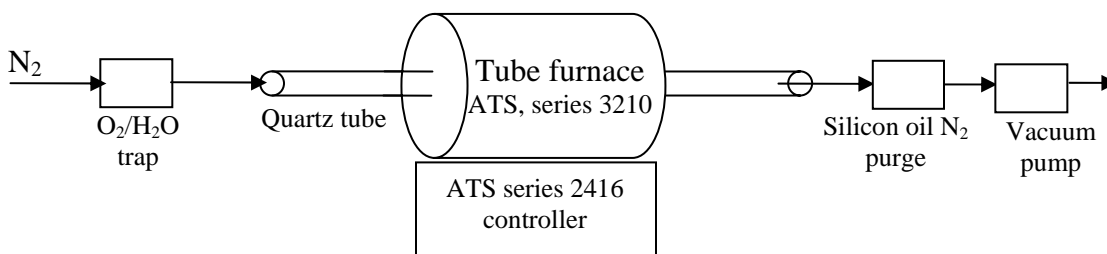


Figure 3.9 Titanium nitriding tube furnace block diagram.

3.1.2 Weight-loss Testing

The weight-loss samples were tested in the long term corrosion test facility where samples were immersed in an enclosed vessel holding the SCW solution at either 60°C or 90°C. The vessels, fiberglass tanks that have a total volume of ~2000 L, were filled with ~1000 L of aqueous test solution. The solution was held at either 60 °C or 90 °C and was covered with a blanket of air flowing at approximately 150 cm³ min⁻¹ (Farmer et. al, 2000). The coated weight loss samples were weighed and dimensioned (length, width, and thickness measurements) using calibrated electronic calipers (Fowler Ultra-Cal III, Sylvac) and scale (Mettler AT200, S/N 1115473441) before placing them inside the tanks. The calipers and scale recorded all measurements directly into a computer spreadsheet to prevent human error in transposing values. Samples were mounted on insulating racks and either submerged in the solution, placed at the water line, or fixed above the solution in the region of vapor concentration. The samples were located as described in Table 3.4 and kept inside the vessels for six months (July 29, 2004 – February 2, 2005). After being removed they were rinsed with de-ionized water and re-

Table 3.4 Sample ID and position in long-term corrosion SCW vessels.

Position	SCW 60°C	SCW 90°C
Submerged	E316L584	E316L587
	E316L585	E316L588
	E316L586	E316L589
Water-line	E316L593	E316L594
		E316L595
Vapor	E316L590	E316L581
	E316L591	E316L582
	E316L592	E316L583

weighed. The corrosion rate was calculated from the mathematical relationship as described previously.

It is important to recognize that the time for exposure of these samples is somewhat short compared to typical weight-loss sample tests performed at LLNL. These tests are sometimes carried out for years to get a good idea of general corrosion properties for specific samples of interest to Yucca Mountain.

3.2 Corrosion Testing Results

The corrosion testing results can be broken into four different components: cyclic polarization, polarization resistance, EIS, and weight-loss long term corrosion testing. Each of these has different meanings which are significant for various reasons. Cyclic polarization is related to localized corrosion, polarization resistance is related to general corrosion rates, EIS is related to the equivalent circuit for the sample, and the weight-loss samples are related to the general corrosion without active polarization being used. Pictures of all the samples after their corrosion testing are also provided in addition to the data and analysis in Appendix C.

3.2.1 Cyclic Polarization Results

The cyclic polarization results are reported using the important points found on the cyclic polarization curve (Figure 3.3) such as the open circuit potential, E_{corr} , the potential and current density at which the sample goes transpassive, and the potential and current density at which the sample re-passivates. These results, as consolidated from the

individual cyclic polarization curves, are presented using bar charts to show the comparison of solution and temperature cyclic polarization results. It should be noted, again, that the open circuit potential is the equilibrium potential of the cell after being at temperature for 24 hours without any applied potential. The passive region is the potential difference between the open circuit potential and the repassivation potential. This indicates that higher potential levels for the transpassive and repassivation are more desirable than lower values close to the open circuit. A low current density for the transpassive and repassivation positions is ideal because of its proportionality to corrosion rate. Figure 3.10 shows a compilation of cyclic polarization curves in 90°C SCW.

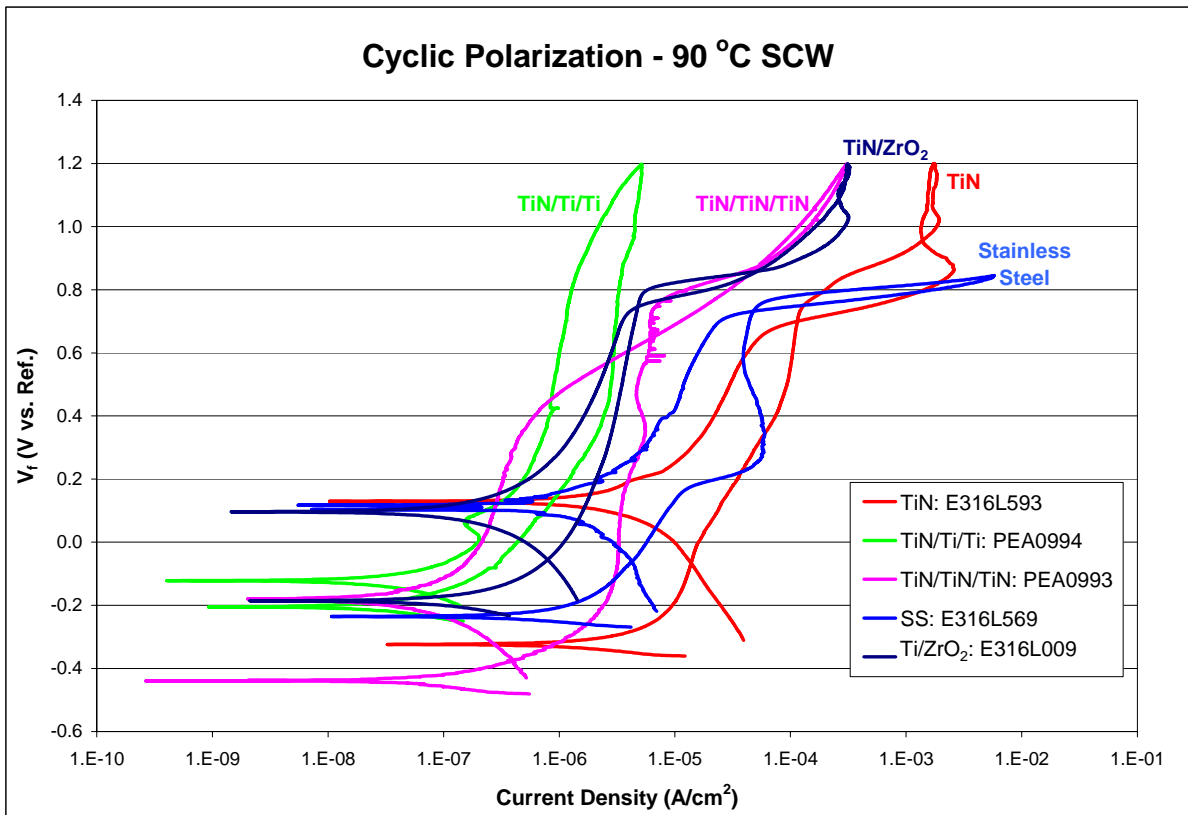


Figure 3.10 Selected cyclic polarization curves for 90°C SCW tests.

The bar chart presenting the potential values for the open circuit potential, transpassive region, and repassivation point of samples in SCW is shown in Figure 3.11. The cyclic polarization curves for samples tested in SCW indicate that TiN has a

relatively consistent passive region, with only a slight increase in repassivation potential for lower temperatures. The average passive region for TiN coated samples in SCW at 90 °C is 757.4 ± 341.8 mV. The potential value for repassivation is slightly higher for the two-layer coated samples with TiN + ZrO₂ (822.8 ± 107 mV). There was also an increase in the passive region for the mirror polished PEA samples to 1050 ± 31 mV. The sample with titanium coated as the top layer does not repassivate, as would be expected for titanium.

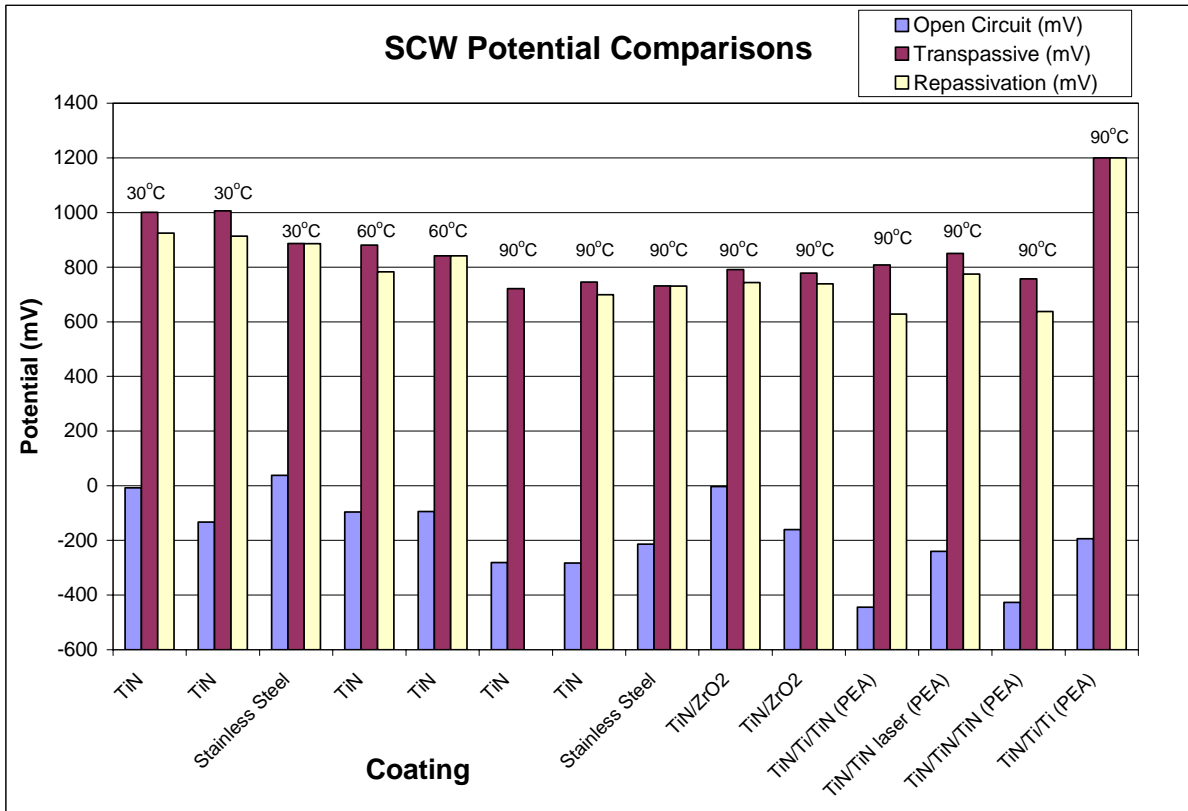


Figure 3.11 SCW potential comparisons for cyclic polarization corrosion tests.

The current density values where repassivation occurs are shown in Figure 3.12, and it is immediately obvious that multiple layers, whether they are TiN/ZrO₂ or multiple TiN layer, decrease the value of the current density. This decrease in current density indicates that there is also a decrease in corrosion rate for those samples with multiple coatings.

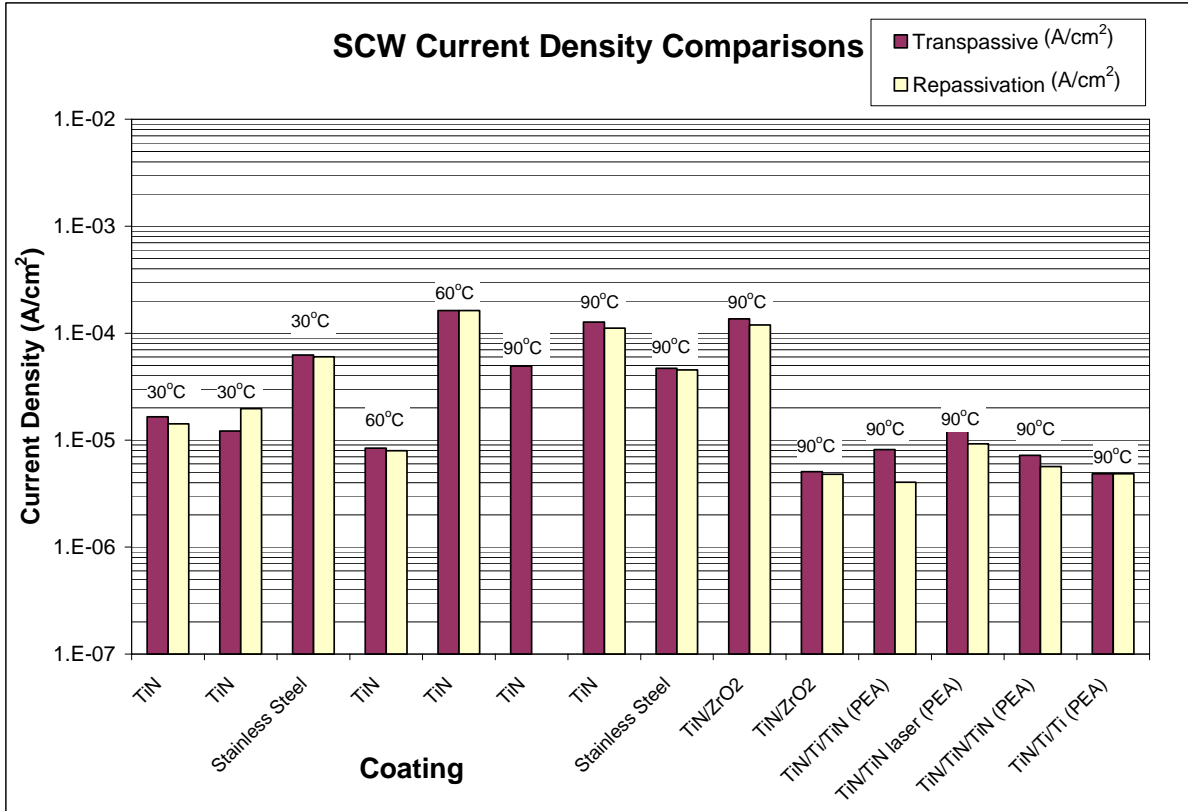


Figure 3.12 SCW current density comparisons for cyclic polarization corrosion tests.

Cyclic polarization curves from samples tested in the 90°C BSW solution are presented in Figure 3.13. Here, again, there is an obvious gain in passive layer protection and decrease in current density with the added ZrO₂ layer. Figure 3.14 presents the potential values for the open circuit potential, transpassive region, and repassivation point. The plain TiN coated samples have an average passive region of 407.9 ± 66.6 mV as compared to TiN/ZrO₂ coated samples with a passive region of 1002.2 ± 260 mV. Figure 3.15 presents the current density values for these points. The added ZrO₂ coating greatly increases the protection of the sample against this worst-case scenario for Yucca Mountain.

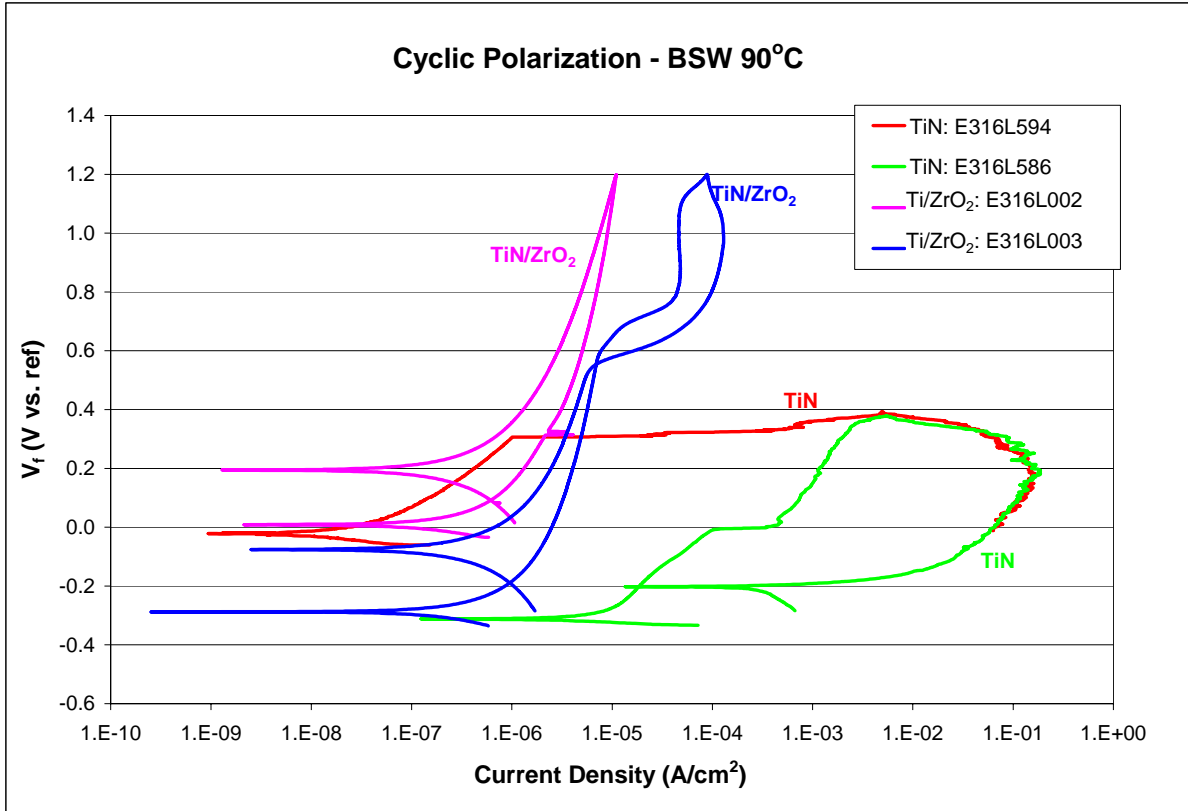


Figure 3.13 Cyclic polarization curves for 90°C BSW.

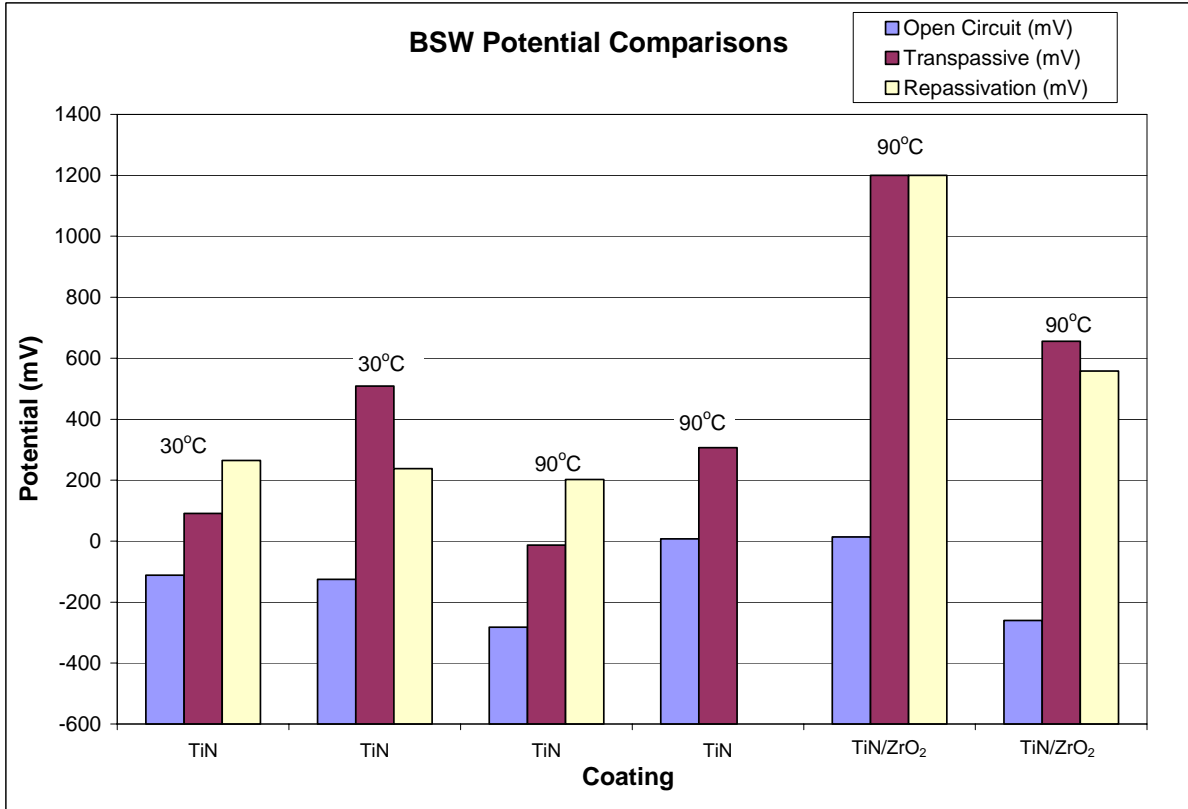


Figure 3.14 BSW potential comparisons for cyclic polarization corrosion tests.

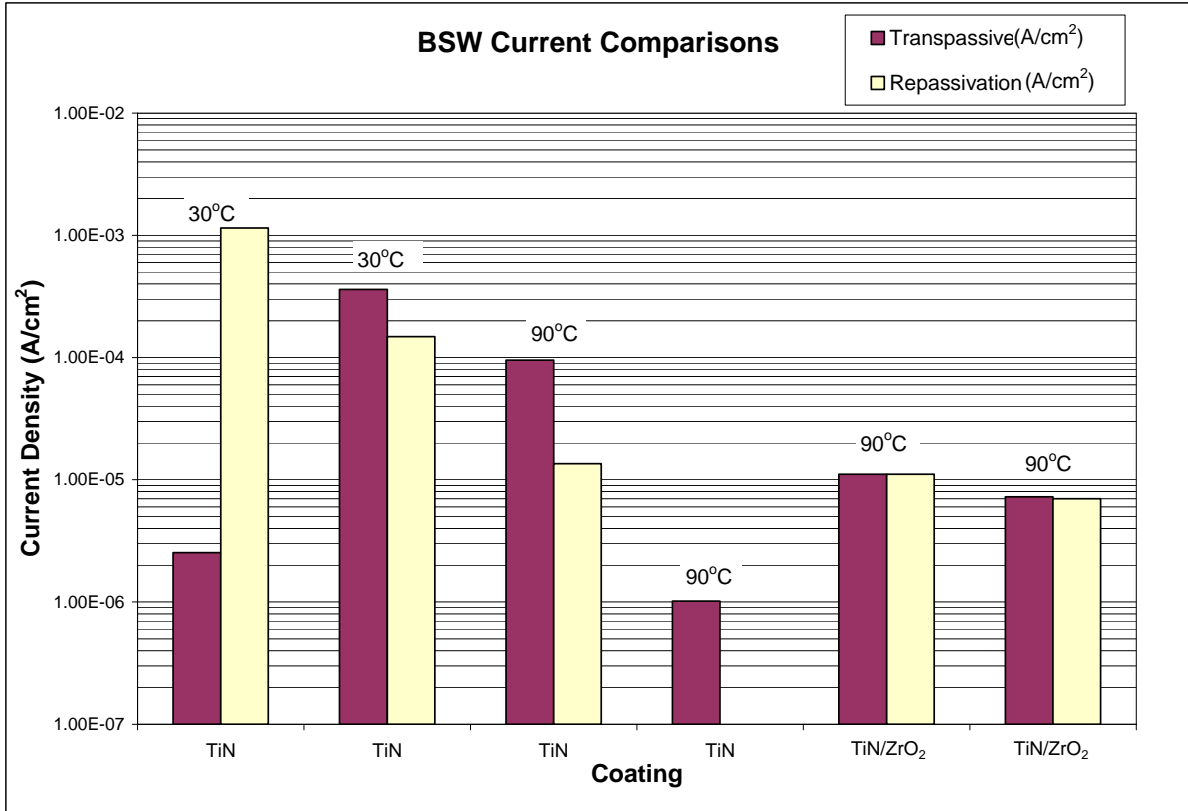


Figure 3.15 BSW current density comparisons for cyclic polarization corrosion tests.

Representative polarization curves and the bar charts for potential and current density values for SSW and 5M CaCl₂ solutions are shown in Figures 3.16 – 3.19. The 5M CaCl₂ is a harsh environment that attacked the samples, preventing any passive region to be formed for both the single and multiple layer coatings. SSW, also a harsh environment indicates rapid corrosive attack on a plain stainless steel sample and a single layer TiN coated sample. The second TiN coated sample tested in SSW did not behave in the same way as the first, indicating that there is some protection provided by the TiN, but more tests should be performed to confirm the behavior. The average passive region for TiN coated samples in SSW is 385 ± 288 mV. The two-layer coated sample indicated a larger passive region of 1063.7 ± 32.6 mV (one test) and lower current density at repassivation.

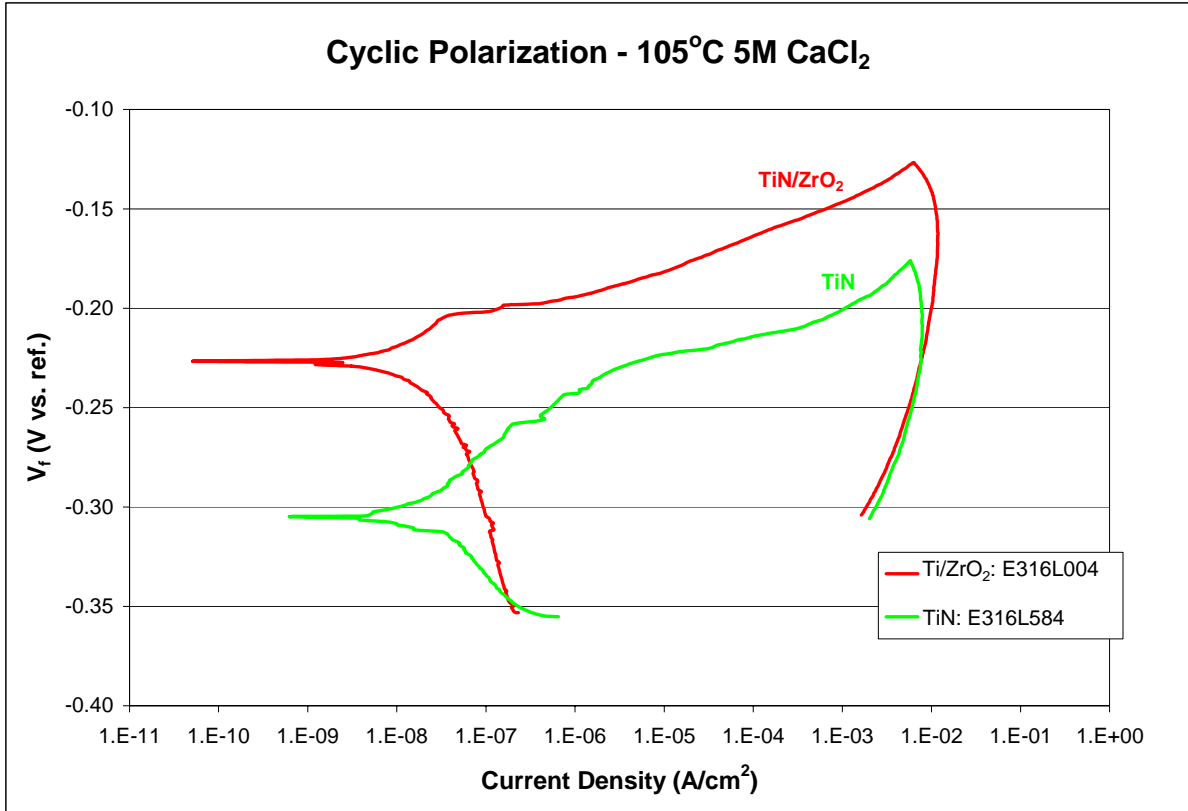


Figure 3.16 Cyclic polarization curves for 5M CaCl₂ at 105°C.

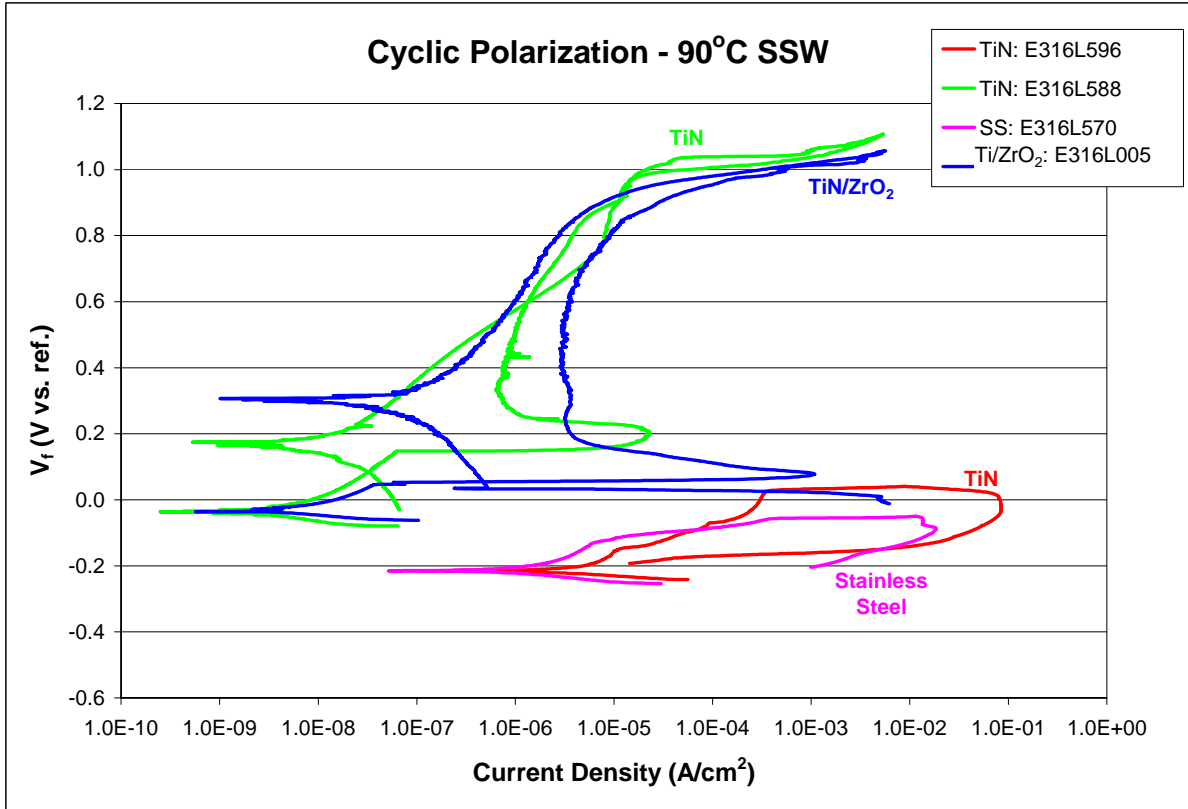


Figure 3.17 Cyclic polarization curves for SSW at 90°C.

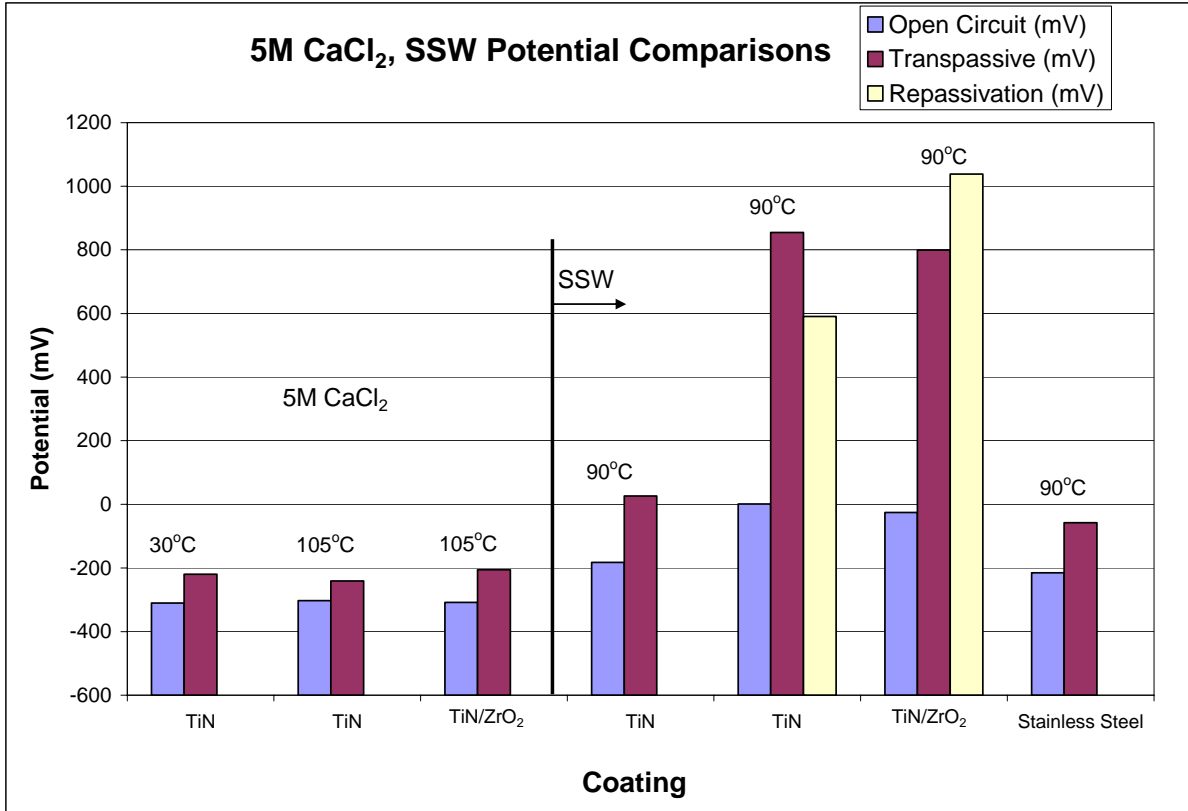


Figure 3.18 5M CaCl₂, SSW potential comparisons for cyclic polarization tests.

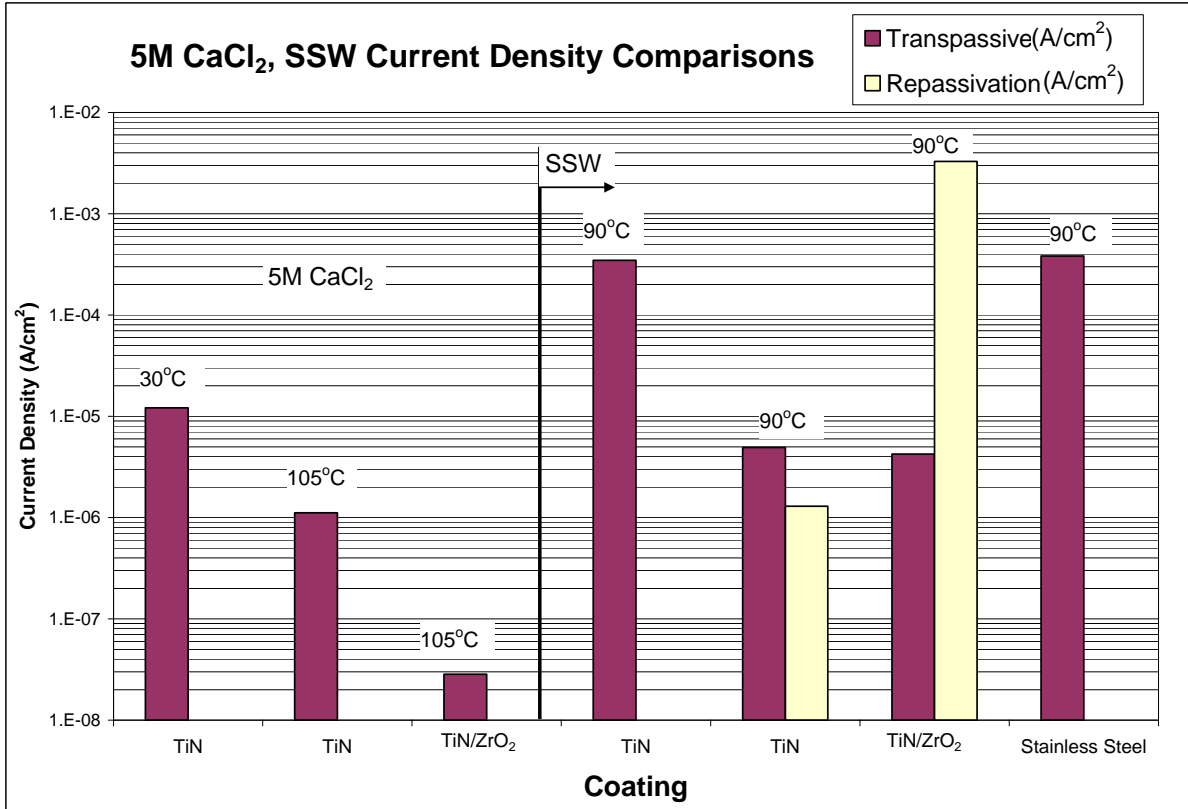


Figure 3.19 5M CaCl₂, SSW current density comparisons for cyclic polarization tests.

Comparing the average results for the high temperature solution environments, Figures 3.20 – 3.21, supports the implication that multiple coatings protect the sample by increasing the size of the passive region and decreasing the corrosion rate. The multiple coated samples with ZrO_2 as the top layer increased the passive region beyond the single coating passive region in BSW and SSW solutions. The multiple coatings on the mirror-polished PEA samples did not significantly increase the passive region, but did decrease the current density at repassivation in the SCW solution. The cyclic polarization curves for all tests performed at LLNL can be viewed in Appendix B.

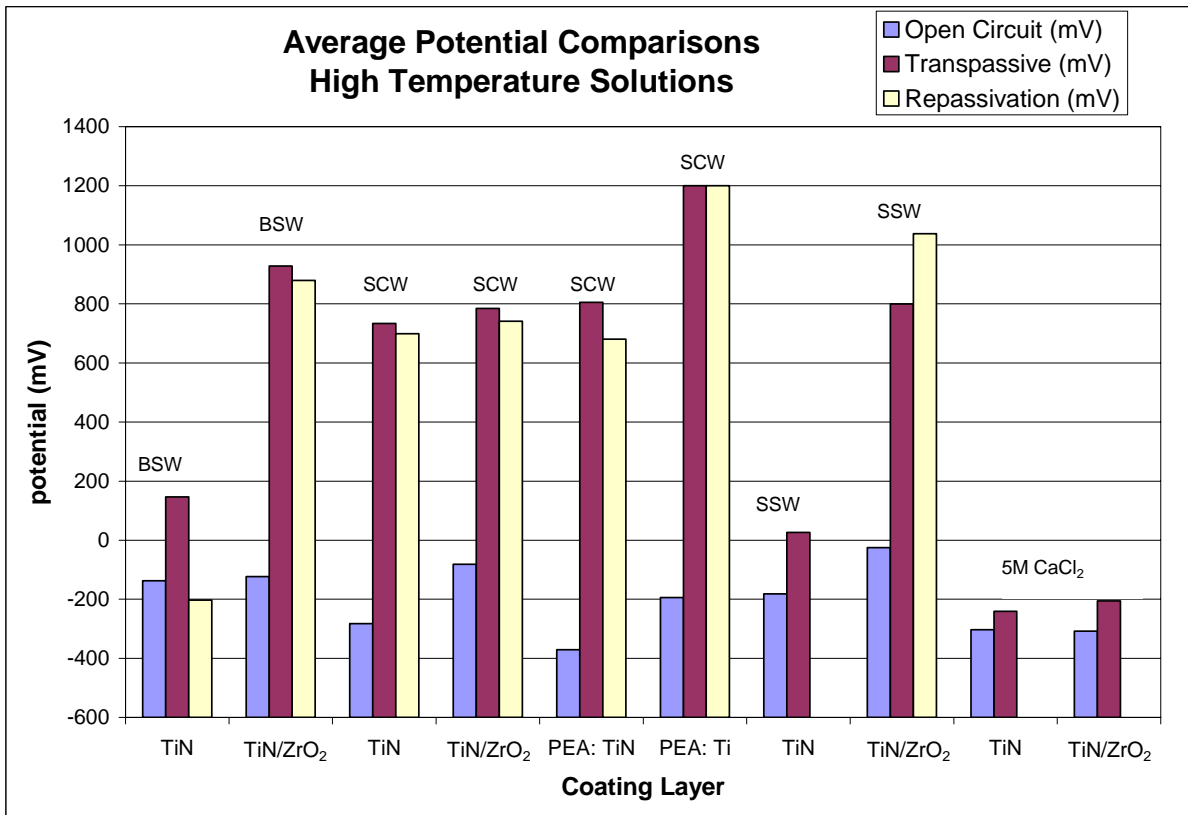


Figure 3.20 Average potential comparisons for cyclic polarization corrosion tests.

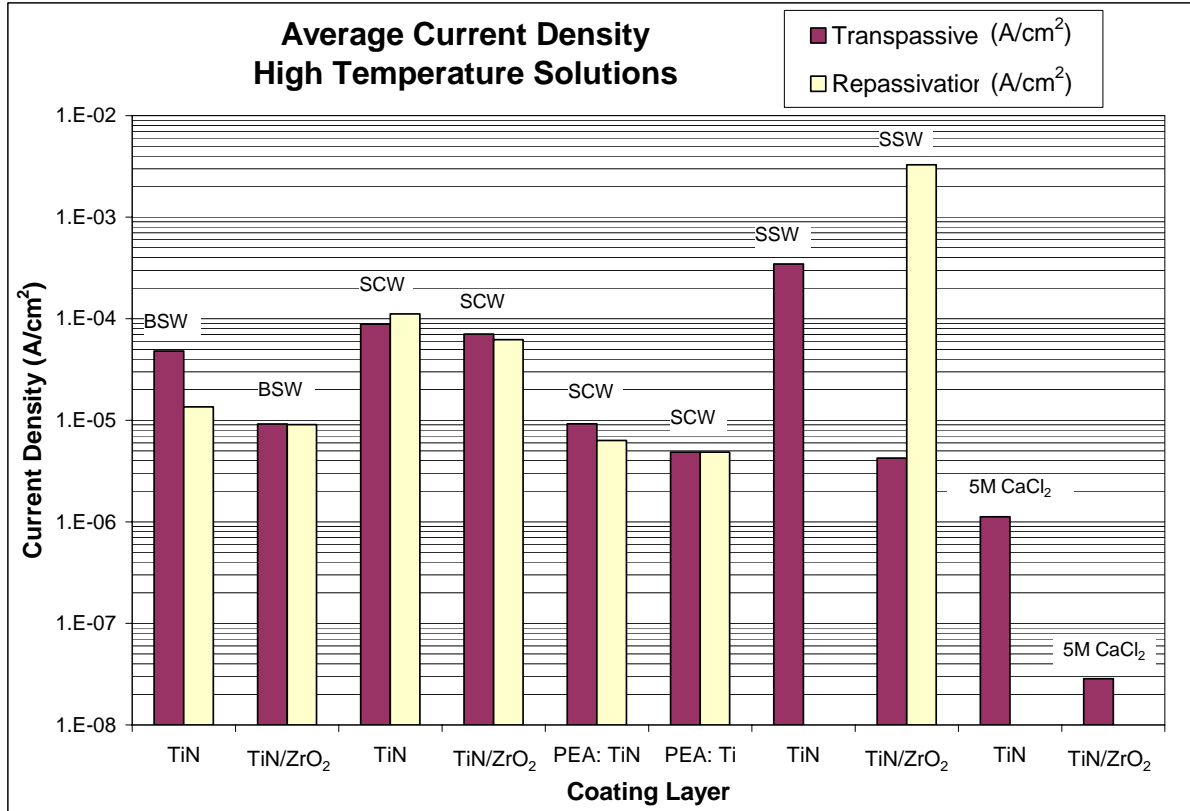


Figure 3.21 Average current density comparisons for cyclic polarization corrosion tests.

Pictures of all the disk samples after corrosion testing, arranged in a table to see exactly what solution and temperature they were tested in are shown in Figures 3.22-3.23. Individual pictures of the samples can be seen in Appendix C.

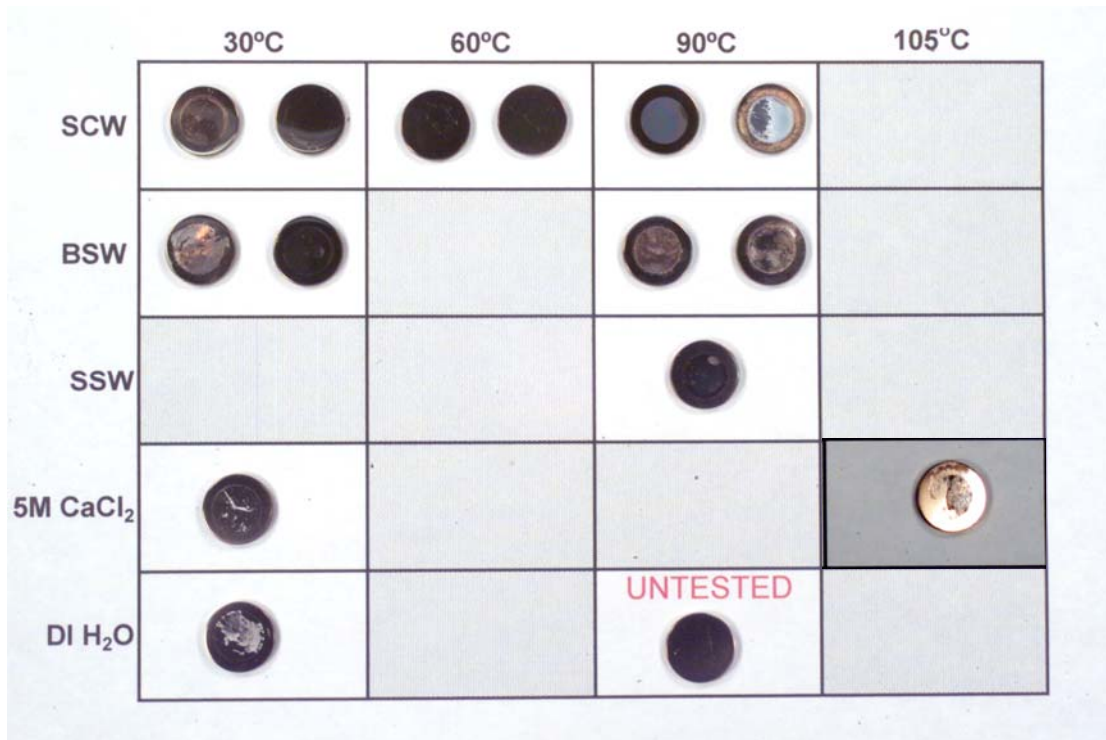


Figure 3.22 Matrix of TiN coated samples after corrosion tests showing solution and temperature level of testing.

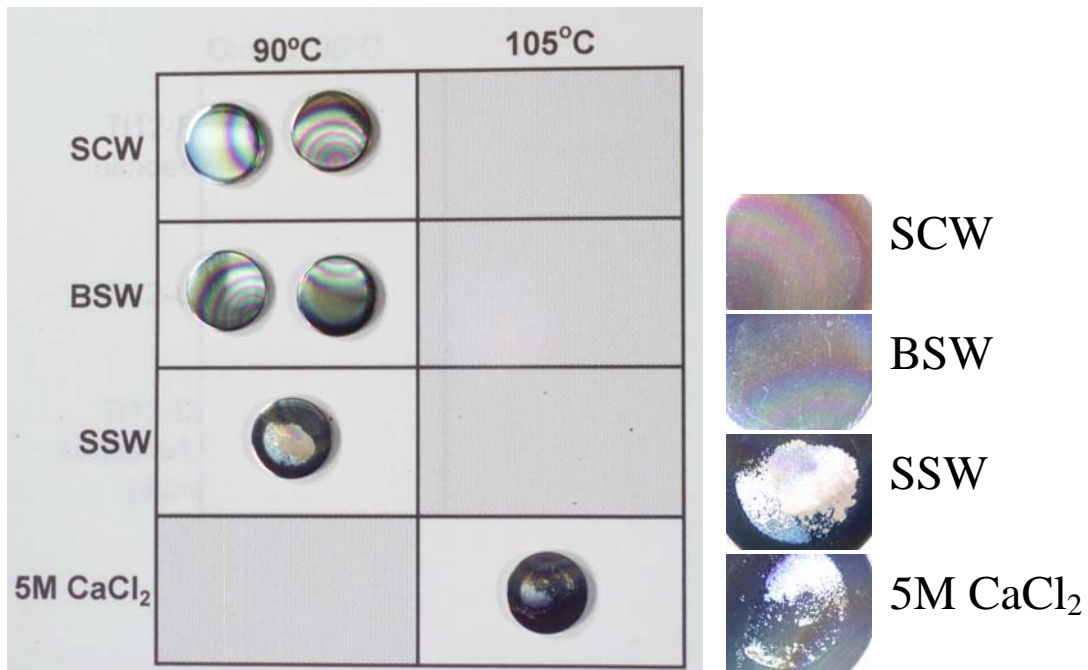


Figure 3.23 Matrix of TiN + ZrO₂ coated samples after corrosion testing showing solution and temperature level of test with zoomed in views of the sample surface.

Before and after optical microscope and SEM images were also taken of the mirror-polished PEA samples to aid in determining how the polarization testing was affecting the coating. These figures are shown at the end of this chapter.

The titanium sample that was nitrided using the tube furnace was compared against plain titanium using a test solution of oxalic acid, which actively corrodes titanium. Titanium is affected very little, if at all, by the concentrated solutions used in all the previous tests. The cyclic polarization curves and a combined photo of the samples can be seen in Figures 3.24 – 3.25.

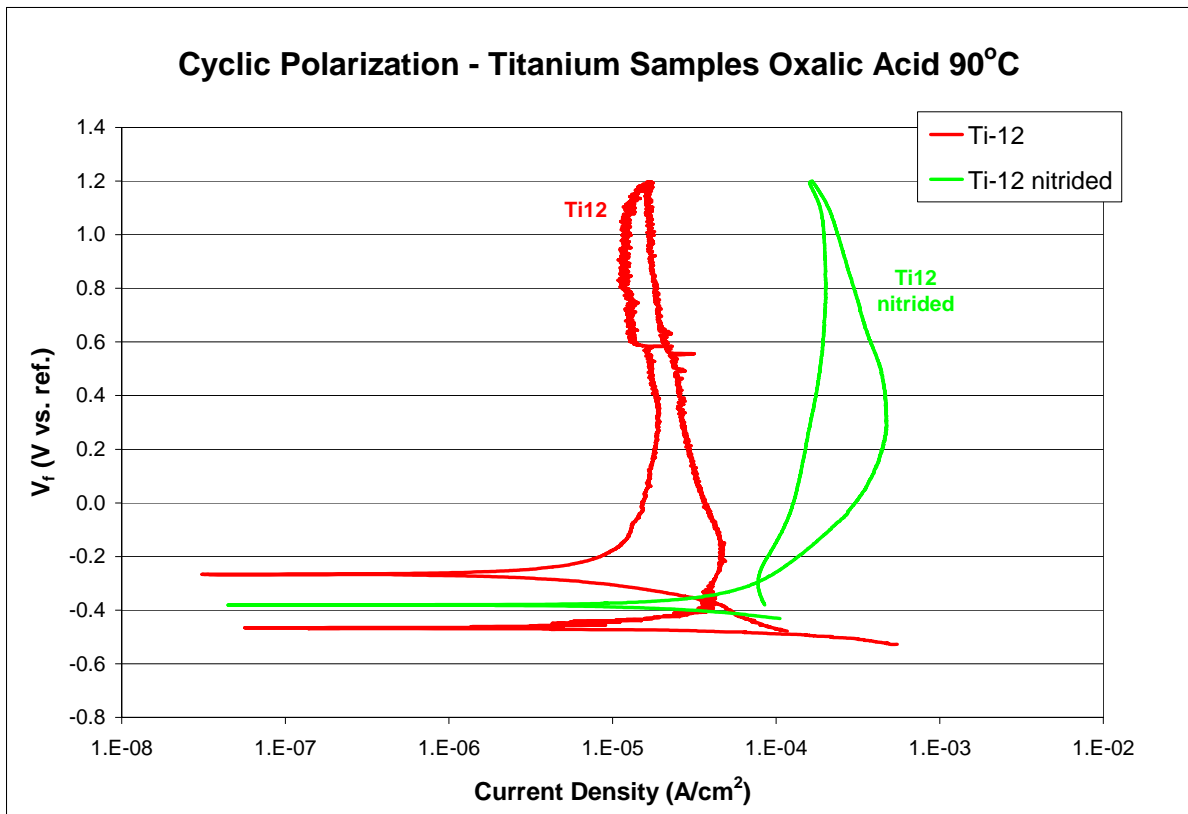


Figure 3.24 Cyclic polarization curves for plain Ti and nitrided Ti in oxalic acid.

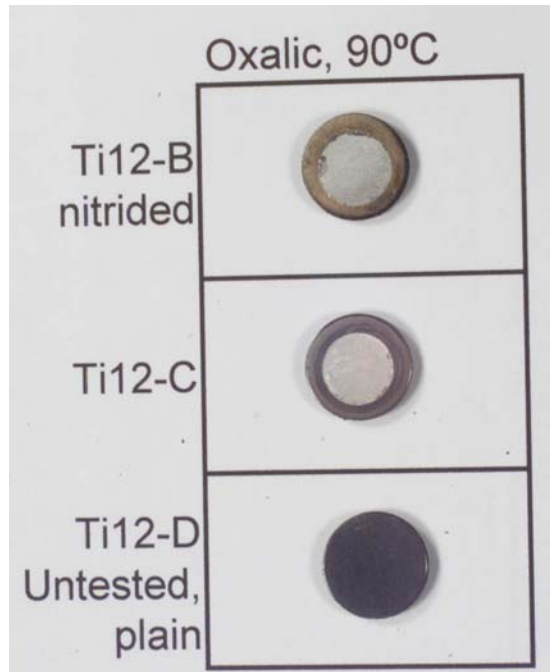


Figure 3.25 Matrix showing nitrided titanium and plain titanium after corrosion testing in oxalic acid.

Figure 3.25 shows images of the nitrided and titanium samples. The oxalic acid was able to corrode away the TiN. The cyclic polarization curve, Figure 3.24, shows that the current density for the nitrided sample is higher than the plain titanium sample, which indicates a higher corrosion rate for titanium nitride than for titanium.

3.2.2 Polarization Resistance Results

The polarization resistance results were obtained using the Gamry^R EchemAnalyst software package that calculates the corrosion rate using the resistance curve and the specific properties of the sample. For each sample, the three polarization resistance corrosion rates were averaged to report a single corrosion rate. These are displayed through a bar chart to aid in comparison of the different solution and temperature environments tested. Figures 3.26 - 3.27 support the corrosion rate estimates as compared to the current density values from the cyclic polarization tests, showing that the multiple coated samples have lower corrosion rates than the single coated TiN samples. These quantitative numbers are difficult to understand for thin-film coatings because a corrosion rate of tens or hundreds of microns per year will easily destroy the coating in

much less than a year. It is also important to note that the solutions tested were highly concentrated, which could indicate a higher corrosion rate than would actually be observed. The corrosion rate as measured through the weight loss samples is more realistic for these thin-film coatings.

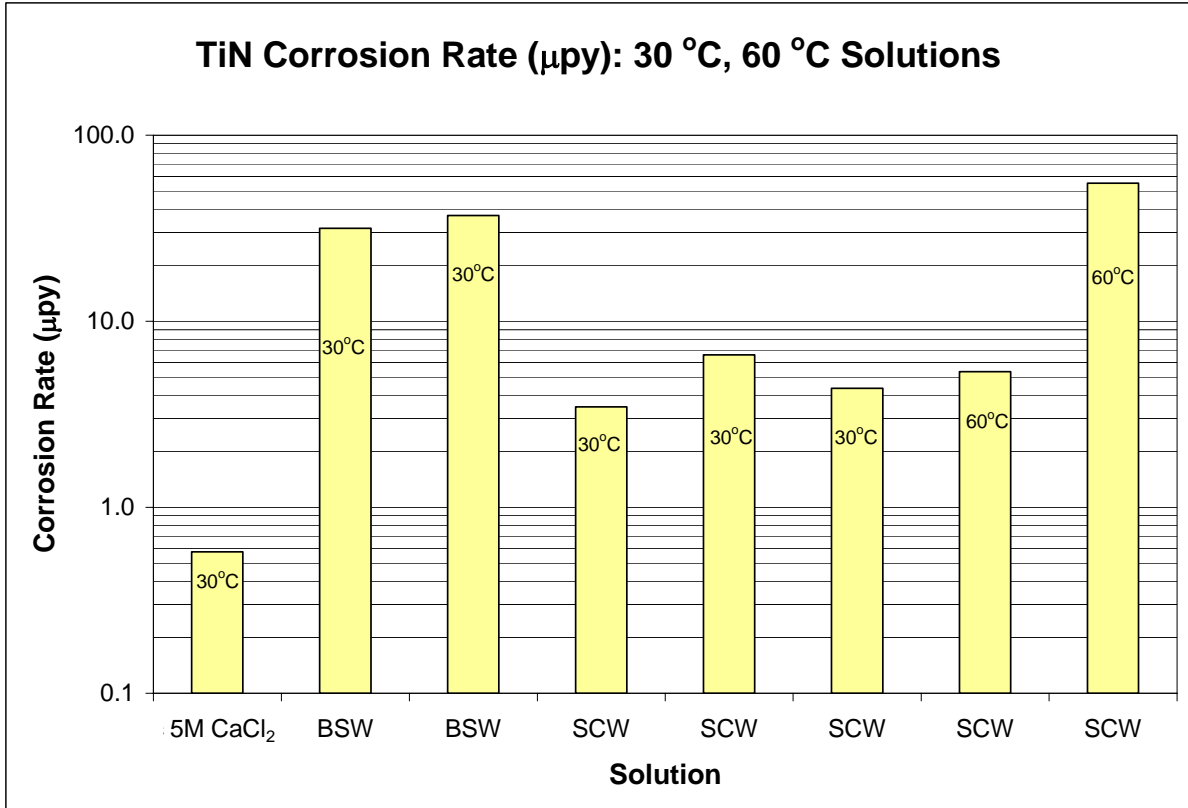


Figure 3.26 TiN corrosion rate from polarization resistance tests in 30°C and 60 °C solutions.

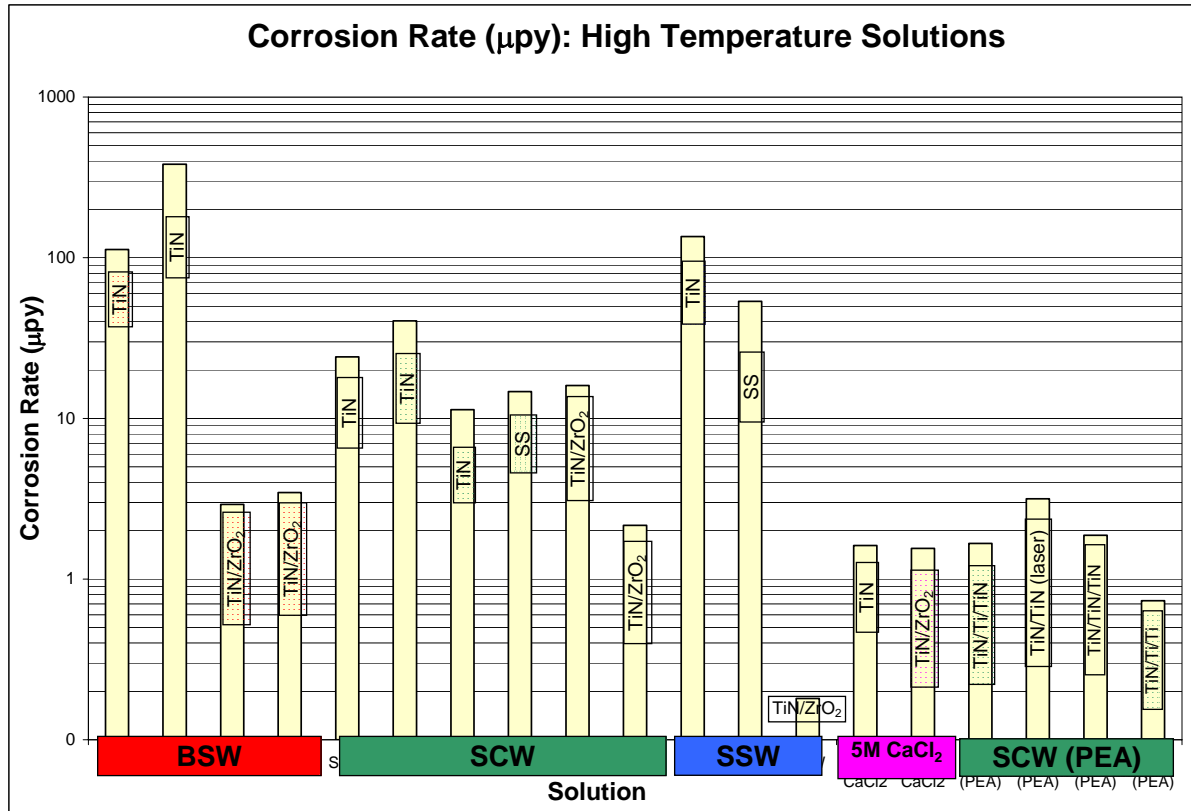


Figure 3.27 Corrosion rates as calculated from polarization resistance tests in high temperature solutions.

3.2.3 Electrochemical Impedance Results

The EIS results obtained have not proven anything that is well defined and comparable for sample tests. Several different equivalent circuit models were used for all of the EIS tests completed to see which model would describe the sample and cell most accurately. It was not found to be a useful method of analysis. Theoretically the circuit element values should be the same for each solution type and vary only between solutions. The circuit element values calculated using the EChem Analyst software varied significantly, often having standard deviations several orders of magnitude larger than the calculated circuit element value.

The analysis done was of a more theoretical nature, using a semi-empirical technique to investigate a specific model of the simplest kind. This analysis assumed a resistive-capacitive model and was performed using equivalent circuit elements. Although several circuit models have been proposed (Liu, 2003), the simple circuit of Figure 3.28 was selected for analysis. This circuit represents a solution resistance R_s , a double layer

capacitance C , and a corrosion resistance R_L (charge transfer resistance). The double layer capacitance and corrosion resistance are coupled in parallel as the impedance Z_L , which is in series with the solution resistance R_S .

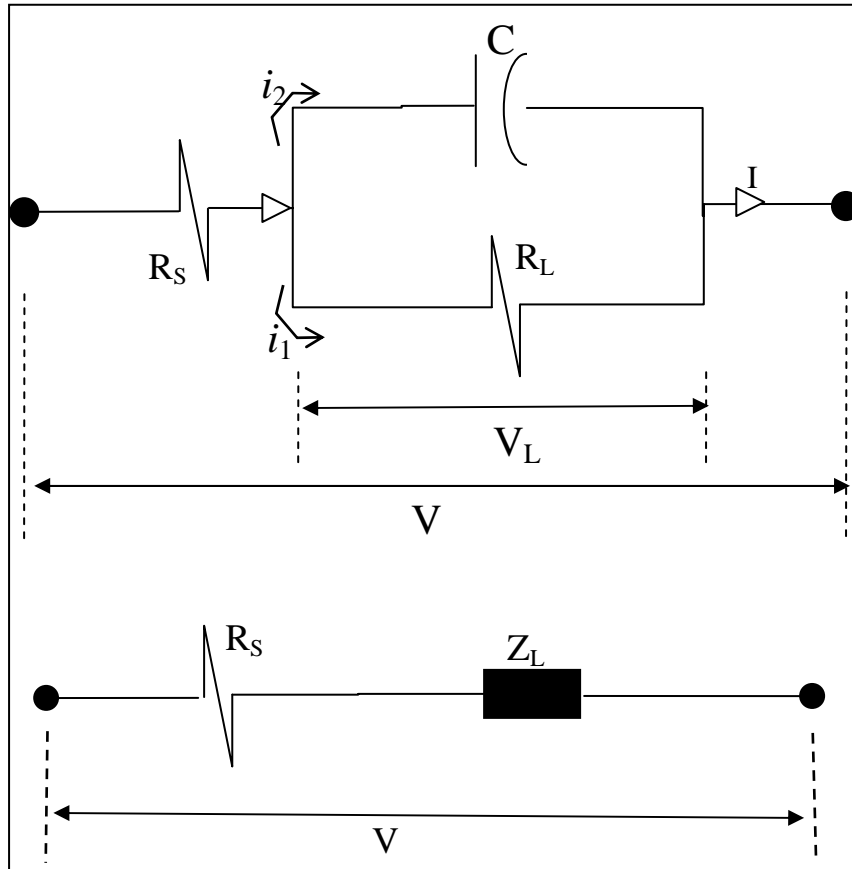


Figure 3.28 Equivalent circuit showing current flow, and broken down into solution resistance and impedance.

The impedance Z_L is given by the following equation for an oscillatory form of voltage ($\sim e^{j\omega t}$), and thus it is expressed in terms of the complex form

$$\frac{1}{Z_L} = \frac{1}{R_L(i)} + j\omega C = \frac{1 + j\omega R_L C}{R_L(i)}$$

where $j\omega C$ denotes the reactance of the capacitor. The voltage-current relation, in complex form, is then given by:

$$V = \left(R_S + \frac{R_L(i)}{1 + j\omega R_L C} \right) I$$

The total impedance could be written in terms of an equivalent resistance represented by the REAL of Z_L , Re , and equivalent reactance represented by the IMAGINARY of Z_L , Im . Rearranging the terms of Re and Im one obtains

$$\text{Re}(Z_L) = \frac{(R_L + R_S) + \omega^2 C^2 R_L^2 R_S}{1 + \omega^2 C^2 R_L^2} \quad \text{Im}(Z_L) = \frac{-\omega C R_L^2}{1 + \omega^2 C^2 R_L^2}$$

These real and imaginary parts of the total resistance can be simplified even further using the following two assumptions:

Case I:

$$\text{for } \omega^2 C^2 R_L^2 \geq 1$$

$$\text{Re}(Z_L) \approx \frac{(R_L + R_S) + \omega^2 C^2 R_L^2 R_S}{\omega^2 C^2 R_L^2} \quad \text{Im}(Z_L) = \frac{-\omega C R_L}{\omega^2 C^2 R_L^2}$$

Case II:

$$\text{for } \omega^2 C^2 R_L^2 \leq 1$$

$$\text{Re}(Z_L) \approx \frac{(R_L + R_S) + \omega^2 C^2 R_L^2 R_S}{1} \quad \text{Im}(Z_L) = \frac{-\omega C R_L}{1}$$

These relationships were used to determine the behavior of the equivalent circuit in the EIS experiments performed on the disk samples. The impedance's real part was used to observe the dependence of the impedance on the frequency, because the real part is what is measured in the Bode plot. In order to use these relationships, a rough estimate of the capacitance of the coating was made using:

$$C = \varepsilon \frac{\pi r^2}{\delta} \approx 1.8 \text{ nF}$$

where ε is the permittivity of space, equal to $10\text{E-}9 * (36\pi)^{-1}$, r is the radius of the disk, and δ is the thickness of the coating. Using the same frequency range as used in the experimental analysis, 1 mHz – 1 MHz, a range can be calculated for ωC :

$$\begin{aligned} (\omega C)_{\text{low}} &= 2\pi fC = 2\pi (10^{-3} \text{ Hz}) (1.8 \times 10^{-9} \text{ F}) = 3.6\pi \times 10^{-12} \\ (\omega C)_{\text{mid-low}} &= 2\pi fC = 2\pi (10^{-1} \text{ Hz}) (1.8 \times 10^{-9} \text{ F}) = 3.6\pi \times 10^{-10} \\ (\omega C)_{\text{mid}} &= 2\pi fC = 2\pi (10^1 \text{ Hz}) (1.8 \times 10^{-9} \text{ F}) = 3.6\pi \times 10^{-8} \\ (\omega C)_{\text{mid-high}} &= 2\pi fC = 2\pi (10^3 \text{ Hz}) (1.8 \times 10^{-9} \text{ F}) = 3.6\pi \times 10^{-6} \\ (\omega C)_{\text{high}} &= 2\pi fC = 2\pi (10^5 \text{ Hz}) (1.8 \times 10^{-9} \text{ F}) = 3.6\pi \times 10^{-4} \end{aligned}$$

This indicates that the range is very small, and when inserted into the equation for the $\text{Re}(Z_L)$, Case II is dominant for most of the range. For Case I to become dominant at the high range, the charge transfer resistance must be on the order of Mega-ohms.

Taking the equation for the real part for both cases from above, and solving for R_L gives the following equations:

Case I:

$$\text{Re}(R_T) \approx Z \approx \frac{(R_L + R_S) + \omega^2 C^2 R_L^2 R_S}{\omega^2 C^2 R_L^2} = \frac{R_L + R_S}{\omega^2 C^2 R_L^2} + R_S$$

This leads to a quadratic equation for R_L , and thus:

$$R_L^2 - \frac{R_L}{\omega^2 C^2 (Z - R_S)} - \frac{R_S}{\omega^2 C^2 (Z - R_S)} = 0$$

$$R_L = -\frac{1}{2\omega^2 C^2 (Z - R_S)} \pm \sqrt{\frac{1}{4\omega^4 C^4 (Z - R_S)^2} + \frac{R_S}{\omega^2 C^2 (Z - R_S)}}$$

Case II:

$$\text{Re}(R_T) \approx Z \approx (R_L + R_S) + \omega^2 C^2 R_L^2 R_S$$

Again leading to a quadratic equation for R_L :

$$R_L^2 - \frac{R_L}{\omega^2 C^2 R_S} - \frac{R_S - Z}{\omega^2 C^2 R_S} = 0$$

$$R_L = -\frac{1}{2\omega^2 C^2 R_S} \pm \sqrt{\frac{1}{4\omega^4 C^4 R_S^2} + \frac{R_S - Z}{\omega^2 C^2 R_S}}$$

All of these equations for R_L can be solved by making an assumption for R_S and plugging in the values obtained from the experimental Bode plots. The solution for R_L using the phase angle was further investigated to observe the relationship between R_L , the imaginary part of the impedance, and the measured impedance to the frequency range applied. The phase angle is the ratio of the imaginary to the real part of the impedance:

$$\phi = \frac{\text{Im}(R_T)}{\text{Re}(R_T)} \quad \text{phase angle}$$

Case I, II:

$$\phi = \frac{-\omega C R_L^2}{1 + \omega^2 C^2 R_L^2} \times \frac{1 + \omega^2 C^2 R_L^2}{R_L + R_S (1 + \omega^2 C^2 R_L^2)} = \frac{-\omega C R_L}{R_L + R_S (1 + \omega^2 C^2 R_L^2)}$$

Solving for R_L :

$$R_L = \frac{\phi}{2\omega C} \pm \frac{1}{2} \sqrt{\frac{\phi}{\omega C} \left(\frac{\phi}{\omega C} - 4R_S \right)}$$

the phase angle can be reduced to two different equations, one for low frequencies and one for high frequencies assuming that R_L is in the range of 10 k Ω :

$$\text{at high frequency: } \omega C = 3.6\text{E-4} \quad \phi \approx \frac{\omega C R_L^2}{R_L + 2R_S}$$

$$\text{at low frequency: } \omega C = 3.6\text{E-12} \quad \phi \approx \frac{\omega C R_L^2}{R_L + R_S}$$

From this, an estimate for the term inside the square root symbol of the equation for R_L can be estimated by dividing ϕ by ωC in order to find an approximate magnitude.

$$\text{at high frequencies: } \omega C = 3.6\text{E-4} \quad \frac{\phi}{\omega C} \approx \frac{\omega C R_L^2}{(R_L + 2R_S)\omega C} \approx \frac{R_L^2}{R_L + 2R_S}$$

$$\text{at low frequencies: } \omega C = 3.6\text{E-12} \quad \frac{\phi}{\omega C} \approx \frac{\omega C R_L^2}{(R_L + R_S)\omega C} \approx \frac{R_L^2}{R_L + R_S}$$

The range of the phase angle as seen from an experimental bode plot is from 10^{-1} radians at the middle frequencies to 1.5 radians at low and high frequencies. This leads to a range in magnitude of 1.5E4 up to 1.5E12 for the phase angle divided by ωC . These values are likely much greater than $4R_S$, under the assumption that R_S cannot be much larger than 10 Ω . Therefore,

$$R_L = \frac{\phi}{2\omega C} \pm \frac{1}{2} \sqrt{\frac{\phi}{\omega C} \left(\frac{\phi}{\omega C} - 4R_S \right)} \approx \frac{\phi}{2\omega C} \pm \frac{1}{2} \frac{\phi}{\omega C} \approx 0 \quad , \quad \frac{\phi}{\omega C}$$

The zero solution is a trivial solution that is not useful, therefore the second solution will be investigated further. A plot of the normalized values for R_L , estimated above, the imaginary term for the impedance using Case II, and the actual experimental impedance values versus the frequency in Hz can be seen in Figure 3.29.

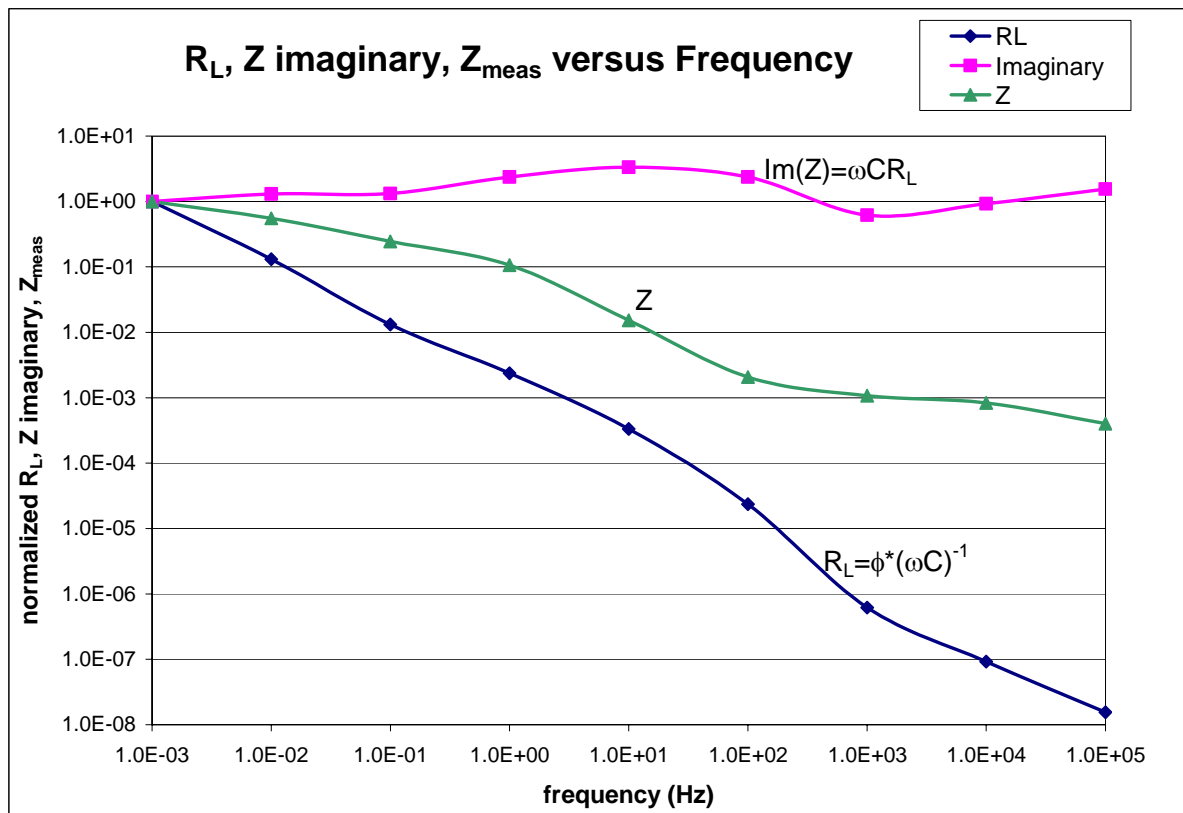


Figure 3.29 R_L , Z imaginary from Case II, and the measured impedance, Z , plotted versus frequency (Hz).

Figure 3.29 indicates little change in the imaginary term for impedance, and an overall decreasing trend for the experimental impedance measured. The corrosion resistance, R_L , as estimated from the experimental phase angle, is also decreasing in magnitude. This decrease in the magnitude of the corrosion resistance indicates an increase in reactance of the double layer capacitance. Table 3.5 shows the data used to produce the normalized plots in Figure 3.29. The values for R_L , Z imaginary, and Z_{meas} were normalized to the value corresponding to the lowest frequency.

Table 3.5 Values for plots in Figure 3.29.

f (Hz)	ϕ	ω	ω^*C	$\phi/(\omega^*C)=R_L$	$\omega^*C^*R_L$	Z
1.0E+05	0.63	6.28E+05	1.13E-03	5.55E+02	6.28E-01	3.51E+00
1.0E+04	0.38	6.28E+04	1.13E-04	3.32E+03	3.75E-01	7.27E+00
1.0E+03	0.25	6.28E+03	1.13E-05	2.23E+04	2.52E-01	9.36E+00
1.0E+02	0.96	6.28E+02	1.13E-06	8.48E+05	9.59E-01	1.82E+01
1.0E+01	1.35	6.28E+01	1.13E-07	1.20E+07	1.35E+00	1.33E+02
1.0E+00	0.96	6.28E+00	1.13E-08	8.48E+07	9.60E-01	9.28E+02
1.0E-01	0.54	6.28E-01	1.13E-09	4.74E+08	5.37E-01	2.15E+03
1.0E-02	0.53	6.28E-02	1.13E-10	4.69E+09	5.30E-01	4.85E+03
1.0E-03	0.41	6.28E-03	1.13E-11	3.59E+10	4.06E-01	8.73E+03

This brief analysis has been done to explore magnitudes and try to get a better idea for how the simple equivalent circuit matches the experimental values. It has also been a useful exercise in recognizing the relationship of the equivalent circuit to the mathematical description. This equivalent circuit may be too simple to adequately represent the experimental data, and more information about the circuit elements and how they relate to the actual corrosion cell would be helpful in fully analyzing this data.

3.2.4 Weight-loss Results

The weight-loss samples were collected from the LTCTF after being inside the tanks for 6-months. The table of data collected both before and after insertion in the tanks can be seen in Table 3.6. The calculations for corrosion rate were performed as described in the introduction to this chapter, using an exposure time of ½ year, the density of 316L stainless steel (8 g cm⁻³), and an exposed surface area of approximately 28.11 cm² (1 in. x 2 in. x 1/8 in. minus ~r = 0.25 in. center hole and mounting area). The exact surface area exposed was calculated using the dimensional measurement data collected before tank exposure. Pictures of a sample from each environment are shown in Figure 3.31, with pictures of all the weight-loss samples located in Appendix C.

Table 3.6 Weight-loss sample data and corrosion rate.

Sample ID	Exposure Condition	Mass before exposure (g)	Mass after exposure (g)	difference <i>w</i> (g)	Corr. Rate μpy	average corr. rate (μpy)
W316I581	90°C Vapor SCW	29.4915	29.4917	-0.0002	-0.0220	-0.024 ± 0.027
W316I582		29.4820	29.4819	0.0000	0.0016	
W316I583		29.6282	29.6288	-0.0006	-0.0527	
W316I584	60°C Aqueous SCW	29.5706	29.5709	-0.0004	-0.0336	0.044 ± 0.083
W316I585		29.4496	29.4492	0.0004	0.0354	
W316I586		29.4264	29.4249	0.0015	0.1311	
W316I587	90°C Aqueous SCW	29.5083	29.5022	0.0060	0.5297	0.462 ± 0.063
W316I588		29.4462	29.4410	0.0051	0.4511	
W316I589		29.5168	29.5122	0.0046	0.4059	
W316I590	60°C Vapor SCW	29.2202	29.2201	0.0001	0.0060	0.0138 ± 0.011
W316I591		29.3830	29.3829	0.0001	0.0089	
W316I592		29.5896	29.5893	0.0003	0.0266	
W316I593	60°C WaterLine SCW	29.6419	29.6417	0.0002	0.0177	0.017 ± 0.133
W316I594	90°C WaterLine SCW	29.6231	29.6212	0.0019	0.1646	0.170 ± 0.008
W316I595		29.4619	29.4599	0.0020	0.1753	



Figure 3.30 Weight-loss samples after removal from corrosion tanks at LLNL (Fix, 2005).

The quantitative weight-loss corrosion rate results indicate that the TiN does not corrode at too high a rate. The negative corrosion rates indicate an increase in weight or a buildup of corrosion products that were not rinsed away with the DI water. This needs to be considered when reviewing the corrosion rates because it does decrease the overall accuracy of the results. The pictures indicate more clearly that the high temperature aqueous environment is corrosive enough to strip away the TiN coating from the substrate. The samples in the vapor environments at both 60°C and 90°C do not show

that the TiN coating was corroded as actively as those samples that were submerged in 90°C. Even the samples submerged and at the water line in the 60°C tank do not appear stripped of the TiN coating.

3.2.5 Optical and SEM Images

The PEA samples were analyzed with both an optical microscope and a scanning electron microscope before and after they were corrosion tested. This was done in order to gain a better understanding of how the coating was being corroded. The following figures present the pre and post corrosion properties of the coatings on the PEA samples. It should be noted that the images for pre and post corrosion are not in the exact same location for each sample. Each is a general image from the center of the sample.

PEA0991 – TiN/Ti/TiN

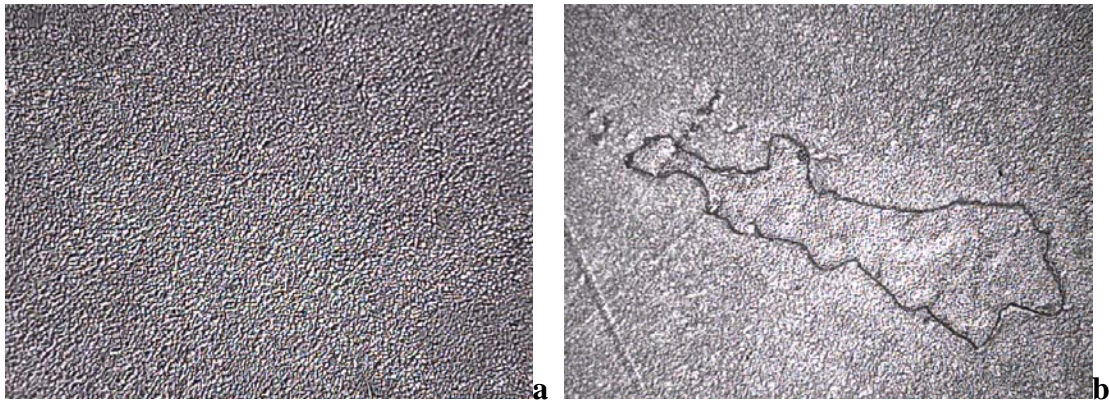


Figure 3.31 1000X optical **a)** pre-corrosion and **b)** post corrosion

The optical images for PEA0991 with the TiN + Ti + TiN coated layers indicate that the solution did attack the coating, with portions stripped completely away. The coating also appears to be not as dark as the pre corrosion image indicating that there is less uniformity in the coated layer after corrosion. The SEM elemental analysis (Figure 3.32) is a post corrosion image that indicates there are areas that no longer have TiN protecting the substrate as seen by the dark spot in the image.

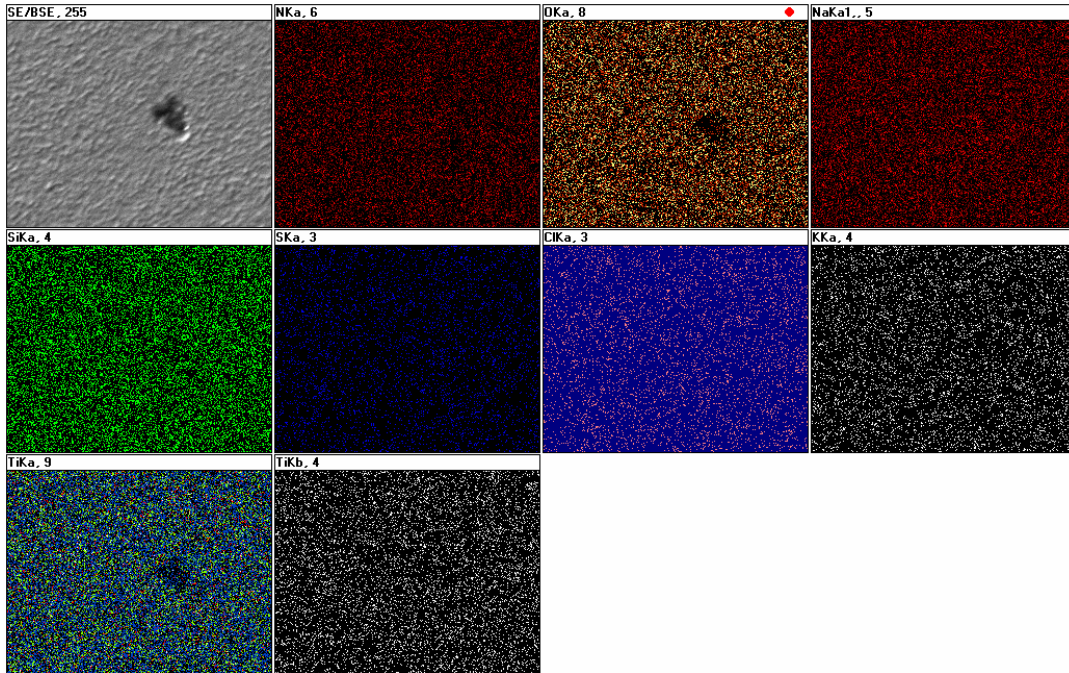


Figure 3.32 SEM elemental analysis, 2000X post corrosion – dark area indicates crater where TiN is absent and Oxygen is present.

PEA0992 – TiN/TiN (laser)

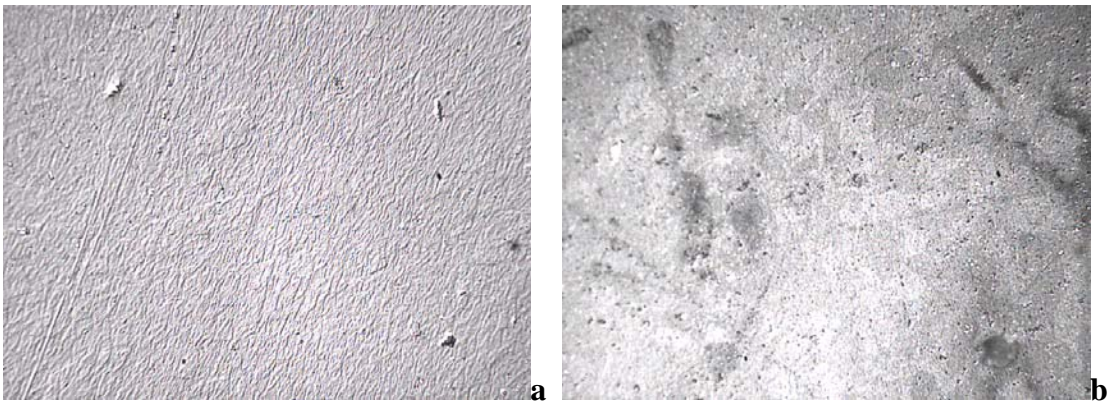


Figure 3.33 1000X optical a) pre-corrosion and b) post corrosion

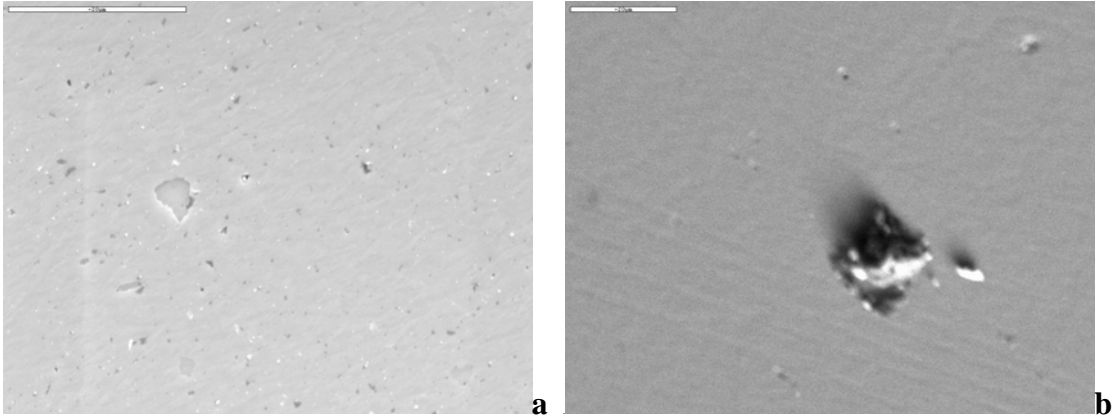


Figure 3.34 SEM image **a)** 2000X pre-corrosion and **b)** 1200X post-corrosion.

The optical image for PEA0992 (Figure 3.33) indicates a significant difference in surface characteristics after corrosion testing. There are visible pits in the sample that come from active corrosion occurring on the surface. The SEM images of PEA0992 (Figure 3.34) show that the pre-corrosion surface was not a continuous surface but the two layers appear to complement each other by protecting the unprotected areas of the other coating. The post corrosion SEM has smoother surface characteristics that are likely due to the difference in magnification. There is also a contaminant sitting on top of the sample that may be a corrosion product.

PEA0993 – TiN/TiN/TiN

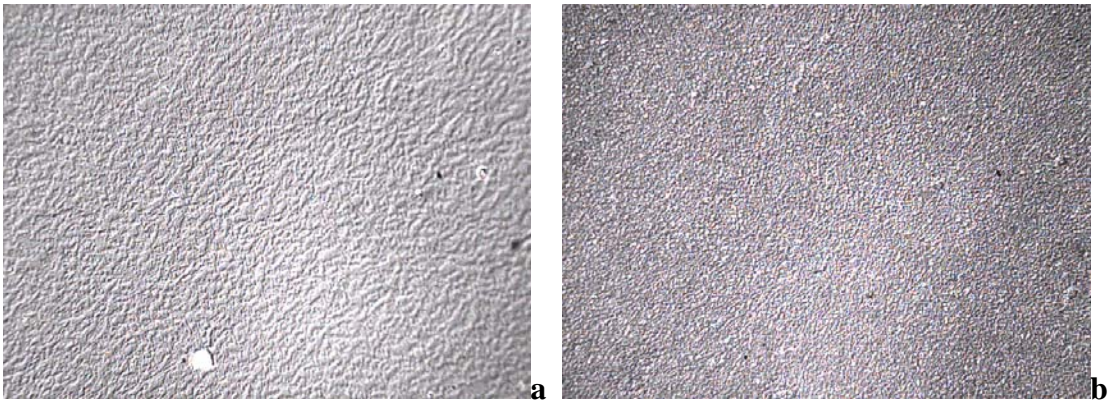


Figure 3.35 1000X optical **a)** pre-corrosion and **b)** post corrosion

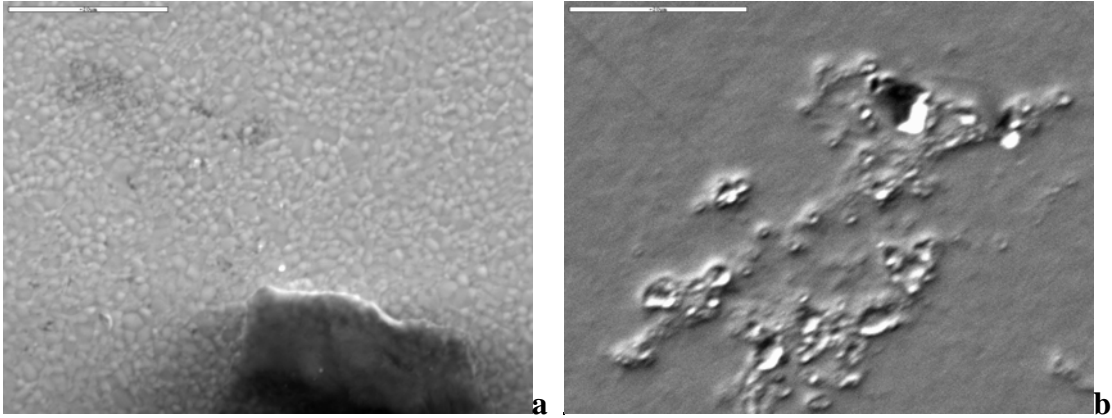


Figure 3.36 SEM image **a)** 1800X pre-corrosion and **b)** 2000X post-corrosion.

The optical images for PEA0993 (Figure 3.35) do not appear significantly different; however the post corrosion image does appear to have a slightly different surface texture. This is also seen in the SEM images (Figure 3.36), although again at different magnification. The post corrosion SEM image shows puckering and large discontinuities in the surface that are due to the corrosion testing.

PEA0994 – TiN/Ti/Ti

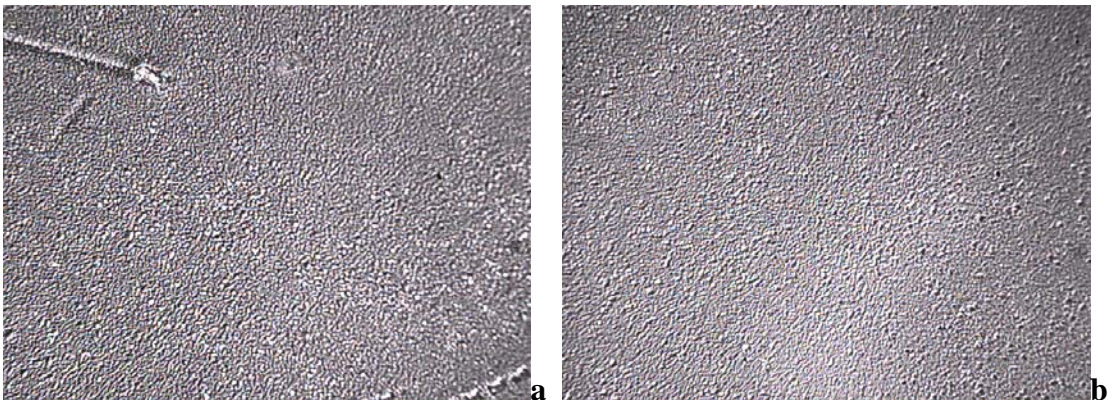


Figure 3.37 1000X optical **a)** pre-corrosion and **b)** post corrosion

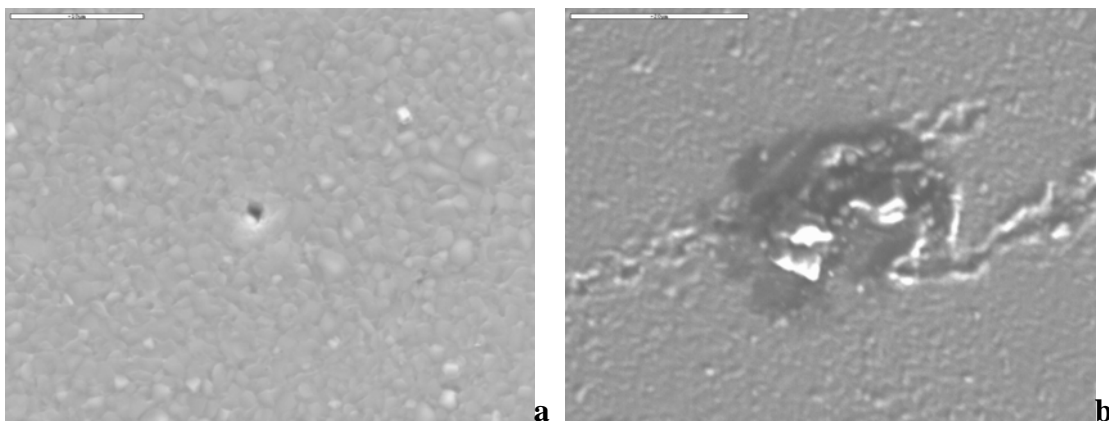


Figure 3.38 SEM image a) 3000X pre-corrosion and b) 2000X post-corrosion.

The optical (Figure 3.37) and SEM (Figure 3.38) images for PEA0994 continue to support the previous sample results. The corrosion testing did cause a change in the surface characteristics, and the pre corrosion sample is not always an ideally smooth, defect-free surface. The optical images for this sample appear to be the most similar in texture for pre- and post- corrosion, which is likely due to the higher corrosion resistance of Ti than TiN.

3.3 Discussion

The corrosion results indicate the behavior of TiN in the simulated waters for Yucca Mountain. The cyclic polarization curves provide the size of the passive region in the particular solution and give an indication of the corrosion rate of the sample. The TiN coating has a passive region of 757 ± 342 mV in SCW, 408 ± 67 mV in BSW, no passive region in 5 M CaCl_2 , and 385 ± 288 mV in SSW. The ZrO_2 does not add significant protection in SCW but there is a large passive region increase in the BSW to 1002 ± 260 mV (~500 mV increase). There is also an improvement in protection with the ZrO_2 layer in 5 M CaCl_2 , but it still does not have a passive region. The added ZrO_2 layer in SSW resulted in a large passive region increase to 1064 ± 33 mV (+600 mV; one test of ZrO_2 coating in SSW).

The 5M CaCl_2 is one of the least likely waters that might occur at Yucca Mountain and is also the most corrosive. SCW and BSW are more likely conditions at Yucca Mountain, and considered to be benign conditions. BSW, however, is currently considered to be the worst-case scenario, which means the ZrO_2 layer is good addition for corrosion protection. The added layer of ZrO_2 and the added layers of TiN and/or Ti typically reduce

the current density for every solution. This decrease in current density is proportional to a decrease in the corrosion rate of the material.

The test on nitrated titanium provides information about the behavior of the TiN as compared to the plain titanium under the highly corrosive conditions of oxalic acid. Titanium nitride corrodes more quickly than plain titanium as seen in the cyclic polarization curve through the higher current density. While this test shows that TiN does not perform as well as plain titanium under corrosive conditions, it is difficult to claim that TiN is a bad corrosion barrier because of the highly acidic solution used.

The weight-loss sample results show that the corrosion rate is highest in the aqueous region and lowest in the vapor region. The samples in the 90 °C aqueous region were stripped completely of the TiN coating. There is not a good way to verify exactly how long it took for the TiN to corrode away and for the 316L stainless steel corrosion rate to be dominating. The samples in the vapor region did not lose the TiN coating. As a rough comparison, the maximum observed corrosion rate for alloy 22 is $0.160 \mu\text{m y}^{-1}$ (Farmer et. al, 2000) and the maximum observed corrosion rate for the TiN coated stainless steel is $0.530 \mu\text{m y}^{-1}$. The TiN does not perform as well as alloy 22 in general corrosion rates as gathered from the long term corrosion test facility at LLNL.

Chapter 4

HYDROGEN DIFFUSION TESTING

Hydrogen diffusion testing was performed to verify reports that TiN is a good hydrogen diffusion barrier (Checchetto, et al, 1996; Tazhibaeva et al, 2000). The method chosen for testing this aspect of the coating was low temperature resistance measurements, which can be related to impurities in a metal sample. Impurities, such as hydrogen atoms inside a metal crystal structure, impede the free flow of electrons, scattering them and giving rise to the metal's electrical resistance. This resistivity is also dependent on the temperature, pressure and chemical and physical state of the metal (Meaden, 1965). All metals have specific resistivities in the range of 1.5 to 150 $\mu\Omega\text{-cm}$ at room temperature, and these resistivities increase roughly in proportion to the temperature and the addition of impurities.

The resistance of a material follows Ohms law ($V = I R$) where V represents voltage, I represents current in amperes, and R the resistance of a sample in ohms. The resistivity, ρ , is defined as the resistance times the cross-sectional area of the sample, A (cm^2), divided by the length of the sample, L (cm):

$$\rho = \frac{V}{I} \frac{A}{L} = R \frac{A}{L}$$

The cross-sectional area of the sample is calculated as the length times the thickness, t , therefore making the resistivity equal to:

$$\rho = R \frac{Lt}{L} = Rt$$

This resistivity (ohms-centimeters) is determined by measuring the resistance of a sample of known geometry by forcing a current through the sample with one pair of leads while measuring the voltage drop with a second pair of leads (Keithley, 1998).

For discussions on resistivity, a distinction is often made between a temperature-dependent component and a temperature-independent component. There are natural vibrations in a material lattice that cause electron scattering and are dependent on temperature as well as scattering caused by impurity atoms which are nearly independent of

temperature. These two components are described in Matthiessen's rule as being additive to represent the total resistivity, ρ_{tot} , of a material:

$$\rho_{tot}(T) = \rho_0 + \rho_h(T)$$

where ρ_0 is the temperature independent resistivity and $\rho_h(T)$ is the resistivity of the pure host material at that temperature (Rossiter, 1987). The material lattice will always be present in resistance measurements and affects the slope on a plot of resistance versus temperature for a material. Impurity atoms present in a material will not alter the slope on a resistance versus temperature plot, but will increase the magnitude of the resistance if a large amount of impurities are present. This relation can be seen in Figure 4.1.

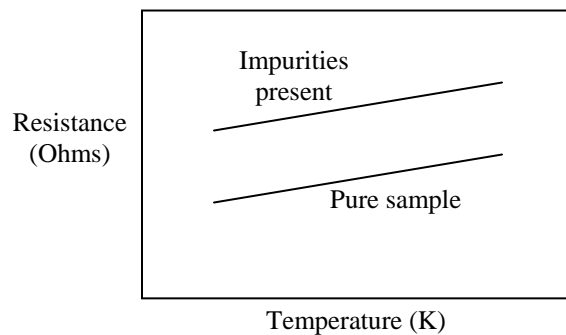


Figure 4.1 General resistance vs. temperature trend observed between a pure metal and a metal with impurities.

The literature (Rossiter, 1987; Meaden, 1965) notes quite often that Matthiessen's rule is true in most systems. Sometimes the impurity resistance can be treated as temperature dependent, but there is not usually a significant change as compared to a large temperature change. The principle can usually be applied for most metals, and is used in this thesis, along with material analysis through Secondary Ion Mass Spectroscopy (SIMS). These resistance measurements were used in conjunction with the characteristics of stainless steel to absorb hydrogen when elevated in temperature.

4.1 Apparatus, Materials, and Methods

Samples tested were small 304 stainless steel disks with a diameter of 5 mm, 1 mm thick. These samples were prepared at NCSU by using a small punch device on a sheet of 1

mm-thick, 304 stainless steel. They were polished and cleaned, and half of the samples were coated as described in Chapter 2.

After coating all sides of the 1 mm-thick samples, three coated samples and three uncoated samples were exposed to hydrogen by placing them inside a sealed chamber, raising the temperature to 300°C, and setting the hydrogen pressure to 30 Torr. This condition was held for three hours before the samples were cooled, the chamber purged, and the samples removed for resistivity measurements. The resistivity measurements were done by passing current through the sample and measuring the resulting voltage.

Passing current through the sample was done using gold wire leads connected to the sample with silver paste. Additional gold wire leads were connected to measure the voltage across the sample and calculate the sample resistance. The leads were connected in a single line configuration across the diameter of the sample, as depicted in Figure 4.2. This configuration is defined as a four-point collinear probe configuration by

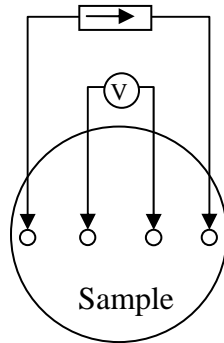


Figure 4.2 Diagram showing lead location and use on 5 mm-diameter sample for resistivity measurements.

Keithley Instruments (1998), and used for very thin samples. The current was sourced through the two outer probes, while the voltage drop was measured between the two inner probes.

The equipment used to apply the current and measure the voltage included a nanovoltmeter (Keithley model 2182) and current source (Keithley model 2400). The sample was placed in a specialized dewar for small samples designed by MMR Technologies. This low temperature hall dewar as shown in Figure 4.3 was fitted with BNC connectors for resistivity measurements. It contained a miniature Joule-Thomson refrigerator

for operating temperatures between 80 and 400 K. A Joule-Thomson refrigerator works by passing a high pressure, non-ideal gas through a heat exchanger where it expands from high to low pressure at constant enthalpy (MMR Technology). This process is basically an adiabatic expansion of a gas and has been developed by

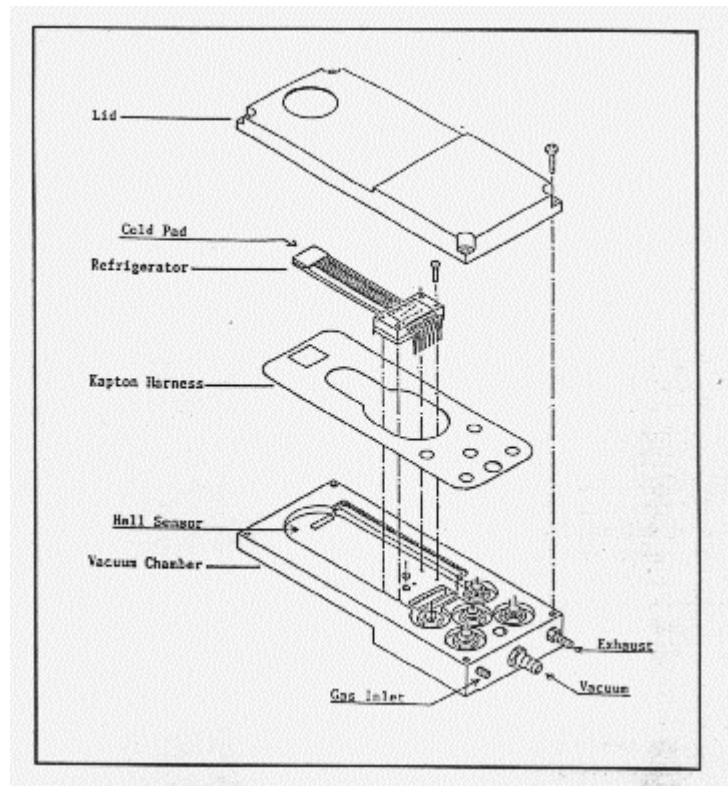


Figure 4.3 Low temperature hall dewar diagram, 6.0" x 2.5" x 0.75" (MMR Technologies, 2005).

MMR Technology for many applications including low temperature resistance measurements.

The Joule-Thomson refrigerator was connected to a cold pad where the sample was 'glued' using a conducting zinc-oxide paste. The gold wire leads (connected to the sample) were soldered to a circuit board inside the dewar that was attached to standard BNC connectors for completing the circuit with the current source and nanovoltmeter. A heat sensor for measuring the temperature was located under the cold pad. Temperature control and measurements were done using the K20 temperature controller and software developed

by MMR Technologies. The dewar was made of aluminum metal and contained all these elements inside a vacuum seal for evacuating down to a pressure of 1-2 mTorr pressure.

The tests done on the samples for this thesis were done using the connections described above at a temperature range of 200 K to 350 K. As the temperature was controlled on the sample, a current of 30 mA was passed through the sample and a measurement of the voltage was taken at every 5 K temperature increment. The resistance was calculated using Ohm's law, and the results were plotted as the resistance versus the temperature.

Further characterization on two (one H₂ exposed, one not H₂ exposed) of the TiN coated samples and two non-coated samples was done using secondary ion mass spectrometry (SIMS). This analysis was done to provide more clarification to the question of whether the TiN prevents hydrogen from diffusing through into the stainless steel substrate. The SIMS analysis provided a depth profile of the elements present in each sample.

4.2 Hydrogen Testing Results

The results that were gathered using the low temperature resistance measurements can be seen in Figures 4.4 – 4.6. This data indicates that all the samples are of the same composition because they have the same slope. It is difficult to reach a conclusion using this data however, because the plots of resistance versus temperature of the hydrogen exposed and non-exposed samples have approximately the same magnitude. There is only one hydrogen exposed sample (see Figure 4.4) with an increase in magnitude as would be expected due to the impurities present in the sample. It is unclear why there are not additional samples of plain stainless steel exposed to hydrogen with an increased magnitude. It is interesting to note however, that all of the TiN coated samples are of the same magnitude with no large magnitude increase observed in the hydrogen exposed samples.

Due to the nature of these resistivity measurements, it is also possible that oxides on the surface of the samples could have altered the voltage measurements taken.

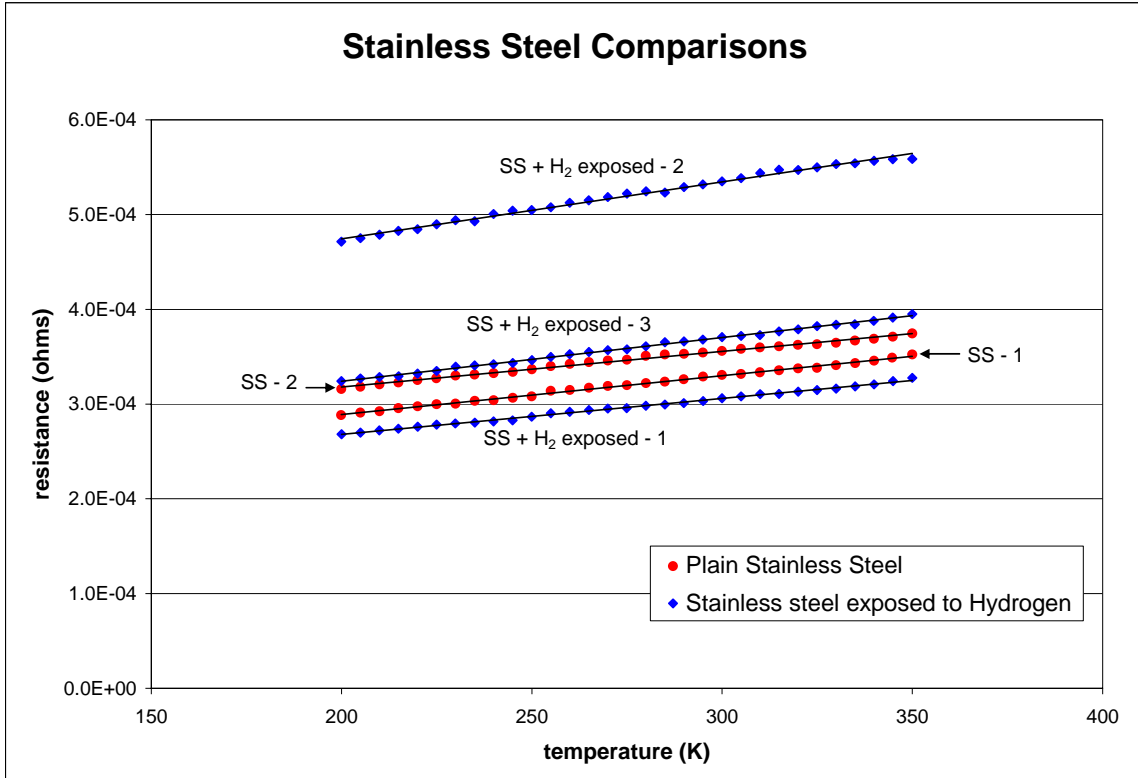


Figure 4.4 Stainless steel resistance vs. temperature data for plain and hydrogen-exposed.

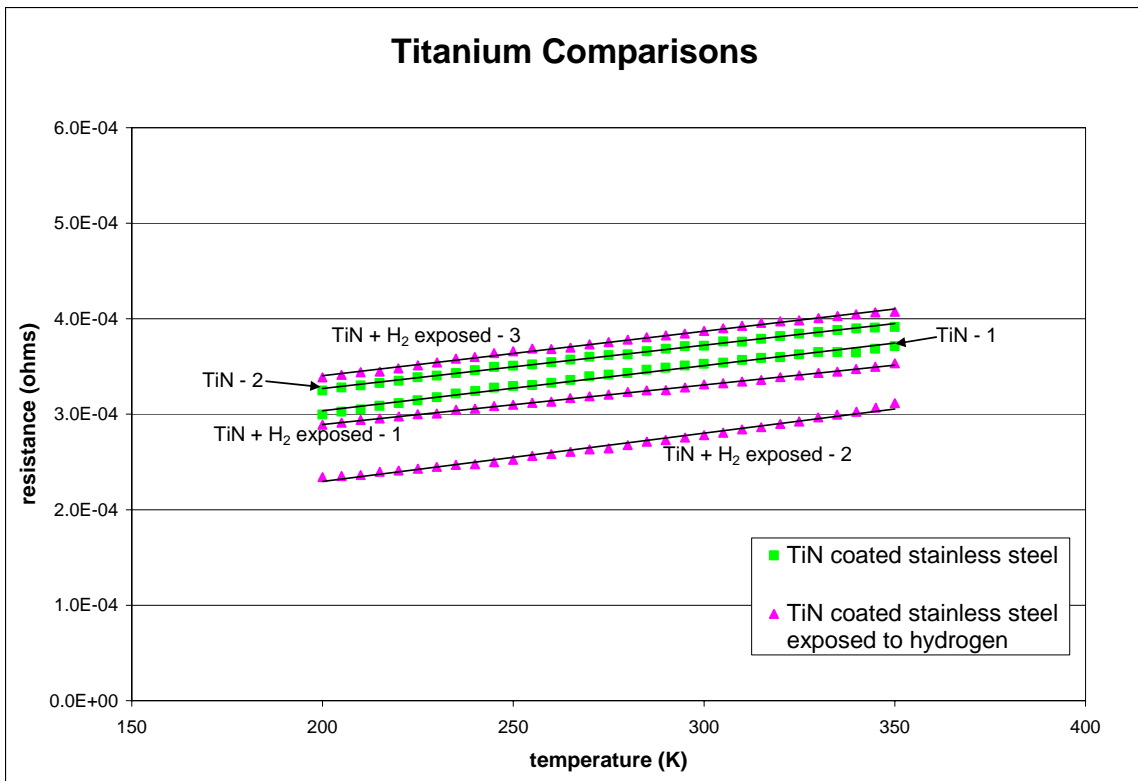


Figure 4.5 TiN coated resistance vs. temperature data for plain and hydrogen exposed samples.

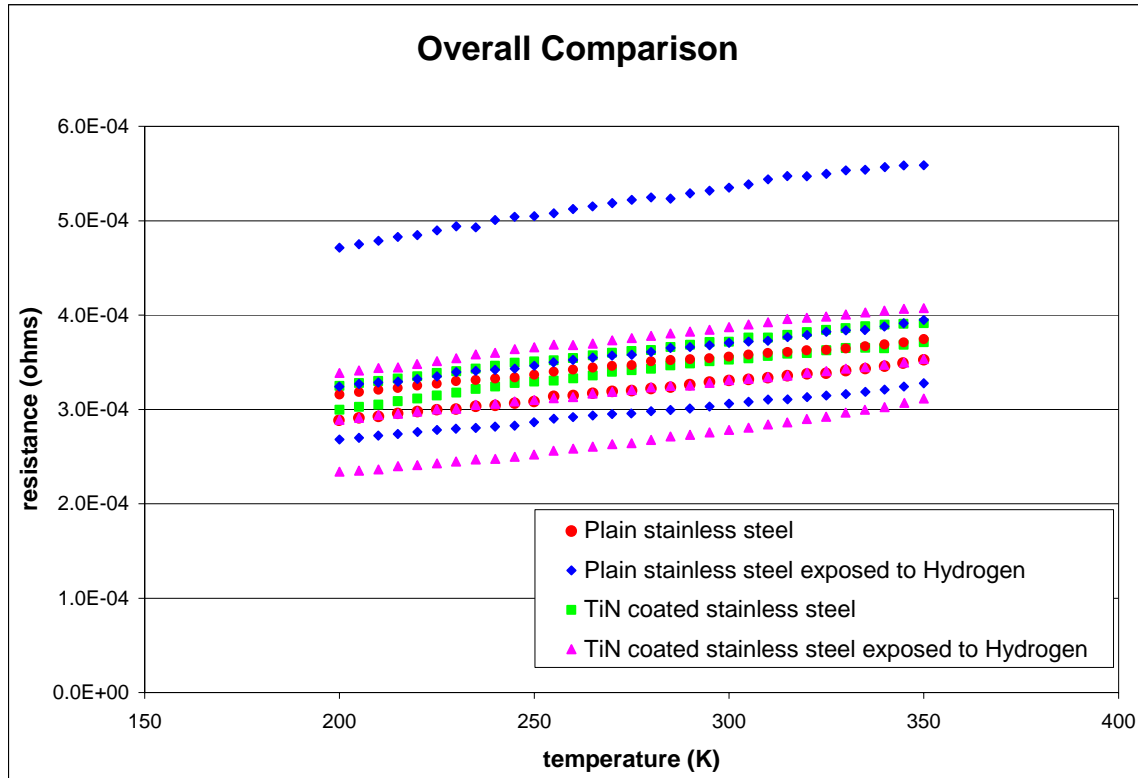


Figure 4.6 Plain stainless steel and TiN coated resistance versus temperature data combined for overall comparison.

The characterization performed using SIMS to test how much, if any, hydrogen diffused into TiN-coated stainless steel samples provided some additional answers to the resistivity measurements. Elemental depth profiles from the SIMS results can be seen in Figures 4.7 thru 4.9. Figures 4.7 and 4.8 show the profile for nickel, TiN (Figure 4.7), hydrogen, and oxygen (Figure 4.8) for TiN coated stainless steel samples. It is clear where the transition between the coating and the stainless steel sample is from the shift in TiN and Nickel in Figure 4.7. This is a good indication for the thickness of the TiN coating, approximately 0.9 μm . Hydrogen is the key element to look at in Figure 4.8, and it is revealed that the hydrogen content in the exposed sample is actually lower than the hydrogen content in the non-exposed sample. This indicates that the TiN does act as a good hydrogen diffusion barrier. The depth profile for oxygen shows that there is more oxygen in the exposed sample rather than the non-exposed sample. This large oxygen increase is likely due to the hydrogen exposure when the temperature was raised and held for a period of three hours. Any moisture and oxygen in the hydrogen chamber at this point would have been

attracted to the TiN film to form an oxide on the film. Oxides can also increase the resistance levels as measured in the resistivity tests performed earlier. This is consistent with the resistivity measurements made on the TiN coated samples (Figure 4.5) where the higher magnitude hydrogen exposed sample is the same sample measured by SIMS.

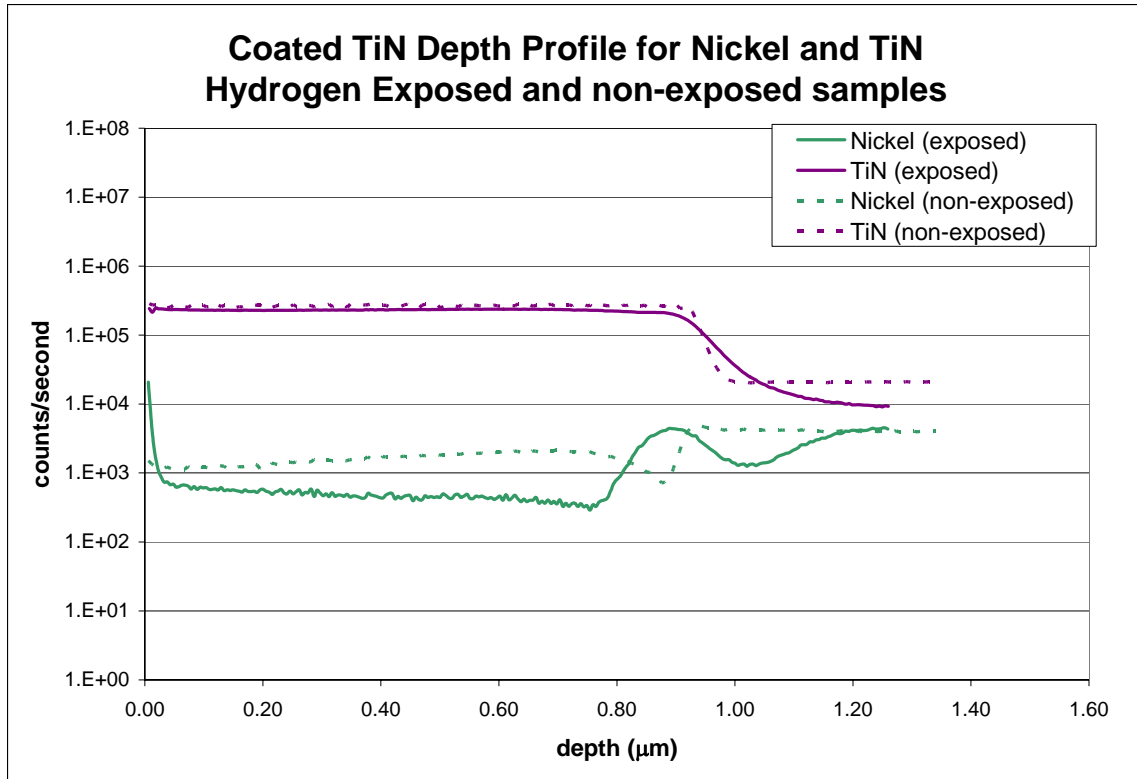


Figure 4.7 Nickel and TiN SIMS depth profile for hydrogen exposed and non-exposed TiN-coated samples.

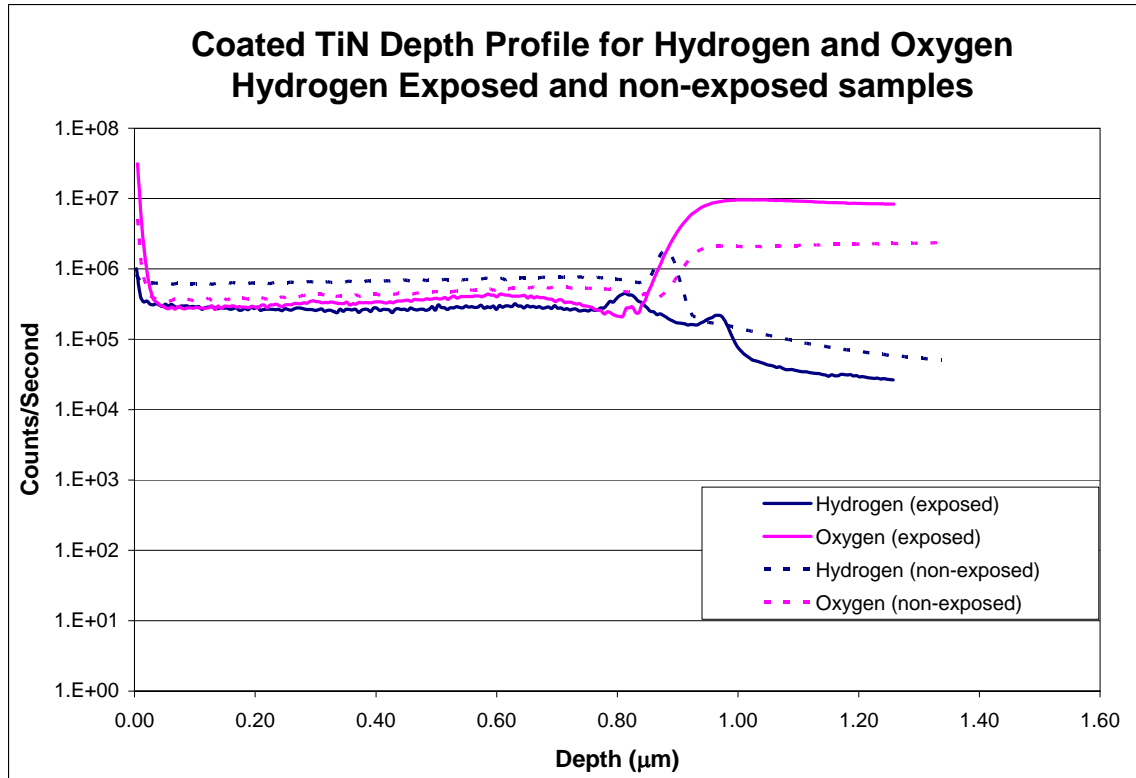


Figure 4.8 Hydrogen and oxygen SIMS depth profile for hydrogen exposed and non-exposed TiN-coated samples.

A second SIMS analysis was performed on two plain stainless steel samples to test what the base hydrogen amount in the sample was, and to see if the exposed stainless steel sample had more hydrogen present than the non-exposed sample. This SIMS result can be seen in Figure 4.9. In this depth profile, the hydrogen content is much lower than in the TiN coated samples and it is about the same for both samples. This does not support the prediction that there would be more hydrogen in the hydrogen-exposed sample. Based on this, in conjunction with the low temperature resistance measurements, there needs to be more tests performed to absolutely verify the hydrogen barrier property claim.

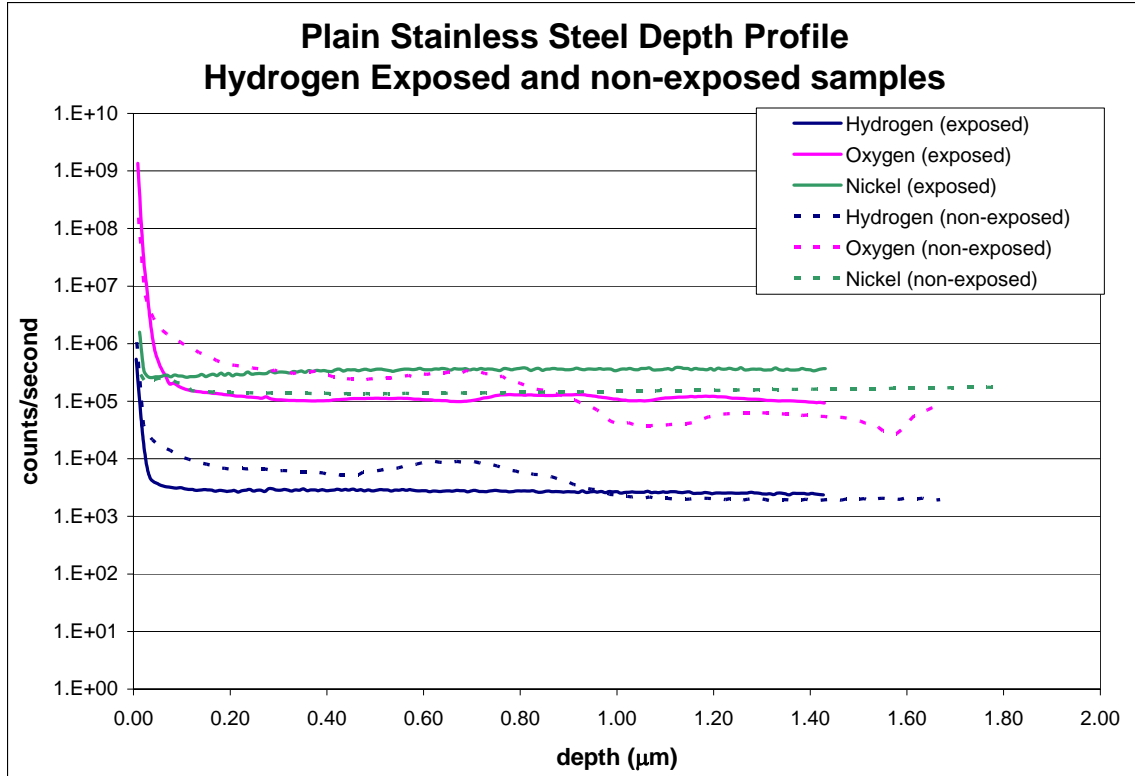


Figure 4.9 Hydrogen, oxygen, and nickel SIMS depth profile for hydrogen exposed and non-exposed plain stainless steel samples.

4.3 Discussion

If hydrogen was able to diffuse through the TiN coating and enter the stainless steel substrate, there should have been a higher concentration (count-rate or resistance magnitude) of hydrogen in the exposed sample as compared to the non-exposed sample. As seen in the SIMS analysis, there was not more hydrogen in the exposed TiN coated sample than the non-exposed sample. However, there was also no difference between the exposed and non-exposed plain stainless steel samples. Figure 4.9 could be the result of several different cases including: no hydrogen diffused into the stainless steel sample that was exposed, hydrogen diffused out of the exposed sample between the time of exposure and SIMS testing, or hydrogen diffused out of the sample while inside the SIMS chamber that was taken to a vacuum of about 10^{-10} Torr. Each of these can be considered with respect to the diffusion coefficient of hydrogen in stainless steel.

Hydrogen readily diffuses into and out of stainless steel ($D=1.0E-6 \text{ cm}^2 \text{ s}^{-1}$ at room T), especially at elevated temperatures (Fukai, 1993; Grant et. al., 1987). During the

exposure period the temperature was elevated to 250-300 °C and held for a period of 3 hours while under positive hydrogen pressure. Based on the diffusion coefficient of hydrogen in stainless steel, there is no reason to believe that hydrogen did not diffuse into the uncoated stainless steel sample. As for the second possibility, the samples were stored inside simple storage boxes at room temperature. Hydrogen in the sample will remain at equilibrium inside the sample unless the temperature is increased or there is a large pressure difference between the hydrogen in the atmosphere and the hydrogen in the sample.

The third possibility could be a better explanation for why there is no obvious increased level of hydrogen in the exposed sample. SIMS needs to be performed under a very large vacuum and the samples were placed in the SIMS chamber for two and half days to allow for a good vacuum to be reached. A vacuum of 10^{-10} Torr is quite substantial and is a perfect example of a concentration gradient, a good environment for hydrogen to diffuse out of the 1 mm-thick sample ($1.0E-6 \text{ cm}^2 \text{ s}^{-1} * 2.5 \text{ days} * 24 * 3600 = 0.216 \text{ cm}^2 \implies 0.464 \text{ cm}$ root-mean square distance of diffusion). The level of hydrogen in the TiN coated samples indicates that hydrogen is present, and at a higher level than seen in the plain stainless steel samples. The coating, as a hydrogen barrier, could have prevented any hydrogen in the stainless steel from diffusing into or out of the sample, even under the vacuum condition of the spectrometer. The hydrogen detected in these coated samples could have also been a result from the coating process, but with the hydrogen being detected at different levels there is a conflict because each sample was coated at the same time and should have had the same amount of hydrogen.

The tests and results gathered using low temperature resistance measurements and SIMS analysis tend to support the claims that TiN is a good hydrogen diffusion barrier. The SIMS is more convincing through the hydrogen depth profile of exposed and non-exposed TiN coated samples that the coating is a good barrier. More tests need to be completed to absolutely verify the TiN coating barrier property, but as for right now references that support the barrier property of TiN will be used (Tazhibaeva, 2000).

Chapter 5

DISCUSSION

5.1 Significance of Results

The results collected throughout this thesis work have provided valuable information about the properties of TiN coatings and its effectiveness in corrosion environments. In addition, TiN is possibly a good barrier to hydrogen diffusion, and can provide better corrosion protection than plain stainless steel in the Yucca Mountain solutions tested. The TiN coating is not as protective against corrosion as an additional layer of ZrO₂ or multiple layers of TiN coating on a substrate. This simple observation and all the supporting cyclic polarization curves along with the weight-loss corrosion rate samples indicate that TiN can withstand Yucca Mountain corrosion conditions of SCW and BSW. While this is true, it is only true to the level indicated by the cyclic polarization and weight-loss corrosion results. There is a passive film that forms and breaks down at higher corrosion potentials. If the corrosion properties of Alloy 22 and titanium grade-7 are desired and absolutely required, more needs to be done to provide additional corrosion protection.

The uncertainty involved with the prediction of actual Yucca Mountain conditions thousands of years in the future creates difficulty in determining exactly what amount of protection is necessary. The barrier property of TiN to hydrogen is a possible improvement to designs that do not seriously consider hydrogen embrittlement. A TiN coating does not however increase or even meet the current corrosion protection provided by Alloy 22 and titanium grade-7. In addition, a thin film coating of TiN will not provide structural protection to the waste package as the titanium drip shield provides in the Yucca Mountain design. This structural shortfall could be negligible if a backfill in Yucca Mountain is used, which can improve the structural protection against falling rocks inside the drift.

The application and adhesion of the coatings is directly proportional to the surface preparation and cleanliness of the substrate to be coated. In simple terms, proper adhesion requires a pristine substrate surface. While surfaces were prepared carefully for these coatings, there were still defects in the coating that could not be completely eliminated. This

indicates that there is difficulty in preparing a perfect TiN coating, but this was counteracted by applying multiple coatings of TiN on the substrate surface. Magnetron sputtering is also a more efficient method than laser ablation for applying TiN.

5.2 Engineering and Economic Considerations

The application of this TiN coating to the large scale of Yucca Mountain would be a major project requiring time and money to implement. The experiments done here were completed in a lab on a small scale, and the important factors that will need to be scaled up for Yucca Mountain include the vacuum chamber, elevated temperature, surface preparation, and sputtering targets for such a large surface (waste package). Assuming this coating were to be applied directly to the surface of the waste package, there would need to be a large vacuum chamber that could create a vacuum on the scale of 10^{-5} Torr in a reasonable amount of time. Inside this vacuum chamber there should be multiple sputtering devices to allow for coating of the entire surface at once. In order to produce a good coating that adheres well to the waste package, it would need to be a smooth, clean surface and its temperature would need to be increased. This depiction only addresses a few of the major parts of the process that need to be considered. While it is a large task, it is not impossible because there are large scale applications of this same nature that are in use now by various industries including NASA. Coating technology for large scale applications is also available for use in a system such as this.

The application of coatings on this scale will be costly, but it is not certain what the exact difference between the coating and the titanium drip shield would be. Costs of titanium are about 30 times more expensive per pound than steel and about 6 times more expensive than aluminum (Hurless, 2002). Using titanium for the drip shield in Yucca Mountain will also put a strain on the market for available titanium, an already valuable material for many engineering applications. A TiN coating would not require as much titanium material forming (major cost for titanium), but would require the additional application costs associated with the above description. The costs, along with the advantages and disadvantages of the titanium drip shield to the TiN coating should be considered further to determine what a more useful design is. If the cost of applying the TiN coating on waste packages is much less than that of using high grade titanium, the hydrogen barrier

characteristics of the TiN coating could make it a good choice for an alternative to the drip shield.

Other options should also be considered if there is any way to reduce costs and improve the long term performance of Yucca Mountain. This multi-layer coating along with a backfill is one possible alternative. Other materials could also be used rather than titanium as a drip shield for structural protection. An early design for the Yucca Mountain waste package called for an outer shell of 4 inch thick carbon steel that could provide structural strength and corrosion protection through a different mechanism than the inner shell of alloy 22. While this design was rejected, its general idea using a thick barrier of carbon steel may be another option that could be less expensive and just as effective. The significance of these results however should be compared carefully to the standards required for the protection of the environment from radionuclides being placed in Yucca Mountain. Right now there is not enough evidence to claim that this multi-layer coating would protect as well as the titanium drip shield is predicted to perform.

5.3 Other Applications

The corrosive properties of TiN have been studied for other solutions (Li, 2004) and have been shown to have a high corrosion resistance. Corrosion resistance to simulated Yucca Mountain waters has been shown in these experiments but the level of resistance may not be sufficient for applications in Yucca Mountain. As described by Li et. al., TiN can be used on bipolar plates for fuel cells. The hydrogen diffusion barrier property of TiN adds to its desirability for an application such as fuel cells. The diffusion barrier property of TiN has also been specifically mentioned to be a possible material for fusion reactor technology (Checchetto, 1996). There are many applications for TiN as seen through its common use today as a PVD coating for tools, sporting goods, and even jewelry. A multi-layer coating with the added corrosion protection from ZrO_2 increases the possibility for even more applications of this coating.

Chapter 6

CONCLUSIONS AND FUTURE WORK

6.1 Conclusion

TiN and TiN + ZrO₂ coatings were successfully produced using magnetron sputtering and laser ablation. These coatings were tested for their corrosion resistance using polarization and weight-loss tests, and it was shown that the second layer of ZrO₂ is an added benefit for protecting against corrosion in BSW and SSW. It was also found that multiple layers of TiN decreased the corrosion rate in simulated Yucca Mountain water SCW. The overall corrosion resistance of TiN and TiN + ZrO₂ is higher than that of plain stainless steel in the simulated waters, but not as high as alloy 22 or plain titanium, the materials of choice for Yucca Mountain. A three layer coating of TiN + ZrO₂ + DLC was also successfully produced but not tested for corrosion resistance.

The TiN coating deposited using magnetron sputtering was tested to see how it might act as a diffusion barrier against hydrogen. Low temperature resistance measurements did not provide conclusive results about the barrier properties of TiN, but further SIMS analysis on the samples showed that TiN did act as a barrier to hydrogen. The SIMS analysis revealed no increase of hydrogen in the exposed sample as compared to the non-exposed sample. SIMS does not however, indicate that the plain stainless steel sample exposed to hydrogen has a higher concentration of hydrogen as compared to the plain stainless steel sample with no hydrogen exposure. The hydrogen in the exposed stainless steel sample may have diffused out while in the SIMS vacuum for an elongated time and more needs to be done experimentally to investigate the barrier property of TiN.

The hydrogen barrier property of TiN is not sufficient to claim that the multi-layer coating will be an effective alternative for the Yucca Mountain drip shield. This multi-layer coating does not have the high level of corrosion resistance that the drip shield material, titanium, provides. The coatings will not provide any structural support, another key feature of the drip shield design for Yucca Mountain. However, TiN does appear to prevent hydrogen from diffusing through into an underlying substrate. This barrier to hydrogen can

add to the performance of the waste package design for Yucca Mountain by preventing hydrogen embrittlement of the waste package material. While its corrosion protection is not as extensive as the titanium, the coating does have protective properties against corrosion and the addition of a backfill may help to enhance the protection of the coating.

6.2 Future Work

There are several things that can be done to support this research and further investigate the possibility of an alternative for the Yucca Mountain drip shield. Regarding this research specifically, the optimal coating thicknesses and coating properties should be analyzed. The thickness of the coating may be related to how well it adheres to the substrate, how it performs under corrosive conditions, or how well it acts as a diffusion barrier to hydrogen. Definitely more experimental work into the diffusivity of hydrogen through TiN needs to be done for a more quantitative solution to how effective TiN acts as a hydrogen barrier. A more thorough microscopic analysis of the coating layers should be undertaken to determine if there is something other than substrate preparation causing surface defects. There are also further corrosion tests and analysis that can be done, particularly regarding the EIS analysis. The information gathered from EIS can be useful and a more in depth analyses is needed to fully utilize the information.

Research into how well a backfill material may or may not support the use of a coating material as an alternative to a titanium drip shield can also be performed. A feasibility study for the upscale of a process such as coating waste packages for Yucca Mountain may also be a useful tool in determining the actual possibility of a multi-layer coating barrier.

Chapter 7

REFERENCES

- ASTM Designation G 3 - 89. "Standard practice for conventions applicable to electrochemical measurements in corrosion testing." Reapproved 2004.
- ASTM Designation G 5 - 94. "Standard reference test method for making potentiostatic and potentiodynamic anodic polarization measurements." Reapproved 2004.
- ASTM Designation G 61 - 86. "Standard test method for conducting cyclic potentiodynamic polarization measurements for localized corrosion susceptibility of iron-, nickel-, or cobalt-based alloys." Reapproved 2003.
- ASTM Designation G 106 - 89. "Standard practice for verification of algorithm and equipment for electrochemical impedance measurements." Reapproved 2004.
- Bard, A.J. and L.R. Faulkner. Electrochemical Methods: Fundamentals and Applications. New York: John Wiley and Sons, 1980.
- Benton, H., Connel, J. "The evolution of spent-fuel waste packages: designing the means to permanently dispose of U.S. high-level nuclear waste." Radwaste Solutions. March/April 2001: 34-42.
- Burkholder, H.C. and E.L.J. Rosinger. "A model for the transport of radionuclide and their decay products through geologic media." Nuclear Technology. 49 (June, 1980): 150-158.
- Checchetto, R. et al. "Analysis of the hydrogen permeation properties of TiN-TiC bilayers deposited on martensitic stainless steel." Surface and Coatings Technology 83 (1996): 40-44.
- David R. Lide, Ed. CRC Handbook of Chemistry and Physics. 85th Ed. CRC Press: 2004-2005.
- Dean, S.W. "Electrochemical methods of corrosion testing." Electrochemical Techniques for Corrosion Engineering. Ed. R. Baboian. Houston, TX: NACE, 1986.
- Eckhardt, Roger C. "Yucca Mountain: looking 10-thousand years into the future." LANL Science 26 (2000): 464-471.

- Farmer, et al. "Technical basis document no. 6: Waste package and drip shield corrosion."
LLNL: August 1, 2003. UCRL-LR-155288.
- Froes, F.H. "How to market titanium: lower the cost." JOM, 56.2 (February 2004): 39
- Fukai, Yuh. The Metal Hydrogen System: Basic Bulk Properties. New York: Springer-Verlag, 1993.
- Gdowski, G.E., T.J. Wolery, N.D. Rosenberg. "Waste package environment for the Yucca Mountain site characterization project." Mat. Res. Soc. Symp. Proc. Vol 713. Ed. B. Peter McGrail. Warrendale, PA: Materials Research Society, 2001. 29-36.
- Grant, D.M., Cummings, D.L., Blackburn, D.A., "Hydrogen in 304 steel; diffusion, permeation, and surface reaction." Journal of Nuclear Materials. 149 (1987): 180-91.
- Hurless, Brian and F.H. Froes. "Lowering the Cost of Titanium." Amptiac Quarterly. 6.2 (Summer 2002): 3-23.
- Jones, Denny.A. Principles and Prevention of Corrosion. New York: Macmillan Publishing Company, 1992.
- Keithley, ed. Low level measurements: Precision DC Current, Voltage, and Resistance Measurement. 5th ed. Cleveland, OH: Keithley Instruments, 1998.
- Li Moucheng, et al. "Corrosion behavior of TiN coated type 316 stainless steel in simulated PEMFC environments." Corrosion Science. 46 (2004): 1369-1380.
- Nevada Commission on Nuclear Projects Report to the Governor and Legislature. "Site suitability – the technical argument." December, 2000. February 9, 2005 <<http://www.state.nv.us/nucwaste/news2001/commrpt2000tech.pdf>>
- Office of Civilian Radioactive Waste Management <<http://www.ocrwm.doe.gov>>
- OCRWM. "Engineered barrier system degradation, flow, and transport process model report." TDR-EBS-MD-000006 REV 00ICN01. July 2000.
- OCRWM. "Final report: Waste package materials performance peer review panel, Feb. 28, 2002." January 2004 – March 2005 <http://www.ocrwm.doe.gov/documents/peer_rev/main.htm>
- Liu, C et al. "An electrochemical impedance spectroscopy study of the corrosion behaviour of PVD coated steels in 0.5 N NaCl aqueous solution: Part I. Establishment of equivalent circuit for EIS data modeling." Corrosion Science 45 (2003): 1243-1256.
- Meaden, George T. Electrical Resistance of Metals. New York: Plenum Press, 1965.

- Miller, John C. and Richard F. Haglund, eds. Laser Ablation and Desorption, vol 30: Experimental methods in the physical sciences. San Diego: Academic Press, 1998.
- MMR Technologies, Inc. 2003. January 25, 2005 <<http://www.mmr.com>>
- Murray, Raymond L. Understanding Radioactive Waste. 5th Ed. Columbus, OH: Battelle Press, 2003.
- Rosenberg, N.D., G.E. Gdowski, K.G. Knauss. “Evaporative chemical evolution of natural waters at Yucca Mountain, Nevada.” Applied Geochemistry 16 (2001): 1231-1240
- Rossiter, Paul L. The electrical resistivity of metals and alloys. New York: Cambridge University Press, 1987.
- Saling, James H., and Audeen W. Fentiman. Radioactive Waste Management. 2nd Ed. New York: Taylor and Francis Publishing, 2002.
- Tazhibaeva, I.L. et al. “Hydrogen permeation through steels and alloys with different protective coatings.” Fusion Engineering and Design. 51-52 (2000):199-205.
- Tompkins, Betsy Ed. “Report calls for option other than Yucca Mountain.” Nuclear News. January, 2005: 56+.
- United States. Nuclear Regulatory Commission. 10 CFR Parts 2, 19, 20, 21, etc.: Disposal of high-level radioactive wastes in a proposed geologic repository at Yucca Mountain, Nevada; final rule. Federal Register, vol. 66, no.213: November 2, 2001.
- United States. Nuclear Waste Technical Review Board. ‘December 30, 2004 Letter to Congress and the Secretary of Energy.’ January 14, 2005 <<http://www.nwtrb.gov/reports/con219.pdf>>
- Voevodin, A.A. et al. “Mechanical and tribological properties of diamond-like carbon coatings prepared by pulsed laser deposition.” Surface and Coatings Technology. 76-77 (1995): 534-539.
- Wert, C. A. “Damping of interstitial atoms in bcc metals.” Journal of Physics and Chemistry of Solids. 31.8 (1970): 1771-1783.
- Wilson, Michael et al. “Total-system performance assessment for the yucca mountain site.” Mat. Res. Soc. Symp. Proc. Vol 713. Ed. B. Peter McGrail. Warrendale, PA: Materials Research Society, 2001. 152-164.
- Yim, M.S., K.L. Murty. “Materials Issues in Nuclear Waste.” JOM. September 2000: 26-29.
- Zacha, Nancy J. “Waste Management 2002: Step-by-step, top-to-bottom, Rebecca, and other topics.” American Nuclear Society: Radwaste Solutions. May/June 2002. 52-57.

Appendix A – Material Properties

The following properties for TiN and ZrO₂ are listed as reported in the CRC Handbook of Chemistry and Physics (CRC, 2004-2005).

Table A.1 Properties of TiN and ZrO₂

	Unit	Titanium Nitride	Zirconium Oxide
Formula	--	TiN	ZrO ₂
Molecular Weight	--	61.874	123.223
Physical Form	--	Yellow-brown, cubic crystalline	White amorphous powder
Melting Point	°C	2950	2709
Density	g/cm ³	5.21	5.68
Qualitative Solubility	--	Insoluble in water, soluble in HNO ₃	Insoluble in water, slightly soluble in acid
Hardness	Mohs (1-10)	9	--
	Mod. Mohs (1-15)	--	11
	Knoop	1770	--

Appendix B – Cyclic Polarization Curves

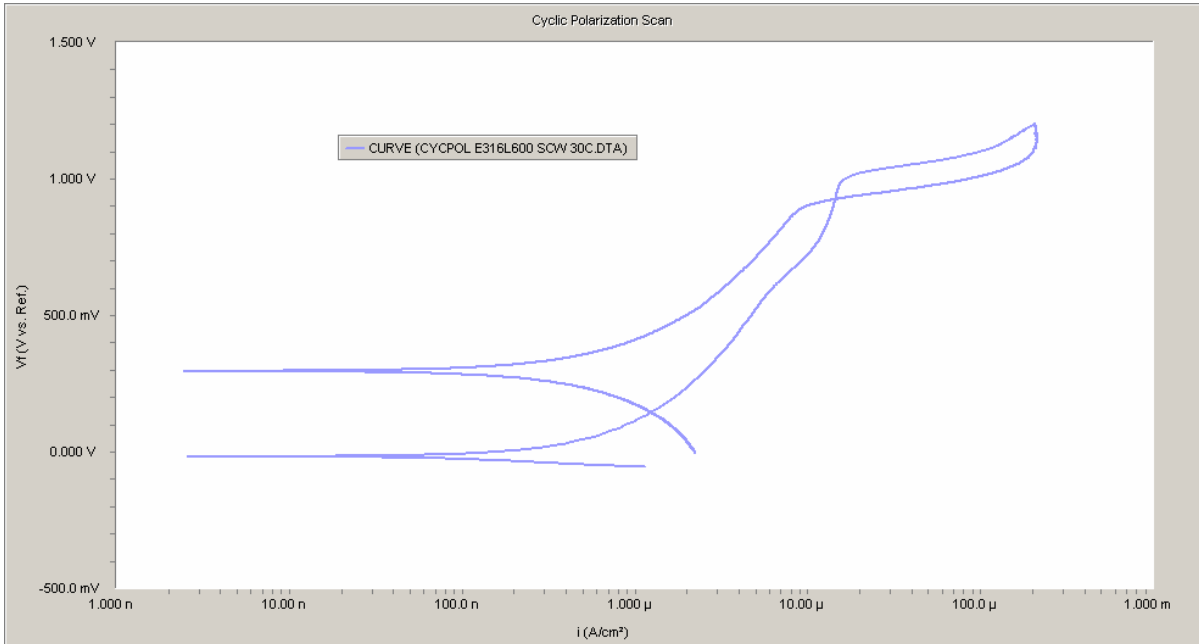


Figure B.1 Cyclic polarization curve – TiN coated E316L600, 30 °C SCW

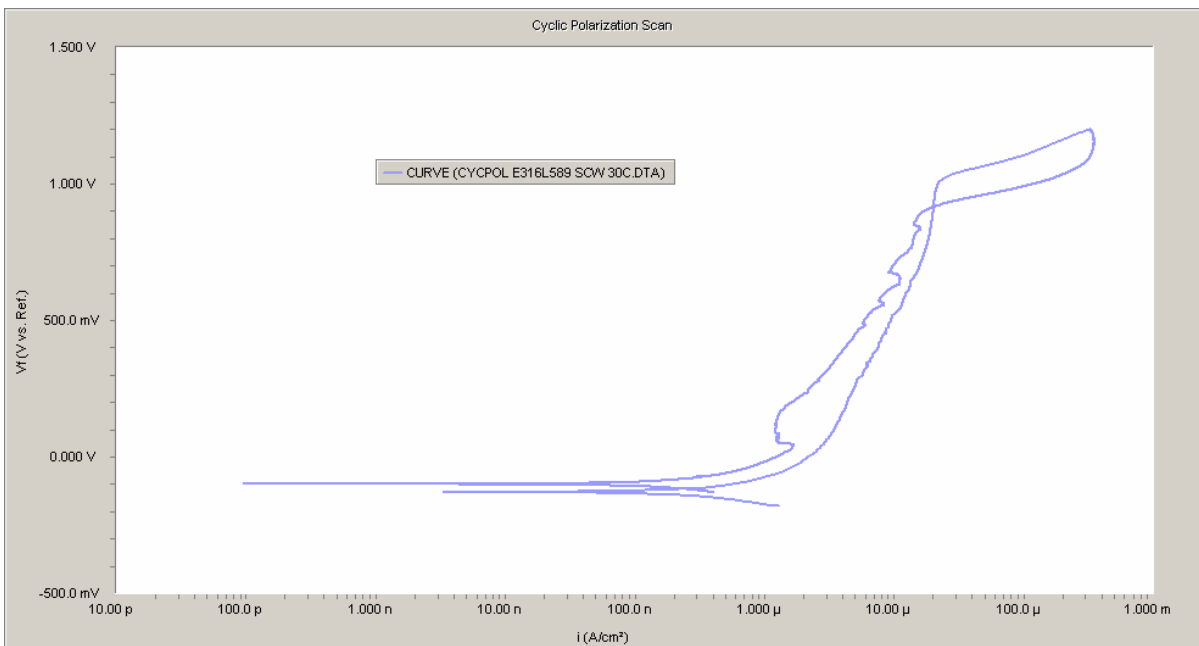


Figure B.2 Cyclic polarization curve – TiN coated E316L589, 30 °C SCW

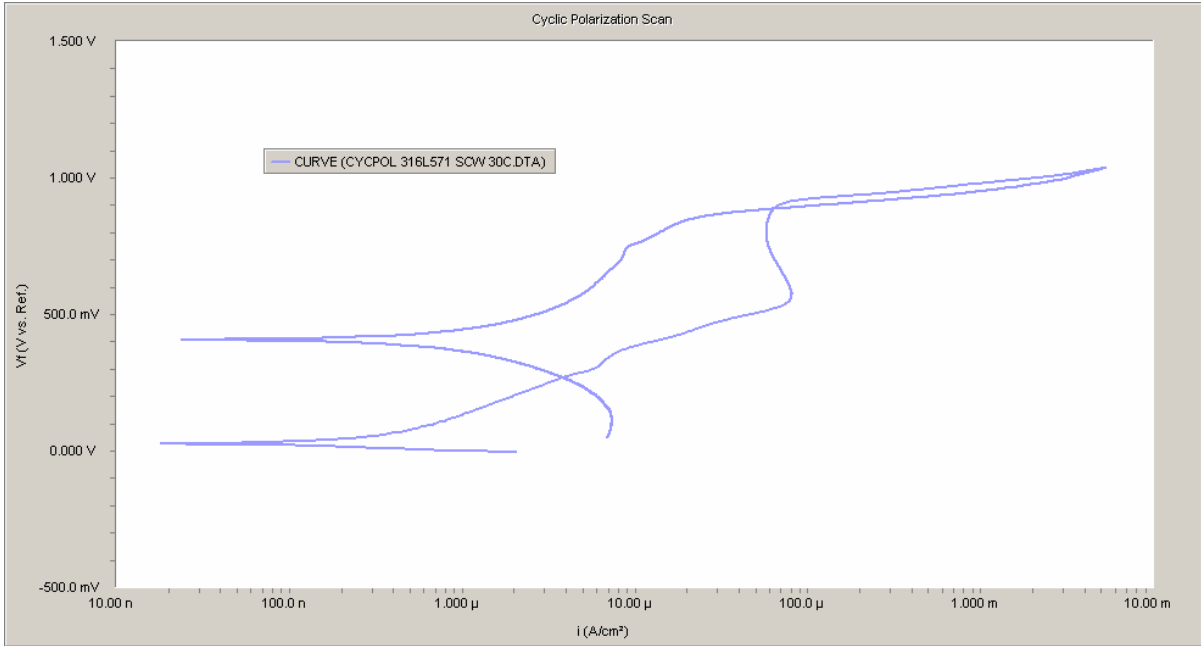


Figure B.3 Cyclic polarization curve – plain 316L stainless steel E316L571, 30 °C SCW

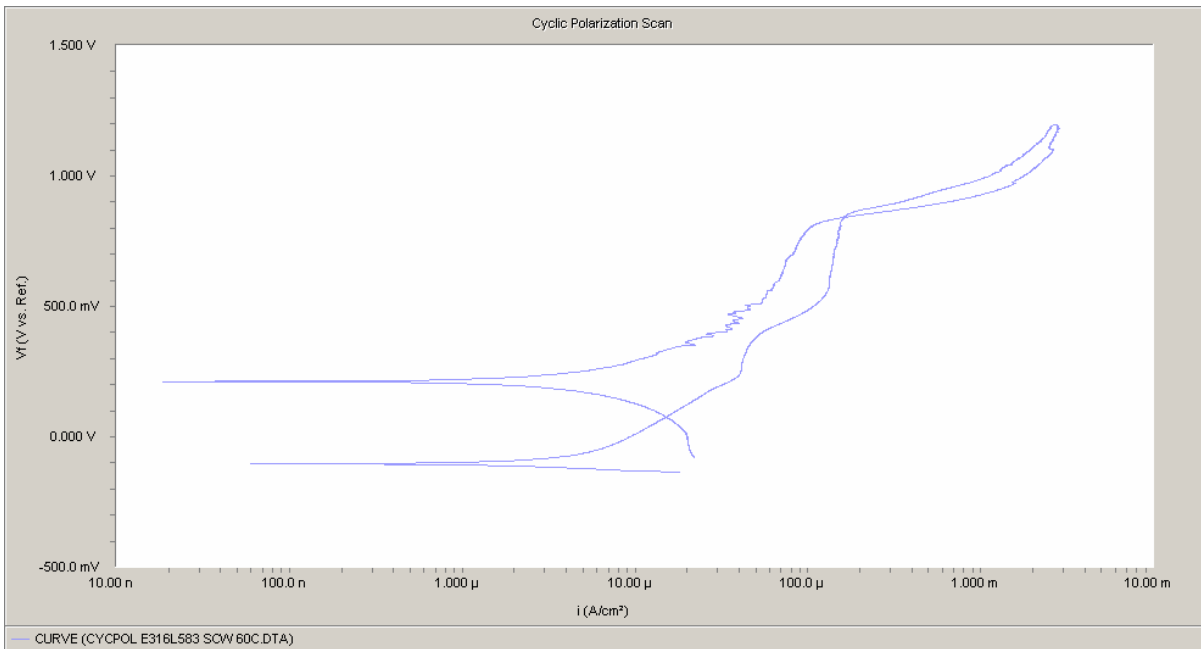


Figure B.4 Cyclic polarization curve – TiN coated E316L583, 60 °C SCW

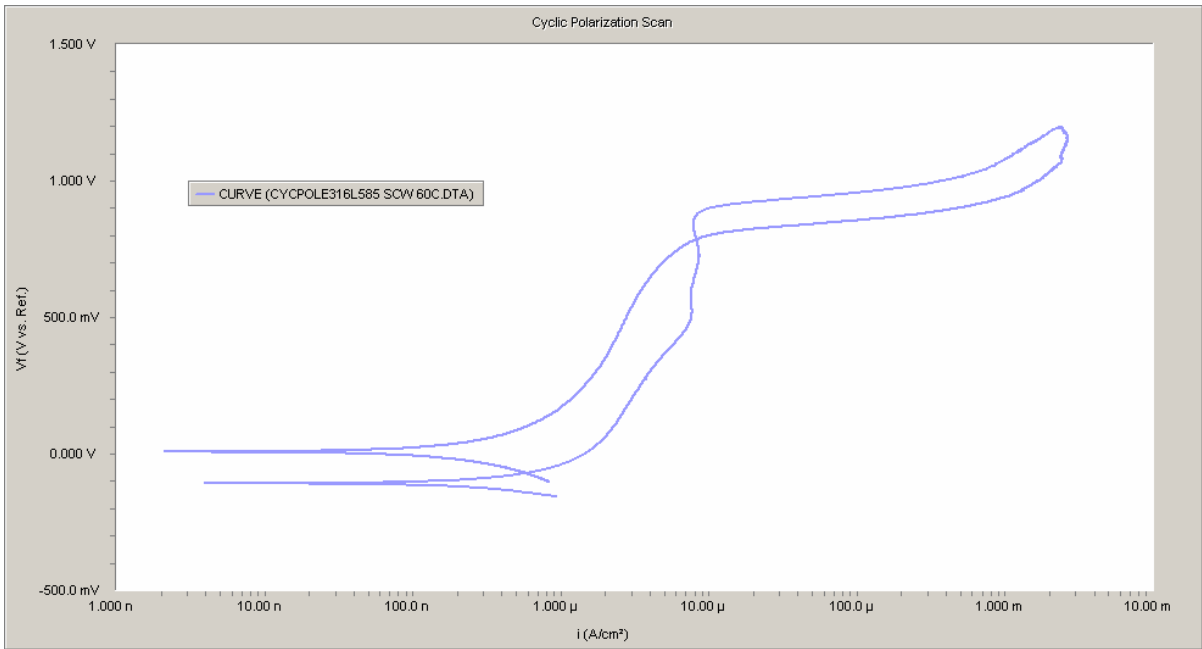


Figure B.5 Cyclic polarization curve – TiN coated E316L585, 60 °C SCW

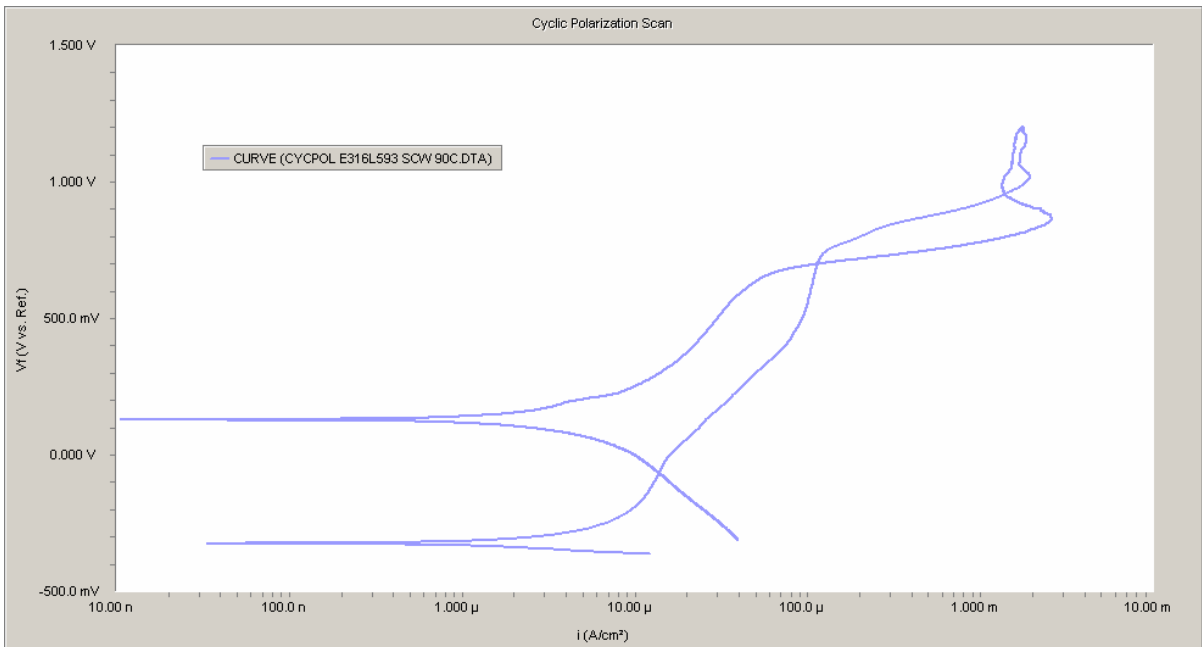


Figure B.6 Cyclic polarization curve – TiN coated E316L593, 90 °C SCW

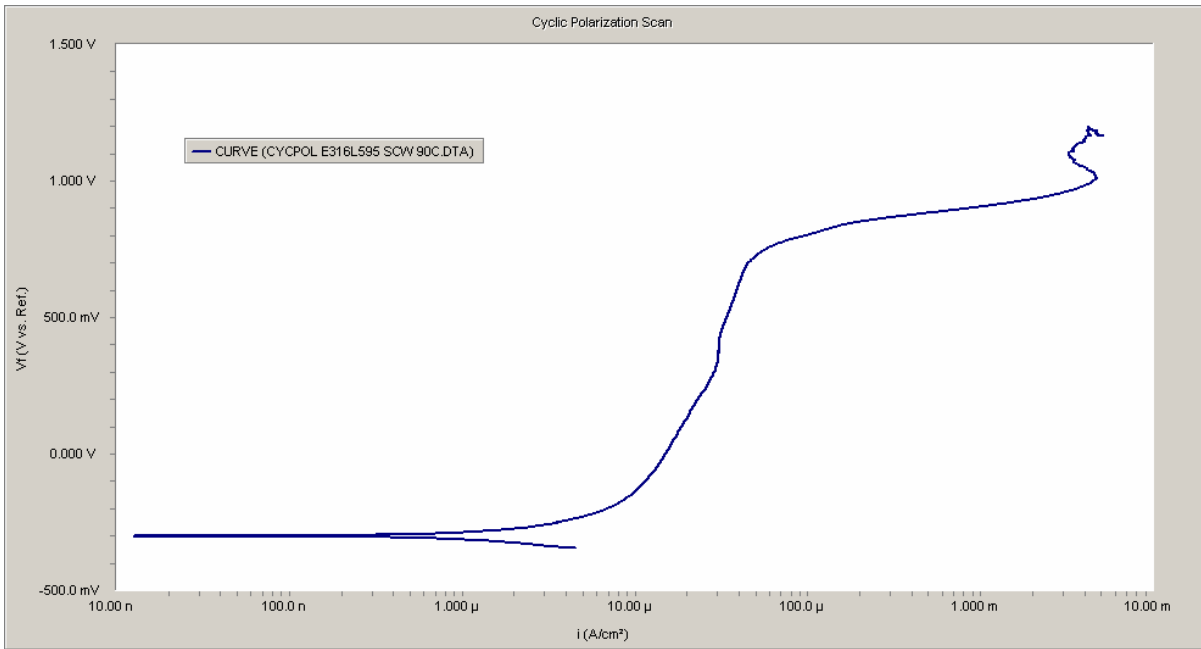


Figure B.7 Cyclic polarization curve – TiN coated E316L595, 90 °C SCW

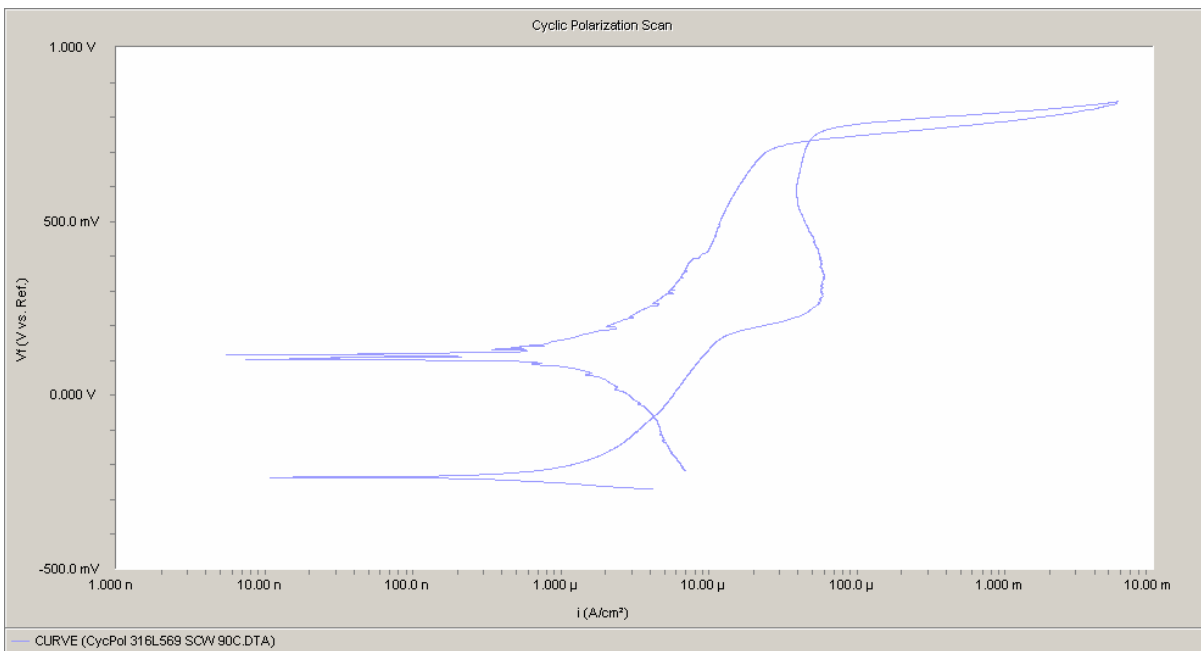


Figure B.8 Cyclic polarization curve – plain 316L stainless steel E316L569, 90 °C SCW

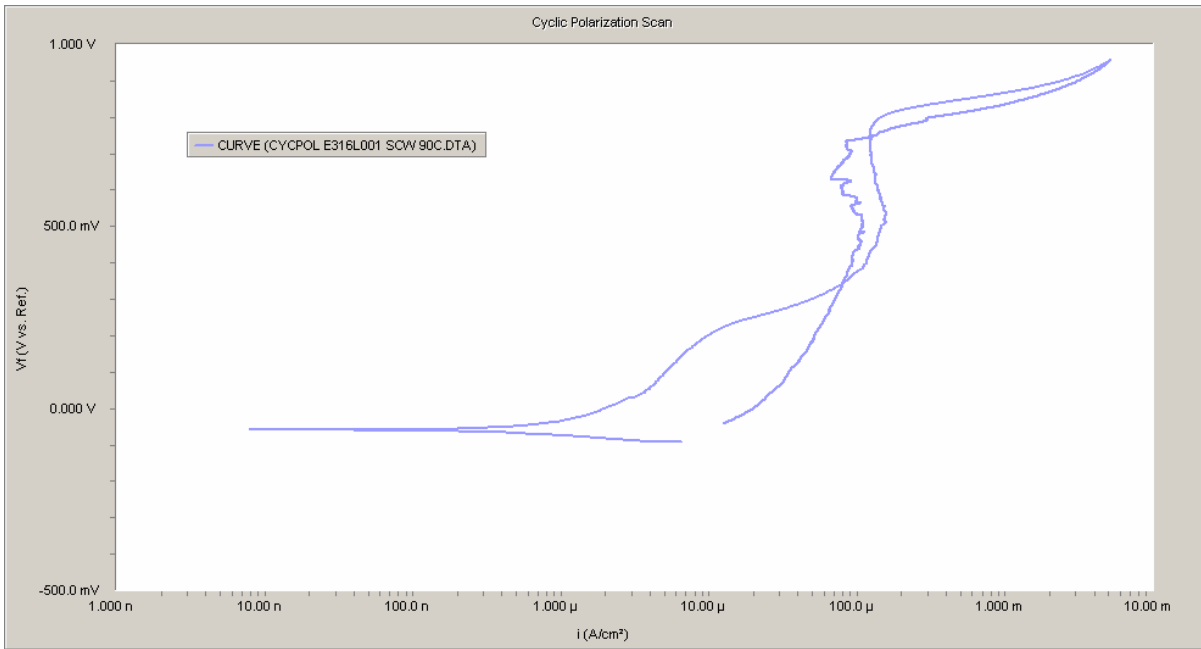


Figure B.9 Cyclic polarization curve – TiN/ZrO₂ coated E316L001, 90 °C SCW

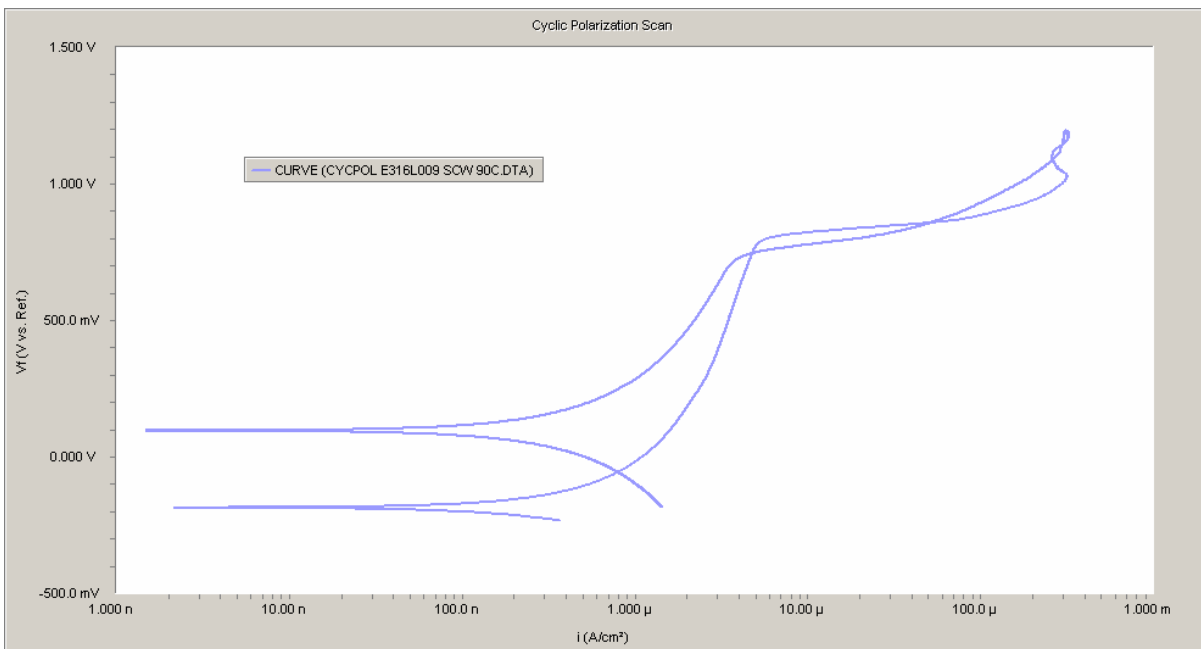


Figure B.10 Cyclic polarization curve – TiN/ZrO₂ coated E316L009, 90 °C SCW

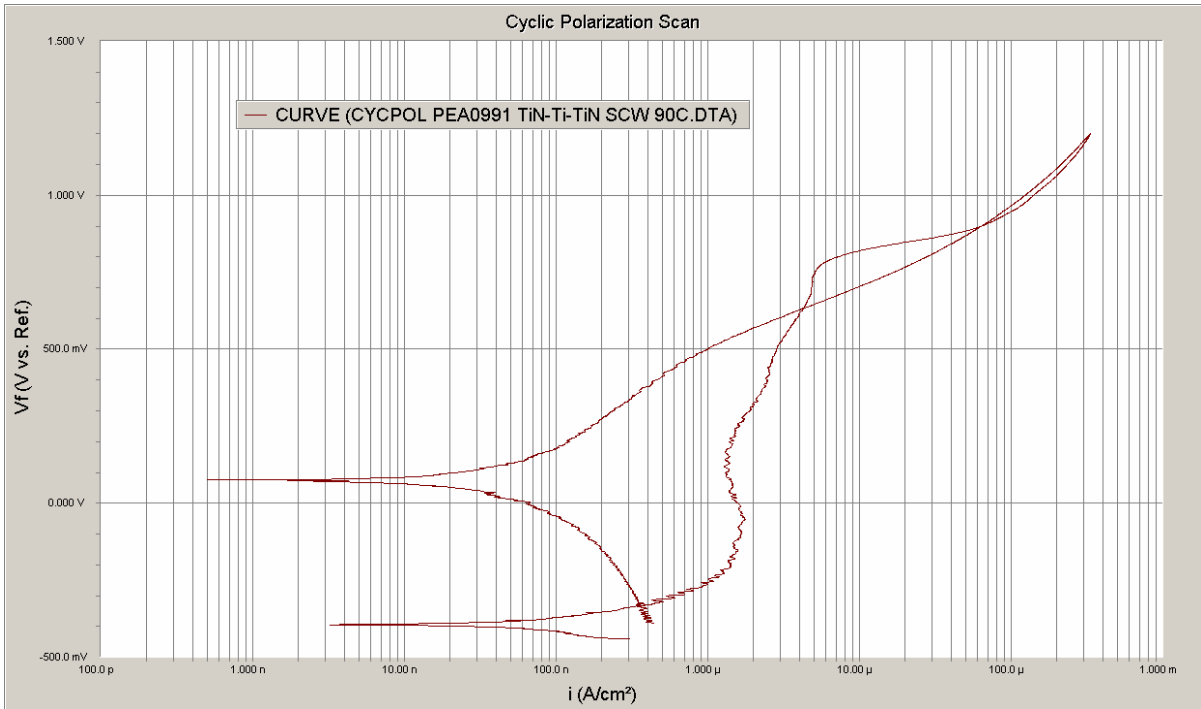


Figure B.11 Cyclic polarization curve – TiN/Ti/TiN coated PEA0991, 90 °C SCW

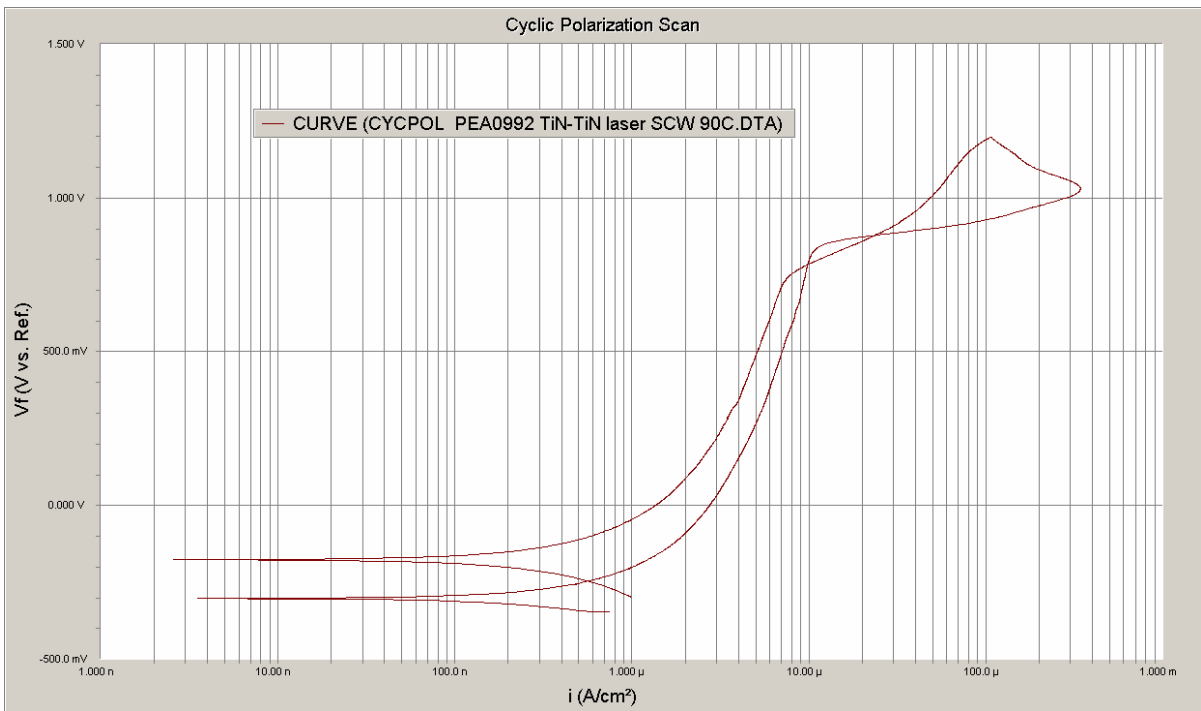


Figure B.12 Cyclic polarization curve – TiN/TiN (laser) coated PEA0992, 90 °C SCW

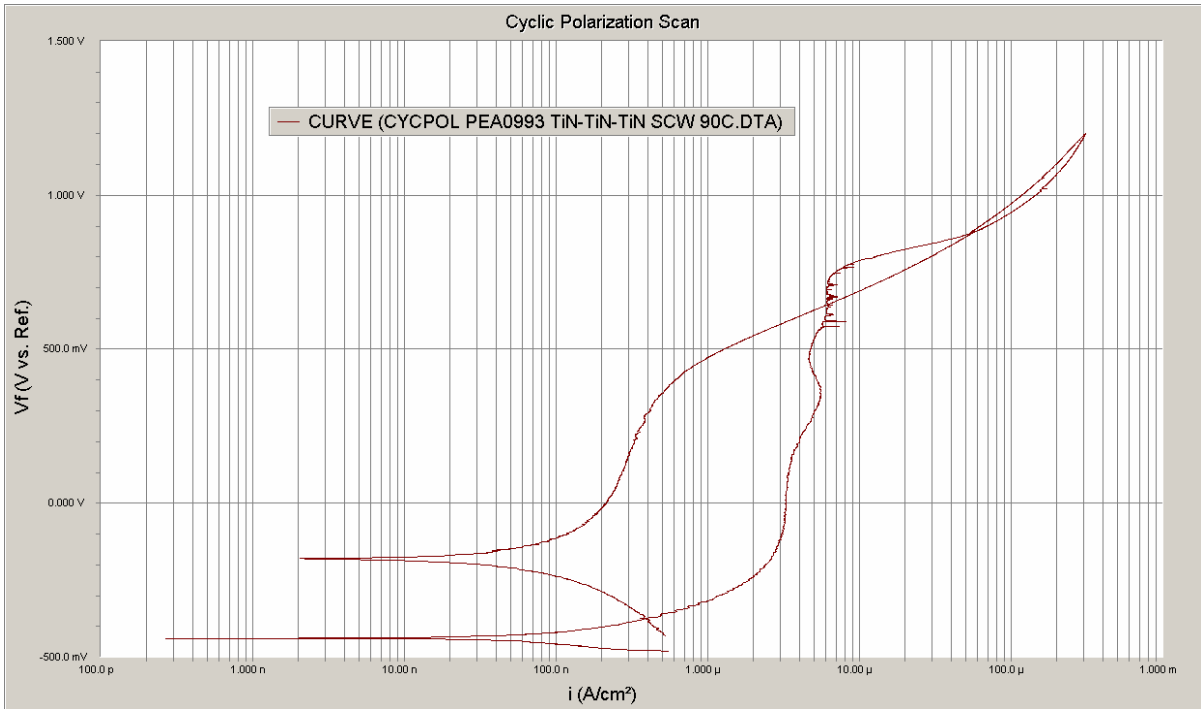


Figure B.13 Cyclic polarization curve – TiN/TiN/TiN coated PEA0993, 90 °C SCW

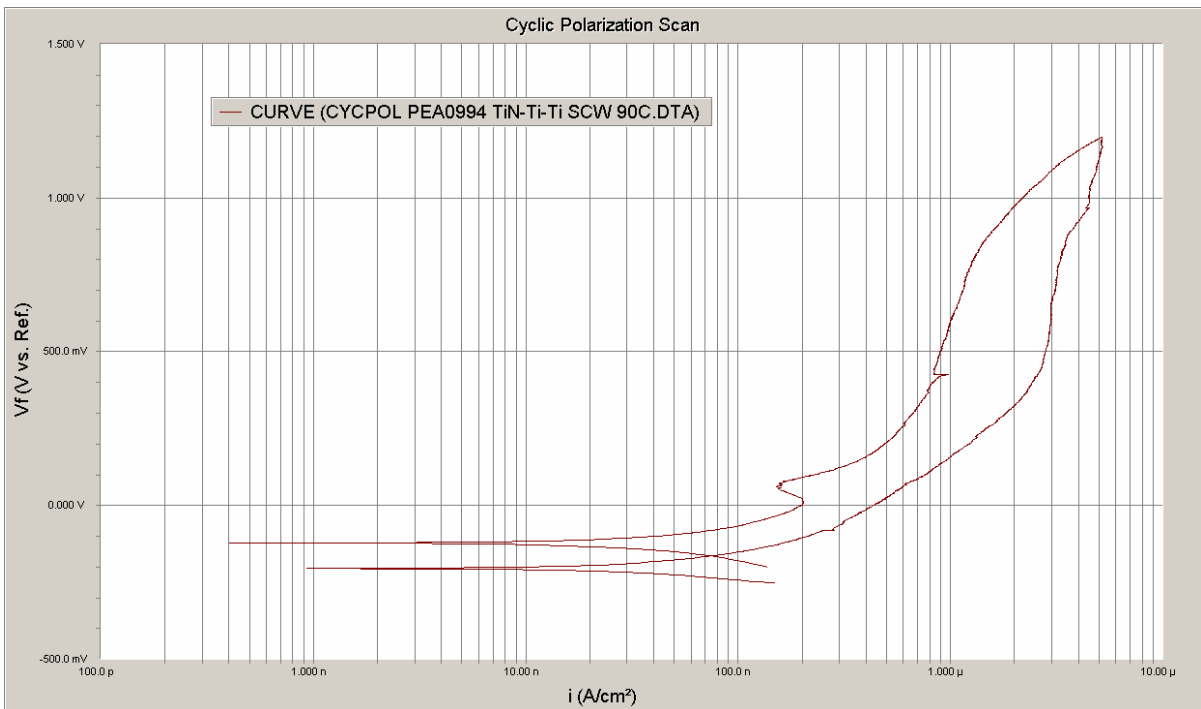


Figure B.14 Cyclic polarization curve – TiNTi/Ti coated PEA0994, 90 °C SCW

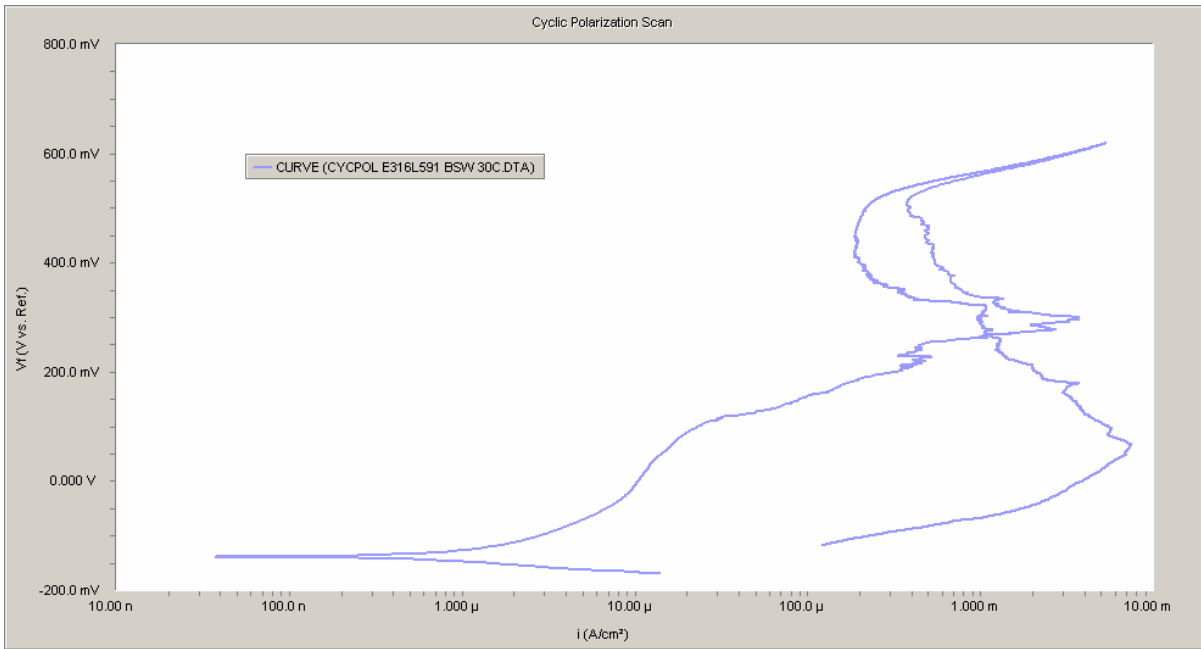


Figure B.15 Cyclic polarization curve – TiN coated E316L591, 30 °C BSW

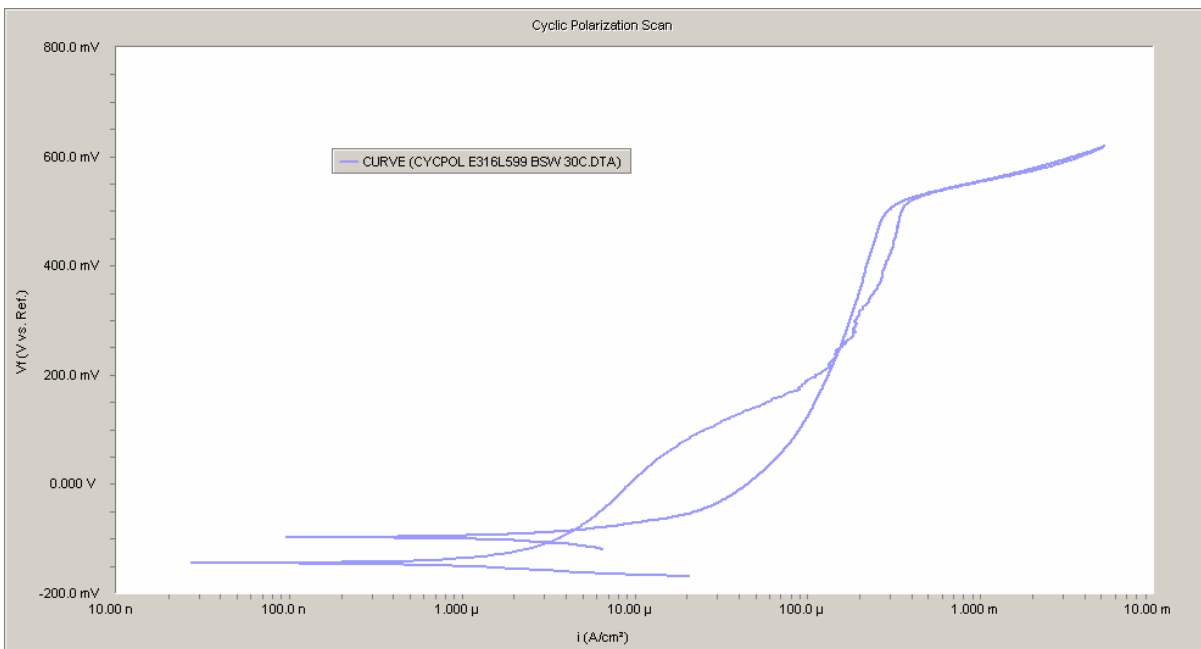


Figure B.16 Cyclic polarization curve – TiN coated E316L599, 30 °C BSW

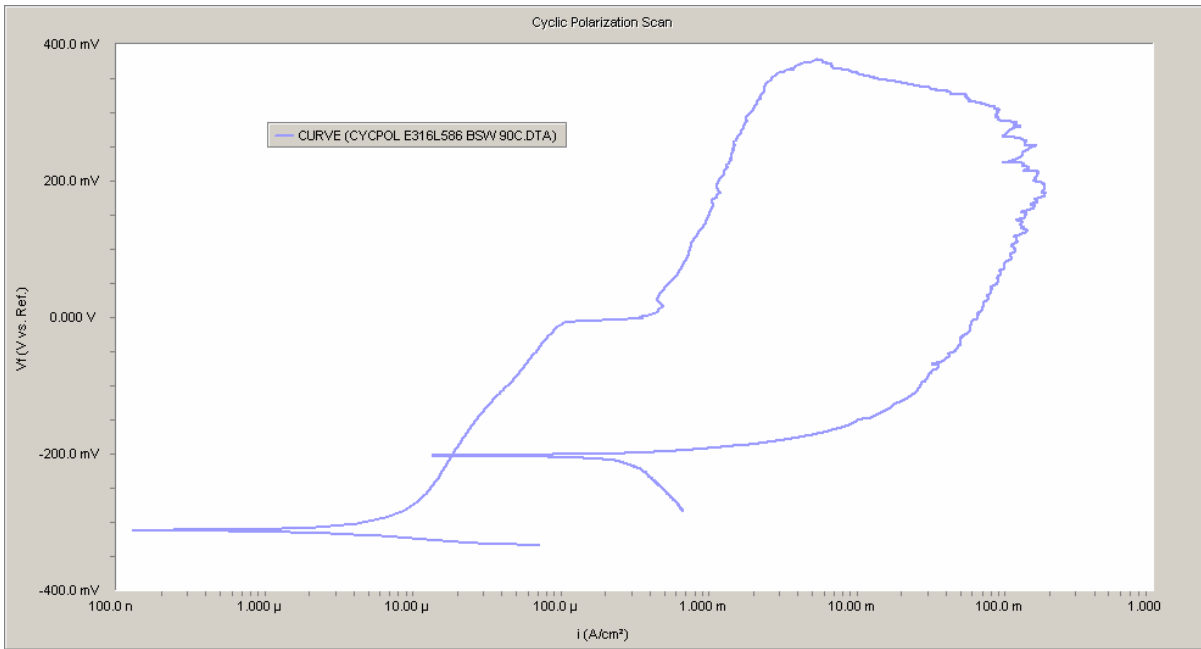


Figure B.17 Cyclic polarization curve – TiN coated E316L586, 90 °C BSW

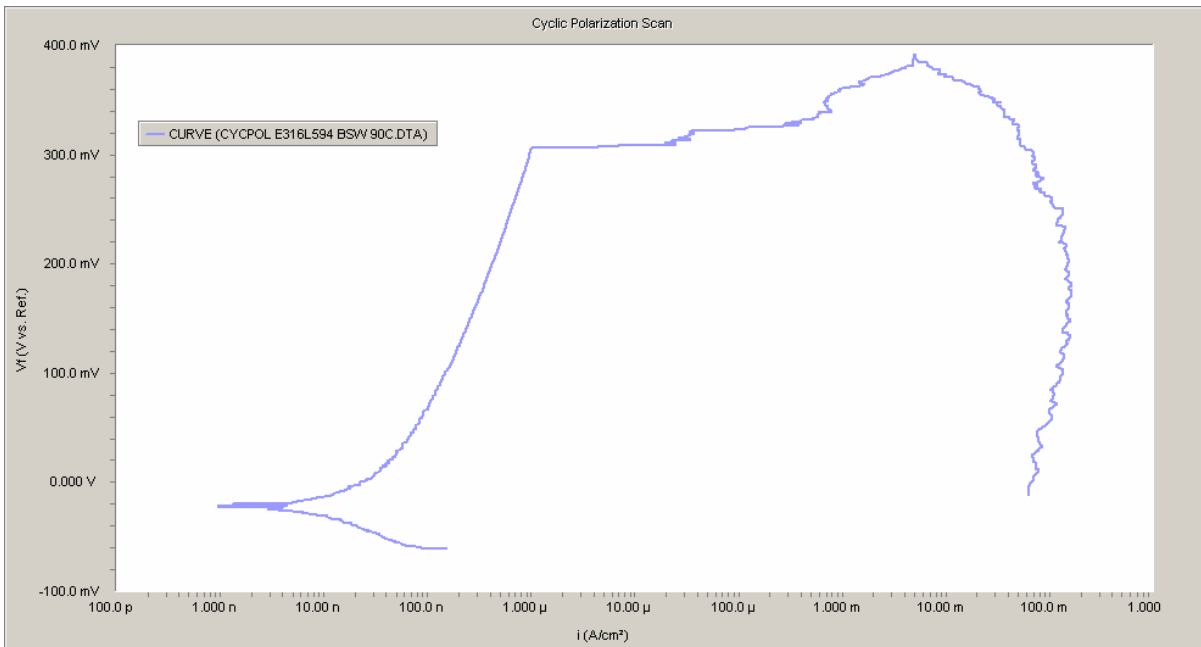


Figure B.18 Cyclic polarization curve – TiN coated E316L594, 90 °C BSW

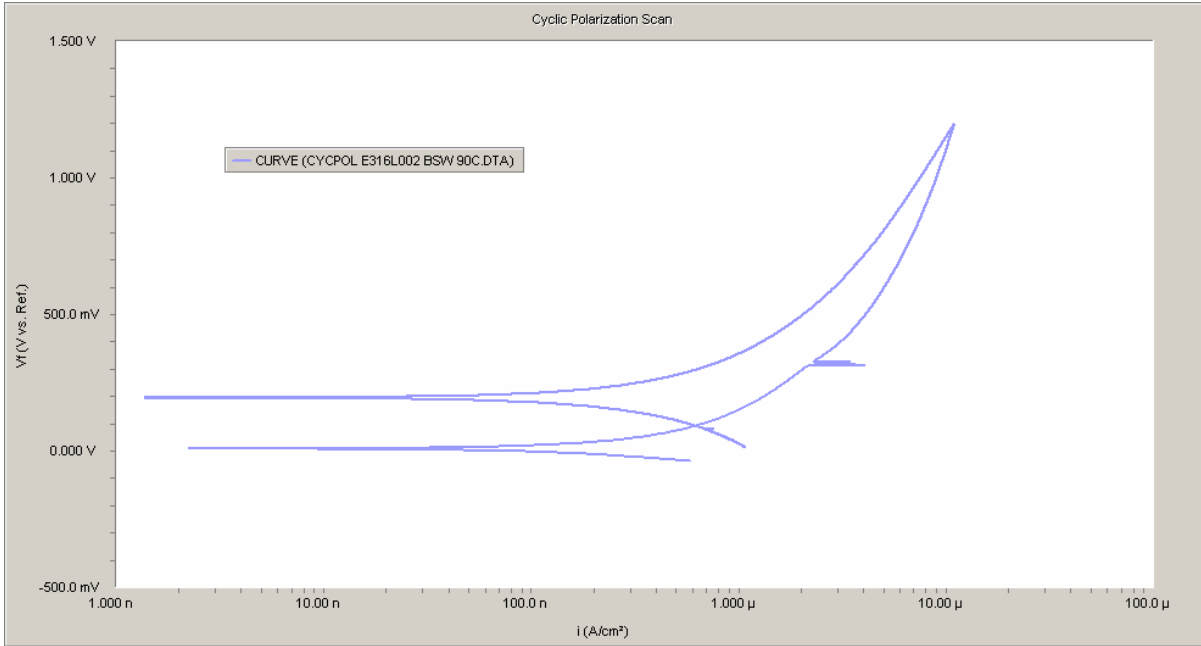


Figure B.19 Cyclic polarization curve – TiN/ZrO₂ coated E316L002, 90 °C BSW

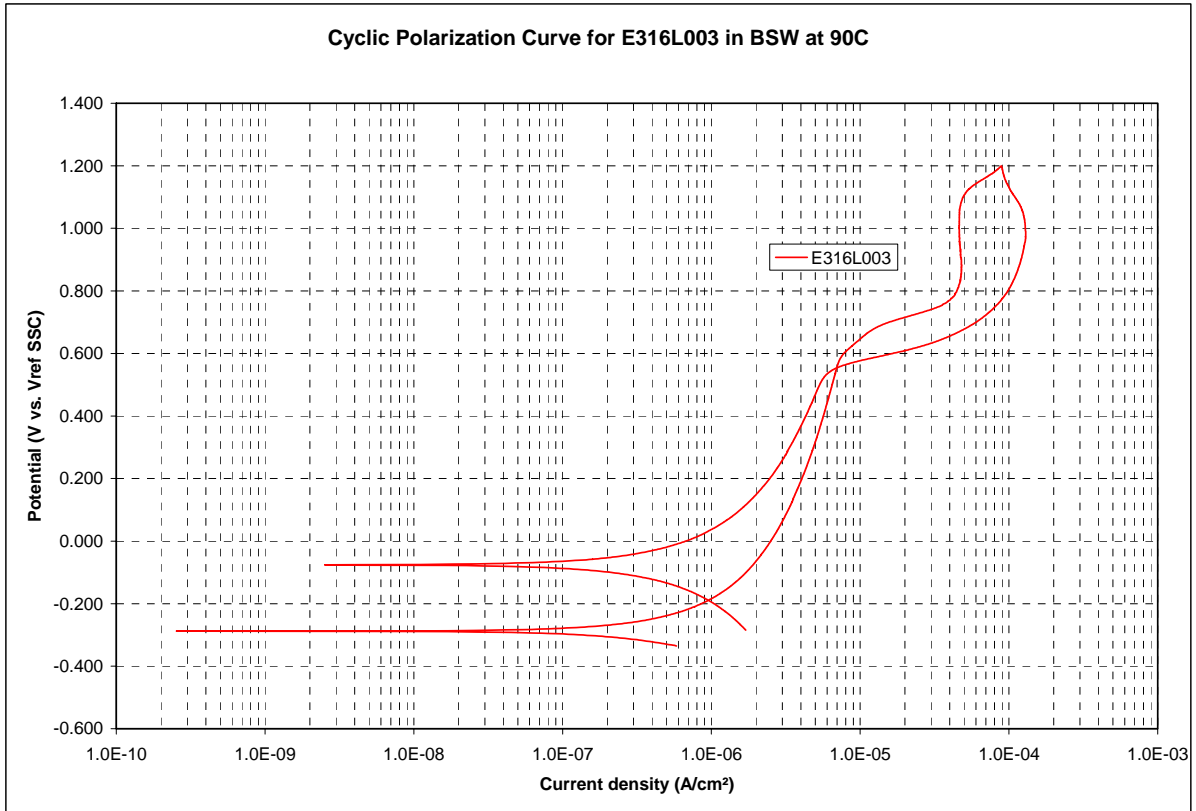


Figure B.20 Cyclic polarization curve – TiN/ZrO₂ coated E316L003, 90 °C BSW

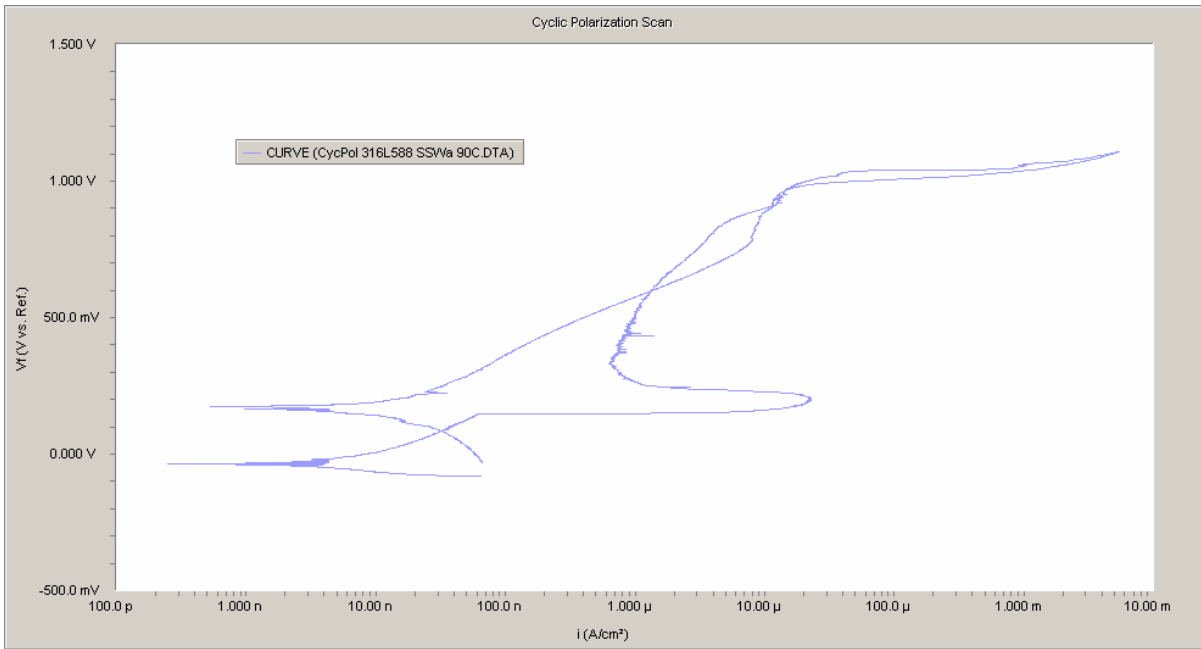


Figure B.21 Cyclic polarization curve – TiN coated E316L588, 90 °C SSW

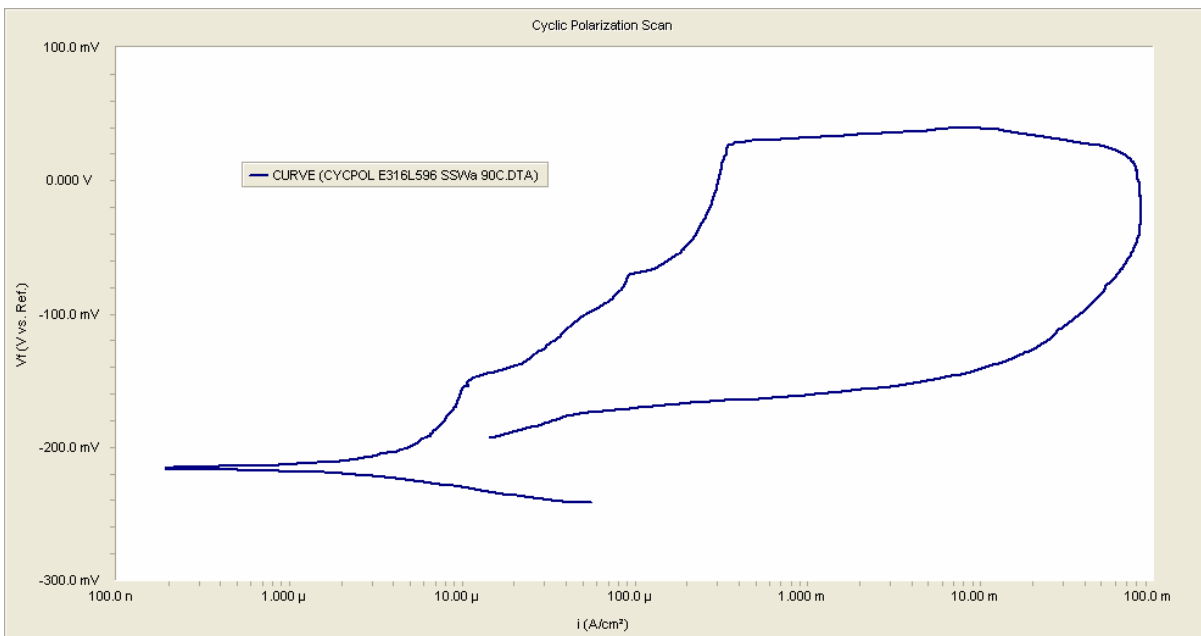


Figure B.22 Cyclic polarization curve – TiN coated E316L596, 90 °C SSW

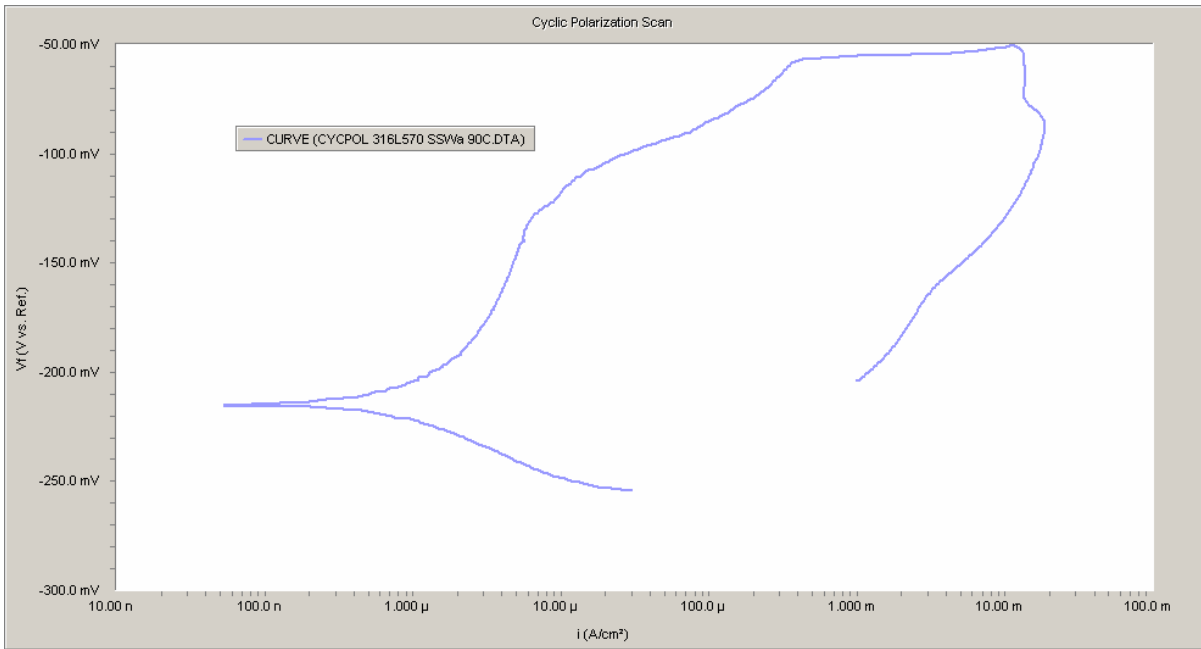


Figure B.23 Cyclic polarization curve – Plain 316L stainless steel E316L570, 90 °C SSW

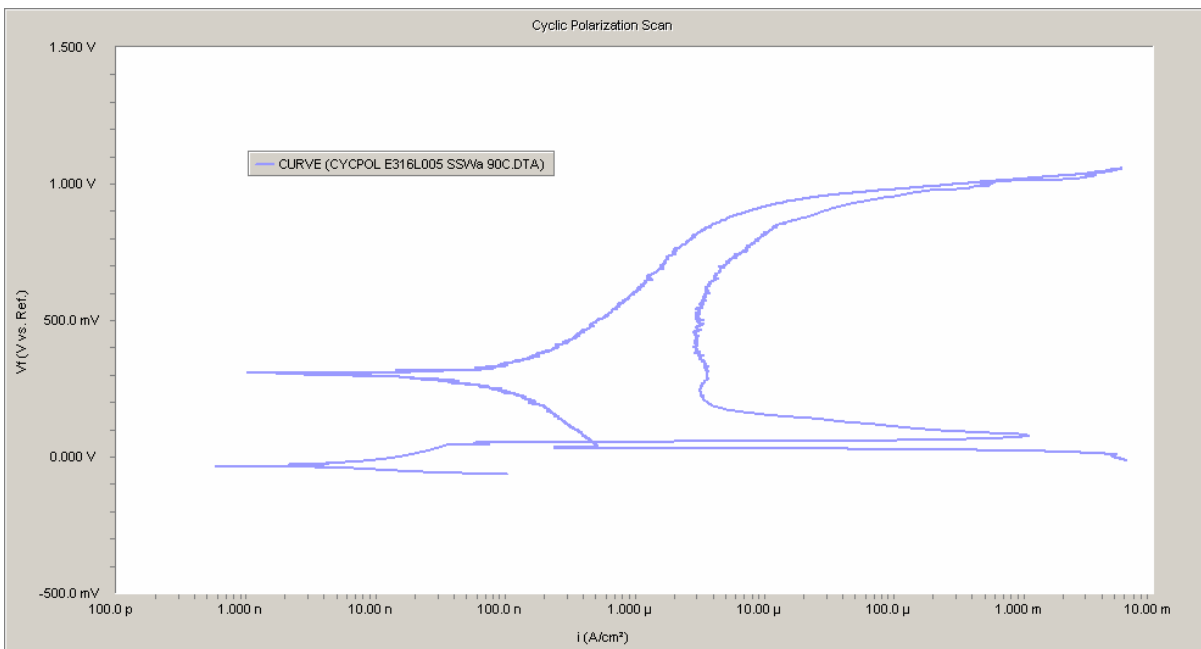


Figure B.24 Cyclic polarization curve – TiN/ZrO₂ coated E316L005, 90 °C SSW

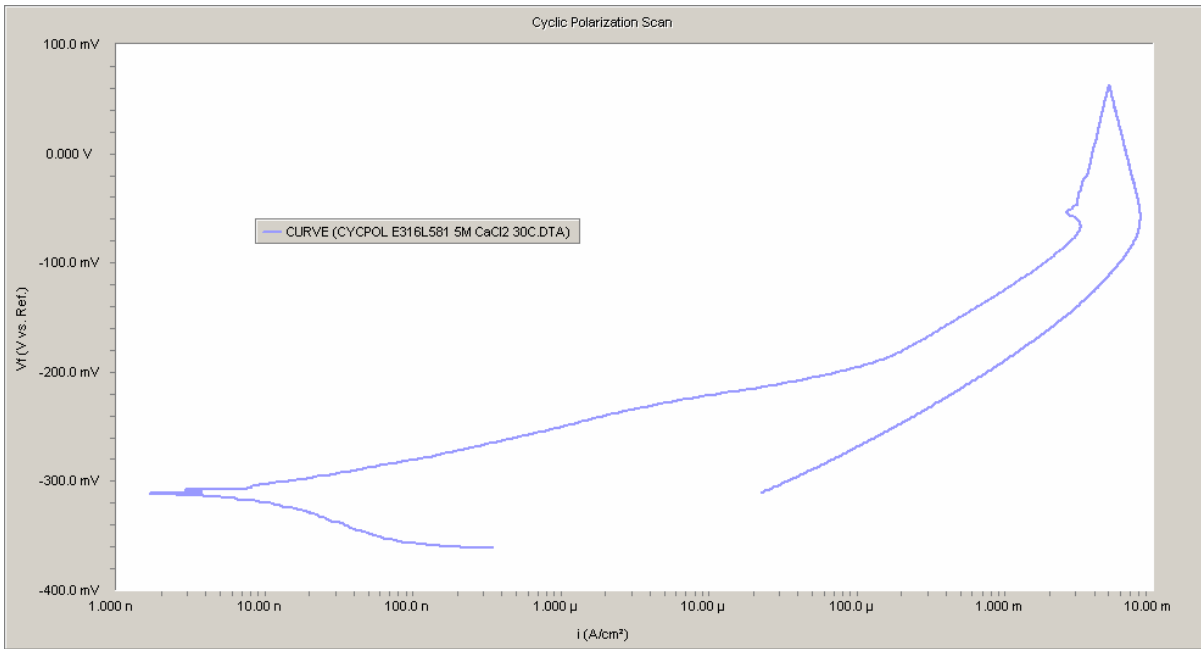


Figure B.25 Cyclic polarization curve - TiN coated E316L581, 30 °C 5M CaCl₂

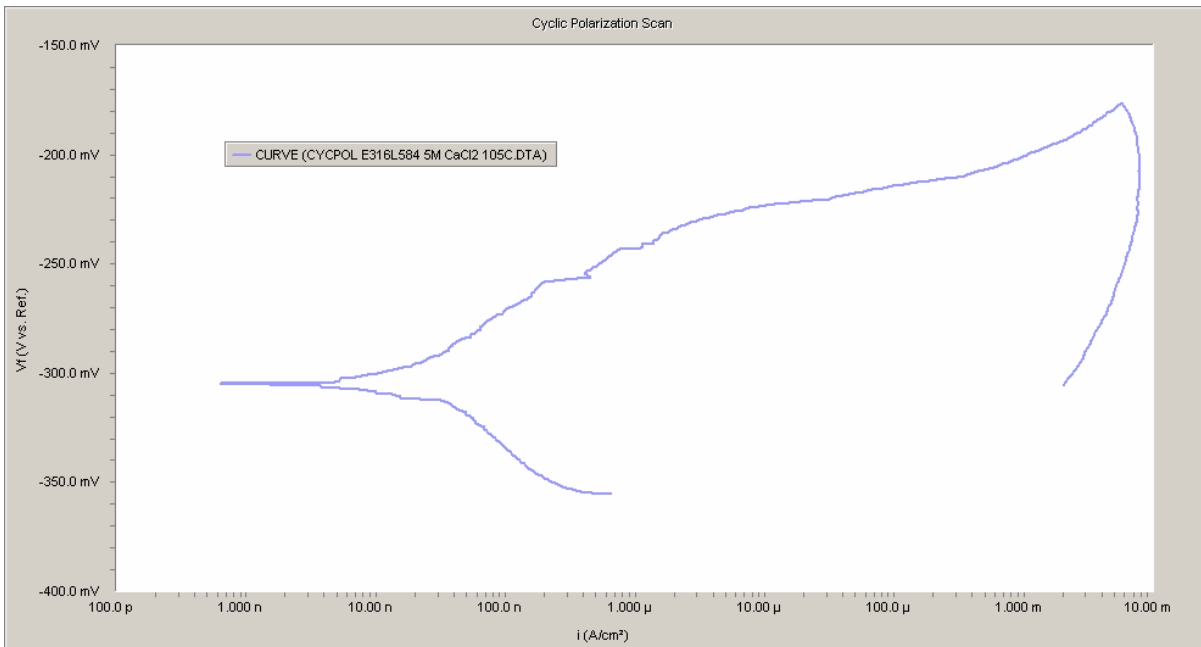


Figure B.26 Cyclic polarization curve - TiN coated E316L584, 105 °C 5M CaCl₂

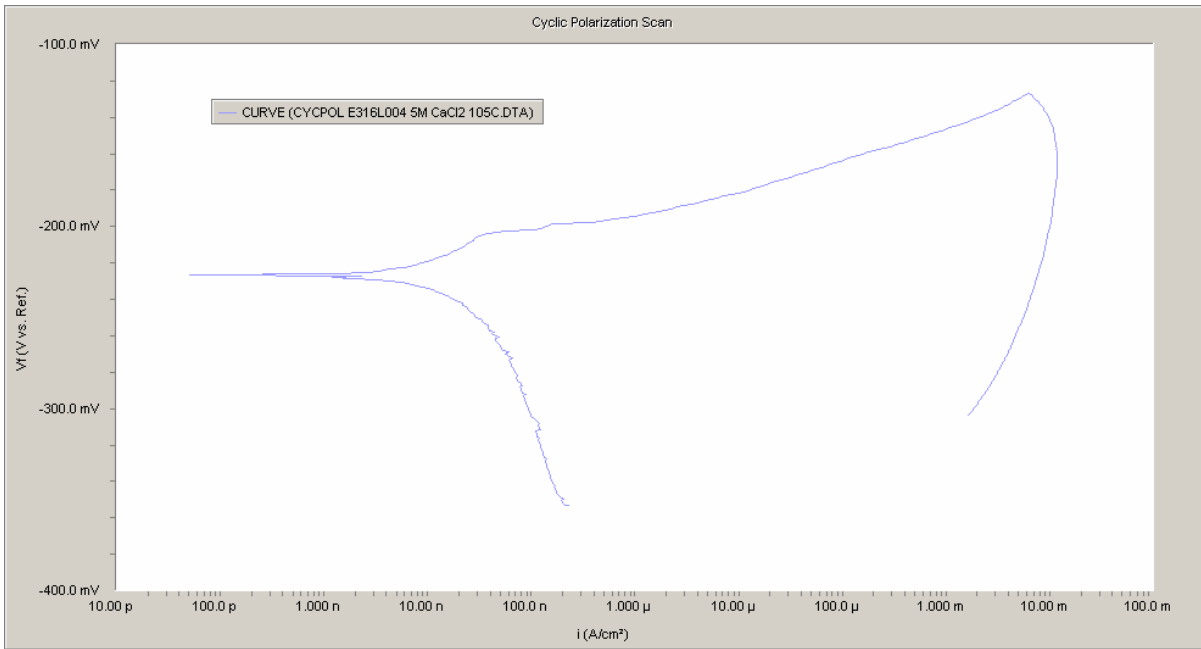


Figure B.27 Cyclic polarization curve – TiN/ZrO₂ coated E316L004, 105 °C 5M CaCl₂

Appendix C – Sample Photos



Figure C.1 TiN coated E316L582 disk sample before test

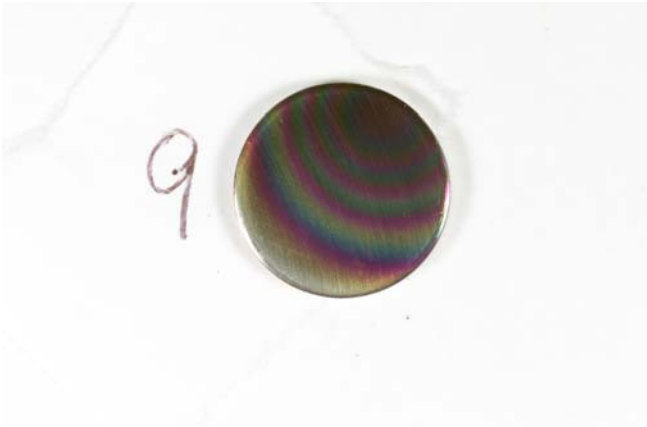


Figure C.2 TiN/ZrO₂ coated E316L009 disk sample before test



Figure C.3 TiN coated weight-loss sample before test



Figure C.4 TiN coated E316L581 after polarization test in 5 M CaCl₂ at 30°C



Figure C.5 TiN coated E316L584 after polarization test in 5 M CaCl₂ at 105°C



Figure C.6 TiN coated E316L588 after polarization test in SSW at 90°C



Figure C.7 TiN coated E316L591 after polarization test in BSW at 30°C



Figure C.8 TiN coated E316L599 after polarization test in BSW at 30°C



Figure C.9 TiN coated E316L586 after polarization test in BSW at 90°C

E316L594



Figure C.10 TiN coated E316L594 after polarization test in BSW at 90°C

E316L589



Figure C.11 TiN coated E316L589 after polarization test in SCW at 30°C

E316L600



Figure C.12 TiN coated E316L600 after polarization test in SCW at 30°C



Figure C.13 TiN coated E316L583 after polarization test in SCW at 60°C



Figure C.14 TiN coated E316L585 after polarization test in SCW at 60°C



Figure C.15 TiN coated E316L593 after polarization test in SCW at 90°C



Figure C.16 TiN coated E316L595 after polarization test in SCW at 90°C



Figure C.17 TiN/ZrO₂ coated E316L004 after polarization test in 5M CaCl₂ at 105°C



Figure C.18 TiN/ZrO₂ coated E316L005 after polarization test in SSW at 90°C

002 - N/8103



Figure C.19 TiN/ZrO₂ coated E316L002 after polarization test in BSW at 90°C

003 - N/8103

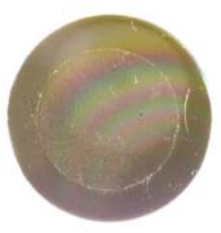


Figure C.20 TiN/ZrO₂ coated E316L003 after polarization test in BSW at 90°C

1



Figure C.21 TiN/ZrO₂ coated E316L001 after polarization test in SCW at 90°C



Figure C.22 TiN/ZrO₂ coated E316L009 after polarization test in SCW at 90°C

Weight loss sample photos: courtesy of Dave Fix, LLNL



Figure C.23 TiN coated weight-loss samples W316L581-583 after 6-month exposure in 90°C SCW Vapor



Figure C.24 TiN coated weight-loss samples W316L590-592 after 6-month exposure in 60°C SCW Vapor



Figure C.25 TiN coated weight-loss samples W316L587-589 after 6-month exposure in 90°C SCW aqueous



Figure C.26 TiN coated weight-loss samples W316L584-586 after 6-month exposure in 60°C SCW aqueous



Figure C.27 TiN coated weight-loss samples W316L594-595 after 6-month exposure in 90°C SCW at water line

W316L593
60°C SCW WaterLine
Removed 2/2/05 @ 1345
Rinsed w/ DI H2O only

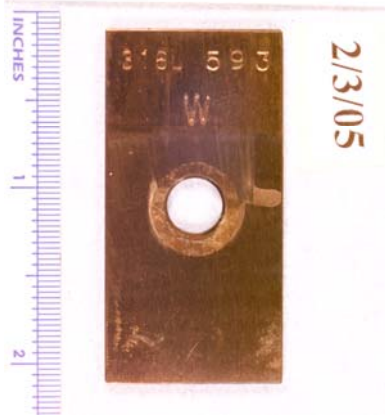


Figure C.28 TiN coated weight-loss sample W316L593 after 6-month exposure in 60°C SCW at water line